#### **Cardiff University**

# Temperature and Polarization Patterns in Anisotropic Cosmologies

## Rockhee Sung

A thesis submitted in partial fulfillment for the degree of Doctor of Philosophy

School of Physics and Astronomy

June 2010

UMI Number: U585366

#### All rights reserved

#### INFORMATION TO ALL USERS

The quality of this reproduction is dependent upon the quality of the copy submitted.

In the unlikely event that the author did not send a complete manuscript and there are missing pages, these will be noted. Also, if material had to be removed, a note will indicate the deletion.



#### UMI U585366

Published by ProQuest LLC 2013. Copyright in the Dissertation held by the Author.

Microform Edition © ProQuest LLC.

All rights reserved. This work is protected against

All rights reserved. This work is protected against unauthorized copying under Title 17, United States Code.



ProQuest LLC 789 East Eisenhower Parkway P.O. Box 1346 Ann Arbor, MI 48106-1346

#### LIST OF ACCOMPANYING PAPERS

This PH.D thesis consists of the following three research articles:

- Sung R and Coles P

  "Polarized Spots in Anisotropic Open Universes", 2009 Class.Quant.Grav.26
- Sung R and Coles P
  "Temperature and Polarization Patterns in Anisotropic Cosmologies",
  arXiv:1004.0957
- Sung R, Short J and Coles P

  "Statistical Characterization of Temperature Patterns in Anisotropic Cosmologies", arXiv:1004.1925

Cardiff University

### Abstract

School of Physics and Astronomy

Doctor of Philosophy

by Rockhee Sung

We study the coherent temperature and polarization patterns produced in homogeneous but anisotropic cosmological models. We show a range of results for all Bianchi types with a Friedman-Robertson-Walker limit (i.e. Types I, V,  $VII_0$ ,  $VII_h$  and IX) to illustrate the possible behaviours that can obtained. We show that localized features in the temperature pattern, perhaps similar to the cold spot observed in the Wilkinson Microwave Anisotropy Probe (WMAP) data, can be generated in models with negative spatial curvature, i.e. Bianchi types V and  $VII_h$ . In Bianchi  $VII_h$ , however, rotation of the polarization angle as light propagates along geodesics can convert E modes into B modes but in Bianchi V this does not happen. We also discuss general properties of the radiation fields. We then consider two possible ways to characterize patterns in CMB temperature maps generated by these anisotropic Bianchi cosmological models. The Pixel Distribution Histogram (PDH) is used as the basis of a discussion of what we mean by 'Gaussianity'. The other method uses multipole vectors, which are derived from the perspective of polynomial defined on the 2-sphere. Although the PDH study gives us limited information to characterize the statistical properties of Bianchi universes, the method using multipole vectors demonstrates a very strong correlation between the multipoles and suggests this could be useful for diagnosing the presence of global asymmetry in the cosmic microwave background.

## Acknowledgements

It is a pleasure to thank those who have helped and inspired me during my doctoral study.

I especially would like to thank my supervisor, Peter Coles, who has made available his support in a number of ways. His guidance and patience helped me in all the time of research and writing of this thesis.

I wish to express my warm and sincere thanks to my friends in Nottingham and Cardiff. They were always in right space-time (!) when I needed their helps.

I owe my deepest gratitude to my family for their unlimited love and support throughout my life. I have no suitable word that can fully describe.

I would like to acknowledge an Overseas Scholarship from the Korean government during my study.

# Contents

D	eclara	ation of Authorship i
De	eclara	ation of Authorship ii
Al	bstra	ct
A	cknov	wledgements
Li	st of	Figures
Li	st of	Tables vii
Sy	mbo	ls viii
1	Star	ndard cosmology 1
		Our Universe
		Study of the Universe
		Theoretical Framework 4
		Paradox of the Big Bang
		Cosmic Inflation 6
		Hypothesis
		Cosmic Microwave Background 9
2	Ani	sotropic cosmology: Bianchi models 11
	2.1	Introduction
	2.2	Bianchi Spaces
	2.3	Bianchi Cosmologies
		2.3.1 Basics

Contents	V.

		2.3.3 Tetrad Frame		•	•	•	•		26
3	Bac	ckground radiation in Bianchi universes	8						28
	3.1	Radiation Transport in Anisotropic Cosmo	logies						
		3.1.1 Radiation Description					•		
		3.1.2 Scattering							
		3.1.3 Transfer Equation							33
		3.1.4 Geodesic Equation							3'
	3.2	Conclusions					•		39
4	Ten	mperature and Polarization Patterns							4
	4.1	Bianchi Maps							43
	4.2	Parameter Limits		•					4
	4.3	Bianchi Maps, Initial Dipole							5
		4.3.1 The Cold Spot							5
		4.3.2 Implications for E and B Modes							5
	4.4	Conclusions		•			•		6
5	Sta	atistical Characterization of Anisotropie	s						6
	5.1	Pixel Distribution Histogram							6
									6
		5.1.1 Applications						•	
		5.1.1 Applications							
				•					6
		ILC maps		•					6 6
	5.2	ILC maps	  ole		 				6 6 7
	5.2	ILC maps	· · · · · · · · · · · · · · · · · · ·	•	· ·				6 6 7 7
	5.2	ILC maps			· · · · · ·				66 70 71 7
	5.2	ILC maps			· · · · · ·				66 70 71 7
	5.2	ILC maps		•					66 70 7 7 7
	5.2	ILC maps	ole			· · · · · ·			66 70 7 7 7 7 79
	5.2	ILC maps	ole						66 70 7 7 7 79 79
	5.2	ILC maps	ole						66 70 77 77 79 79 80 81
	5.2	ILC maps	ole			· · · · · · · · · · · · · · · · · · ·			66 60 70 70 70 70 70 80 80 80

Conten	ts	vi
A.1	Liouville Equation	. 91
A.2		
A.3		
A.4	Coefficients of Boltzmann Equation	. 95
A.5	Extra terms from the geodesic equation	. 96
A.6	Variation of Complex Vector, $m^i$	. 97
В		98
B.1	$a_{E,lm}$ and $a_{B,lm}$ from $N^2$	. 99
$\mathbf{C}$		102
C.1	Spherical Harmonics as $\alpha$ Notations	. 102
C.2	Numerical results for multipole vectors	. 104
Riblio	graphy	110
Biblio	graphy	1

# List of Figures

4.1	Initial configuration chosen for the temperature pattern. Where the initial conditions produce a pure quadrupole anisotropy of <i>tesseral</i> form, i.e. and $l=2$ spherical harmonic mode with $m=1,\ldots,\ldots,\ldots$	42
4.2	Polarization maps, i.e. degree of linear polarization (left),	12
	Stokes parameter Q (middle) and U (right) of Bianchi type	
	I. The polarization patterns do not evolve with time	43
4.3	The time evolution of the temperature maps for Bianchi types $V$ , $VII_h$ and $VII_0$ . Time increases from bottom to top. in Type $V$ (left), the initial quadrupole retains its shape but	
	gets focussed into a patch of decreasing size as time goes on.	
	In Bianchi Type VII <sub>0</sub> (right) the effect of rotation and shear	
	is to twist the initial quadrupole into a spiral shape that	
	winds up increasingly as the system evolves. In the middle	
	case, Bianchi Type $VII_h$ we have a combination of the two	15
1 1	cases either side: there is both a focussing and a twist The time evolution of polarization maps for Bianchi V: de-	45
4.4	gree of linear polarization (left); Stokes parameter Q (mid-	
	dle); and U(right). Time increases from bottom to top.	
	While the polarization pattern alters with time in this case,	
	its general orientation on the sky does not as is the case with	
	the temperature pattern	46
4.5	Same as Figure 4.4, but for Bianchi type $VII_h$ . The prodi-	
	gious twisting of the polarized component of the radiation	
	field, as well as a concentration of the degree of polarization.	
	This case generically produces a large amount of mixing be-	
	tween $Q$ and $U$ during its time evolution	47
4.6	Same as Figure 4.4, but for Bianchi type VII <sub>0</sub> . It produces	
	a similar interweaving of the $Q$ and $U$ configurations, but	
	without the focussing effect in the total polarized fraction	48

4.7	Same as Figure 4.4, but for Bianchi type IX. In terms of polarization degree, the pattern does change at all with time but the Stokes maps $Q$ and $U$ do evolve. The positive cur-	
	vature does not allow for any focussing effects so the temperature pattern does not change with time either	50
4.8	Temperature maps for Bianchi types V, VII <sub>h</sub> and VII <sub>0</sub> with different values of the density parameter, $\Omega_0$ , which increases from top to bottom. It shows how $\Omega_0$ affect the pattern on	
	the maps for each of types we consider	51
4.9	Temperature maps for Bianchi VII <sub>h</sub> type as parameters limits: $h$ is decreased from top to bottom and $\Omega_0$ is increased from left to right. If we take various limits of them, we obtain	
4.10	these subclasses i.e. I, V and $VII_0$ on some stage Temperature (left) and polarization maps i.e. Stokes parameter $Q$ (middle) and $U$ (right) of Bianchi type I which	52
	has initial dipole. Time increases from bottom to top. The temperature pattern is highly affected by the dipole at early	
4.11	time	53
	(bottom) to late time (top) for Bianchi $V$ (left), $VII_h$ (middle) and $VII_0$ (left). These models have a initial dipole	54
4.12	The time evolution polarization maps from early stage (bottom) to late time (top) for Bianchi $V$ type: degree of polar-	
4.13	ization (right), Stokes parameter Q (middle) and U (left) Time evolution polarization maps from early stage (bottom)	55
	to late time (top) for Bianchi $VII_h$ type: degree of polarization (right), Stokes parameter Q (middle) and U (left)	56
4.14	Time evolution polarization maps from early stage (bottom) to late time (top) for Bianchi VII <sub>0</sub> type: degree of polarization (right), Stokes parameter Q (middle) and U (left)	
		57
4.15	Time evolution polarization maps from early stage (bottom) to late time (top) for Bianchi IX type: degree of polarization	
1.10	(right), Stokes parameter Q (middle) and U (left)	58
4.16	Quadrupole patterns for Bianchi $V$ (left) and $VII_h$ (right) which show how they are affected by increased initial dipoles	
	from pure quadrupole without initial dipole (bottom) to affected quadrupole which makes a cold spot and hot ring	
	around it (top).	59

List of Figures x

4.17	Temperature and Polarization maps for Bianchi models with localized features (aligned with the known CMB Cold Spot). The left panels show the temperature, the right the total polarization $P = \sqrt{Q^2 + U^2}$ . The top row shows an example of Bianchi VII <sub>h</sub> with a compact spiral feature produced by focusing and twisting; the polarized component contains a significant B-mode. The bottom row shows a Bianchi V model in which the initial quadrupole is focussed but not twisted. The polarized field in the latter case has no B-mode.	60
5.1	The Harmonic Internal Linear Combination (HILC5YR) tem-	
5.2	perature and polarization (Q and U) maps	66
5.3	The PDH of temperature pattern (top) and polarization maps i.e. polarization amplitude (lower, left), Stokes parameter Q (lower, middle) and U (lower, right) of Bianchi	07
5.4	type I	68
5.5	$VII_0$ (lower,left) types	69
5.6	early and late (dot) to late stage (thick line)	70
57	(top) and IX (bottom)	71
5.7	Same as Figure 5.4, but for Bianchi types which have initial dipole	79

5.8	For Bianchi V type, the PDH for dipole (left), quadrupole	
	(middle) and overall (right) maps as different density pa-	
	rameters such as $\Omega_0 = 0.3$ (green), $\Omega_0 = 0.6$ (magenta),	
	$\Omega_0 = 1$ (cyan). The temperature patterns also are simulated	
	for multipoles as rely on density parameters such as $\Omega = 0.3$	
	(second row), $\Omega_0 = 0.6$ (third row), $\Omega_0 = 1$ (fourth row)	73
5.9	Same as Figure 5.8 but for Bianchi $VII_h$ type	74
5.10	Normalized Stokes parameters, Q (top, left) and U (top,	
	right), the PDH for Bianchi V type as different density pa-	
	rameters such as $\Omega = 0.3$ (magenta), $\Omega = 0.6$ (green), $\Omega = 1$	
	(cyan). These patterns also are simulated as relying on den-	
	sity parameters such as $\Omega = 0.3$ (second row), $\Omega = 0.6$ (third	
	row), $\Omega = 1$ (fourth row)	75
5.11	Same as Figure 5.10, but for Bianchi type $VII_h$	76
5.12	The multipole vectors from $BianchiV$ map such as The dipole	
	(left), quadrupole (middle) and octopole (right)	80
5.13	The multipole vectors from the Bianchi V (left), $VII_h$ (mid-	
	dle) and VII <sub>0</sub> (right) maps from early stage (bottom panel)	
	to late time (top panel). These vectors are represented by	
	dots as dark blue for dipole, as light red for quadrupole and	
	as brown for octopole. Background colours also indicate if	
	any of the multipoles over-lap; yellow for no overlapped mul-	
	tipoles (right row and bottom of middle row), green for over-	
	lapped dipole and octopole, light yellow (bottom of left row)	
	for quadrupole and octopole and light blue (top of left row)	
	if all the multipole vectors are overlapped	81
5.14	Same figure, but for initial dipole	82

# List of Tables

2.1	The Bianchi types shown in terms of whether the various parameters used to construct the classification are zero, positive or negative; the designation of Class A or Class B depends on whether $a = 0$ , or not, respectively. The parameter $h$ is defined by $h = a^2/n_1n_2$ . The spaces of particular interest
	in this paper are I, V, VII <sub>0</sub> , VII <sub>h</sub> and IX because these con-
	tain the isotropic FRW spaces as limiting cases; the others are shown just for completeness
2.2	Dependence of the scalar curvature of the spatial sections ${}^*R$
	on the parameters $a$ and $n_i$ involved in the construction of the Bianchi classification for those models with an FRW limit. 20
2.3	The Bianchi types shown in terms of the group dimension $p$ and number of arbitrary constants needed to specify the model on a given constant time surface, in vacuum $(r)$ and
	with a perfect fluid equation of state $(s)$
3.1	The angle variations of Bianchi types. Note that we consider the FRW limits i.e. Bianchi vectors as $n_i = n$
C.1	Numerical results from multipole vectors of Bianchi type V (left row of the Figure 5.13)
C.2	Numerical results from multipole vectors of Bianchi type $VII_h$ (middle row of the Figure 5.13) 105
C.3	Numerical results from multipole vectors of Bianchi type VII <sub>0</sub> (right row of the Figure 5.13)
C.4	Numerical results from multipole vectors of Bianchi type V with initial dipole (left row of the Figure 5.14) 107
C.5	Numerical results from multipole vectors of Bianchi type $VII_h$ with initial dipole (middle row of the Figure 5.14) 108
C.6	Numerical results from multipole vectors of Bianchi type VII <sub>0</sub> with initial dipole (right row of the Figure 5.14) 109
	· · · · · · · · · · · · · · · · · · ·

# **Symbols**

#### Note

- 1. Greek indices denote tensor components, Latin indices tetrad components:  $a, b, c, \ldots$  run from 0 to 3,  $i, j, k, \ldots$  from 1 to 3.
- 2. Bar indicates complex conjugate.
- 3. Semicolons denote covariant derivatives.
- 4. Dot denote time derivatives.

#### Constants

c Speed of light

 $h_P$  Planck's constant

G Gravitational constant

#### Chapter 1

K Curvature

 $a_s$  Cosmic scale factor

 $\Lambda$  Cosmological constant

 $G_{ab}$  Einstein tensor

 $R_{ab}$  Ricci tensor

R Ricci scalar

 $T_{ab}$  Energy momentum tensor

 $g_{ab}$  Metric tensor

 $u^a$  Fluid velocity

 $\rho, p$  Density, pressure

#### $V(\Phi)$ Potential of scalar quantum field

#### Chapter 2

 $\xi_i$  Killing vectors

 $C_{ik}^{i}$  Structure constants

 $\delta_i^j$  Kronecker delta

 $\epsilon^{ijk}$  Total antisymmetric tensor

 $\mathcal{L}_{\xi}\zeta$  Lie derivative of  $\zeta$  taken along  $\xi$ 

 $G_L$  L-dimensional group structure

 $a_i$  Bianchi vector,  $a_i = (a, 0, 0)$ 

 $n_{ij}$  Bianchi tensor,  $n_{ij} = diag(n_1, n_2, n_3)$ 

R Scalar curvature of the spatial section

 $h h \equiv a^2/n_2n_3$ 

 $\Omega_0$  Total density parameter

 $x_{para}$   $\frac{h}{1-\Omega_0}$ 

 $\omega$  Rate of rotation

 $\sigma_{ab}$  Shear tensor

 $h_{ab}$  Projection tensor

 $\omega_{ab}$  Vorticity tensor

 $\theta$  Expansion scalar

 $x^{\alpha}$  Local coordinate system

 $\mathbf{e}_a$  Tetrad vectors

 $\Gamma^a_{bc}$  Ricci rotation coefficients or connection components for the tetrad

 $\gamma^a_{\ bc}$  Time dependent structure constant or commutation function

#### Chapter 3

 $\nu$  Light frequency

 $\varepsilon$  Energy of photon  $(=h\nu)$ 

 $N^A$  Photon distribution components, A=0 (spin 0), 2 (spin 2)

I, Q, U, V Stokes parameters

P Degree of polarization

 $\chi$  Angle of the polarization orientation

$k^i$	Three-dimensional ray direction
	(01)

$$m^{i}$$
  $m^{i} = \frac{1}{\sqrt{2}} \left( \frac{\partial k^{i}}{\partial \theta} + \frac{i}{\sin \theta} \cdot \frac{\partial k^{i}}{\partial \phi} \right)$ 

 $p^a$  Four momentum of a photon

ð Spin differential operator

 $\mathcal{D}_A$  Angular operator

$$\gamma^a \qquad \quad \gamma^a \equiv \Gamma^a_{\ 00} + \Gamma^a_{\ 0i} k^i + \Gamma^a_{\ i0} k^i + \Gamma^a_{\ ik} k^i k^k. \label{eq:gamma_a}$$

 $p_{AB}, \hat{p}_{AB}$  Scattering matrices

 $n_e$  Free electron number density

 $\sigma_T$  Thomson scattering cross section

## Chapter 1

## Standard cosmology

Our Universe. Our Universe is, by definition, an unusual object. There is only one Universe to be observed. We have no other sample to compare it with and from which to infer its character. An event such as the Big Bang (if it happened) is not repeatable. The situation we observe it from is also peculiar. We are not able to choose the time or position from which we view it. The accessibility of the Universe for observation is limited in different ways: since the speed of light is finite we are not able to see further than light can have traveled since the origin of the Universe; on the other hand, the information of sky is serious blocked by the Milky Way, absorbed and distorted.

Study of the Universe. Cosmology has a long history, from ancient times (as a metaphysical subject) to its contemporary status as a branch of physical science. Although there have been many attempts to understand it, they were not as physical but an abstract idea since knowledge from

the sky was very much more limited than nowadays. Given this situation, as we mentioned above, it is almost impossible to have a model without some assumptions furnished by a theoretical framework or paradigm. And these paradigms lead us to new stages of discovery by new astronomical observations, or vice versa. Roger Bacon (1214-1294) was almost the first scientist to propose the theory of the universe which is governed by physical laws. The heliocentric cosmology, which is often regarded as the milestone of the modern cosmological paradigm and referred to as the Copernican Revolution, was suggested by Nicolaus Copernicus (1473-1543). It was also supported by Galileo Galilei (1564-1642) and Johannes Kepler (1571 -1630) added even more fuel to the Copernican Revolution. There had been some ideas to explain cosmological observations, but a coherent physical theory was still needed to combine the pieces of explanation. The theory of universal gravitation, which unified what seemed to be many individual physical phenomena, was first proposed by Isaac Newton (1642-1727). The theory of gravitation theories is key to any cosmological theory because, although the force of gravity is extremely weak among the fundamental forces, such as electromagnetism and nuclear forces, gravity is the dominant force on scales beyond those of galaxies. By gravitation, every particle in the universe attracts another particles, so the universe should be collapse into the centre of mass. In order to avoid collapse, Newton needed to assume that the universe is infinite Euclidean space filled with a homogeneous and isotropic matter distribution without centre which is perfect Cosmological Principle. In this universe, there is no special epoch; it has always been and will always be.

In spite of the empirical success of the Newtonian theory, an inevitable

question arises about the darkness of sky in the form of what is now called Olbers' paradox. If an uniform distribution of stars covers the whole sky up to some finite radius, the night sky should be as bright as the mean star surface, which is - of course - not true. So how can modern cosmology solve it? In fact, it turns out there are many routes to a resolution. Our Universe might not be finite, either in extent or duration. The distribution of stars through out space might not be uniform. The wavelength of radiation also increases with time.

The last idea arises from the expanding universe model which is a consequence of the geometrical revolution in the gravitation theory. The expanding universe allow us to trace the history back far enough and everything comes together as singularity. The explosion from such a beginning is called the Big Bang and it describes the evolution of the universe from singularity. The Big Bang theory was motivated and developed by both observations and theoretical consideration. In the 1920s, the possibilities of the expansion of the Universe was suggested by some theorists [1, 2] and Hubble discovered the correlation between distance and recession velocity which indicates the cosmic expansion [3]. Although the most direct evidence is the Hubble expansion seen in the redshift of galaxies, there are more pieces of observational evidence which support the Big Bang theory: The abundance of light elements and measurements of the cosmic microwave background [4] which we will discuss later of this section. The Big Bang model is based on two theoretical pillars, Einstein's general relativity [5] and the Cosmological Principle.

Theoretical Framework. The theoretical foundation of modern cosmology is established by Einstein's relativity, which includes three components: the explanation of the space-time geometry, the equations for the action of gravity, and a description of the properties of matter and energy. As Newton did for his theory, the Einstein's theory also necessary to make assumption about the system to make progress such as the Cosmological Principle which assume that our universe is homogeneous and isotropic. Space-times based on the Cosmological Principle must have the same geometry at each point on a surface of constant time. General relativity describes space-time by a metric and the homogeneous and isotropic universe can be presented by the Friedmann-Robertson-Walker metric such as

$$ds^{2} = c^{2}dt^{2} - a_{s}^{2}(t) \left[ \frac{dt^{2}}{1 - Kr^{2}} + r^{2}(d\theta^{2} + \sin\theta d\phi^{2}) \right].$$
 (1.1)

in polar coordinates. The K represents the curvature and obtain only three cases: i) the flat universe with a Euclidean geometry as K=0, ii) the closed universe with positively curved spatial surface as K>0 and iii) the negatively curved space of hyperbolic form as K<0. This metric contains a cosmic scale factor,  $a_s$ , which describes the size of the Universe.

Einstein's field equations can be written as

$$G_{ab} \equiv R_{ab} - \frac{1}{2}Rg_{ab} = T_{ab} - \Lambda g_{ab},$$
 (1.2)

with  $R_{ab}$  being the Ricci Tensor, R the Ricci scalar,  $T_{ab}$  the energy-momentum tensor and  $\Lambda$  the cosmological constant. Latin indices (a, b, c, ...) run from 0 to 3. The Einstein tensor,  $G_{ab}$ , which contains the derivatives of the metric, describes the action of gravity in the space-time. The energy momentum

tensor, describes the properties of matter. The Universe has expanded from a very hot state, and due to the creation of space them matter cools as in usual thermodynamics. In this context, it reveals the astonishing fact there is a direct connection between the global geometry of the Universe from the  $G_{ab}$  and its the matter (density) which is described by  $T_{ab}$ . Two equations arise as independent equations from different components of Einstein's equations for the FRW metric. From  $G_0^0$  we obtain the Friedmann's equation:

$$\left(\frac{\dot{a}_s}{a_s}\right)^2 = \frac{8\pi G}{3}\rho - \frac{Kc^2}{a_s^2} \tag{1.3}$$

Note that density  $\rho$  covers all components i.e. matter, radiation and dark energy (if we have). The other equation,  $G_i^i - 2G_0^0$ , gives the knowledge of acceleration in dynamics by following form:

$$\left(\frac{\ddot{a}_s}{a_s}\right) = -\frac{4\pi G}{3} \left(\rho + 3\frac{p}{c^2}\right). \tag{1.4}$$

The energy conservation equation,

$$\dot{\rho} = -3\frac{\dot{a}_s}{a_s} \left( \rho + \frac{p}{c^2} \right) \tag{1.5}$$

comes from  $T_{0;b}^b = 0$ . Those equations determine the time evolution of the scale factor  $a_s$ .

Paradox of the Big Bang. In spite of successes at resolving paradoxes arising from the Newtonian cosmology, the Big Bang alone is not a complete model since there are significant deficiencies within it. Current observational data tell us that the present Universe is very close to flat.

However, the flat geometry is an unstable situation under the Big Bang cosmology. If there is any deviation from flatness then the Universe will very quickly become more and more curved. Therefore, the fact of present flat geometry would require an extreme flatness in the early Universe. If the Universe did not have precisely the critical density, it lead to a Universe extremely different to which we see (The Flatness Problem). The second issue is related to the large scale isotropy. One of most important results from Cosmic Microwave Background (CMB) observation is our Universe is very isotropic. Regions of the sky seen in opposite directions from the observer seem to have been able to communicate with each other in order to reach the same temperature. However, in the context of the Big Bang cosmology, they could never have been in casual contact with each other and no physical process that would bring them to the same temperature since the light travel time between them exceeds the age of the universe (The Horizon Problem). Another problem with the standard Big Bang cosmology, much discussed in the 1980s, was the possible existence of magnetic monopoles, predicted by Grand Unified Theories to arise as topological defects generated during phase transitions in the early Universe. These monopoles would be expected to be produced in the hot early Universe, yet have never been observed (The Magnetic Monopole Problem).

Cosmic Inflation. An elegant solution to these problems is suggested by inflationary theory, in the form of an exponential expansion of the early Universe[7]. If it occurred, this rapid expansion would push large regions of space well beyond our observable region and drive the Universe to a very close to flat state since space-time expanded to an extent that its

curvature would be smoothed away. It also removes all point defects from the Universe in the same way such that expansion drives the flat geometry.

There is stage in the evolution of the universe during which its energy density is dominated by the action of a scalar quantum field,  $\Phi$ .

$$\rho c^2 = \frac{1}{2}\dot{\Phi}^2 + V(\Phi) \tag{1.6}$$

$$\rho c^{2} = \frac{1}{2}\dot{\Phi}^{2} + V(\Phi)$$

$$p = \frac{1}{2}\dot{\Phi}^{2} - V(\Phi)$$
(1.6)
(1.7)

Where the density,  $\rho$  and pressure, p depend on the potential,  $V(\Phi)$ .

By Heisenberg's Uncertainty Principle there would be quantum fluctuations during the inflationary phase which would be magnified to a cosmic scale. These fluctuation grew into the stars, galaxies and clusters that what we see today. Quantum fluctuations in the scalar field driving the expansion generate adiabatic density perturbation with particularly simple statistical properties that 'seed' cosmic structure formation [8, 18]. They would also generate an undetected background of primordial Gravitational Waves [9].

Hypothesis. We have scrutinized the theoretical framework of cosmology. As we mentioned earlier, the standard version of the Big Bang theory has been based on the assumption of a Cosmological Principle, which remains unproven. This, and other key assumptions involved in the standard framework, has been more-or-less completely accepted and used to obtain rather unexpected information about astrophysical processes going on in the Big Bang. Since we are unable to examine directly space-time itself,

or the distribution of matter in it, we simply do not have the astrophysical information needed to determine the veracity sufficiently.

As outlined above, modern cosmology has long been based on the Cosmological Principle as a hypothesis. Let us begin with the puzzle of inertia since it is easy to connect to Einstein's idea that the universe is both homogeneous and isotropic on sufficiently large scales what Milne (1935) called Einstein's 'Cosmological Principle'. At the early time, Ernst Mach (1838-1916) stated that the local motion, or the law of physics for a rotating reference frame, is determined by the large scale distribution of matter (Mach's principle). Einstein adopted his idea that inertial frames of reference are determined by distribution and motion of the matter in the universe. The Cosmological Principle includes the existence of the cosmic time at which all measurable properties are the same. This principle only applies to highly idealized models of the world, such as Friedmann-Robertson-Walker (FRW) models. On the other hand, the Copernican Principle is that we are not at the center of the universe. The Copernican Principle, together with isotropy, implies the Cosmological Principle since the isotropy does not necessarily mean homogeneity without additional assumption that we are not in a special place. The advantage of the Copernican Principle is that it is more flexible assumption which can be applied to realistic cosmological model.

The Cosmological Principle define the idealized universe model. However, it makes predictions about parts of the universe which are beyond observation. The Copernican Principle only states conditions in the observable part of

universe. Therefore, it is not able to apply further regions of the universe which it does not attempt to describe.

In recent days, the Cosmological Principle confront some fundamental question whether the Universe is really prepared in an isotropic. This challenge arise from observational results from the Cosmic Microwave Background.

Cosmic Microwave Background. The Universe is filled with a thermal radiation background, the Cosmic Microwave Background (CMB), which is distributed very isotropic and homogeneous on large scale. At a very early stage, our Universe had the state of thermal equilibrium which gave the black body radiation. As its temperature goes down by expansion photons were constantly reflected from free electrons (Thomson Scattering), therefore, it occurs our Universe to opaque from light. As the temperature went down to a few thousand Kelvin, electron and nuclei started to combine to atoms (recombination). When most of electrons had recombined, at the stage of last scattering, radiation decoupled from matter since photons scatter not frequently from neutral atoms. What we see today is the photons from the epoch, last scattering surface. Since energy of photons was redshifted by expansion of the Universe the photons now fall into microwave region. Although the temperature of the CMB is 'almost' uniform at 2.7 K, there are very small variations on the order of  $10^{-5}K$ . These correspond to areas of various density fluctuation in the early universe.

The CMB is one of the most important pieces of evidence for the hot Big Bang model and provides crucial observational information on the origin, nature and evolution of density fluctuations which are thought to give rise to galaxies and scale structure in the Universe. Big steps in CMB observation have been made since the early 1990s from satellites: The Cosmic Background Explore (COBE) satellite revealed an accurate black-body radiation spectrum around 2.73 K and detected for the fist time fluctuations in the CMB [14]. The Wilkinson Microwave Anisotropy Probe (WMAP) also released the results that most accurate values of the cosmological parameters [15]. The results from satellite data are largely consistent with the concordance  $\Lambda$  Cold Dark Matter ( $\Lambda$ CDM) model, however there are some interesting deviations from it on the large scale. Although, from predictions of inflation, homogeneous and isotropic universe with Gaussian fluctuation is basis for the fundamental framework, our Universe seems neither perfectly isotropic nor Gaussian. At least three instances of anomalous behaviour have been reported, which we discuss in the next Chapter. The research presented in this thesis was motivated to explain these oddities on the basis of models in which the assumption of isotropy is broken, i.e. in cosmological Bianchi type models.

# Chapter 2

## Anisotropic cosmology:

## Bianchi models

#### 2.1 Introduction

Precise measurements of the temperature anisotropies of the Cosmic Microwave Background (CMB), particularly those from the Wilkinson Microwave Anisotropy Probe (WMAP) [15, 16], form the sturdiest foundations of the current ("concordance") cosmological model describing a universe dominated by cold dark matter (CDM) and a cosmological constant [17], and therefore known as ΛCDM for short. It is an essential component of this model that the primordial metric perturbations that gave rise to the galaxies and large-scale structure we observe around us today should be Gaussian and statistically homogeneous (i.e. stationary) [18, 19, 20] and

this means that the temperature fluctuations observed in the CMB should be Gaussian and statistically isotropic.

Detailed analysis of the WMAP data has shown that any departures from the standard framework are small and of uncertain statistical significance. Although some anomalous behaviour has been reported [21], there remains no clear evidence of primordial non-Gaussianity, but there are several indications of departures from statistical anisotropy across the CMB sky. Among the interesting phenomena revealed by detailed analyses of the pattern of CMB temperature fluctuations are an extremely cold spot [22, 23, 24, 25, 26, 27, 28], unusual alignments between large-scale harmonic modes of the temperature pattern [29, 30, 31, 32, 33, 34, 35, 36, 37, 38, 39] (sometimes dubbed "The Axis of Evil") and a global hemispherical power asymmetry [40, 41, 42, 43, 44].

One must not get carried away with these features because they are - almost without exception - based on a posteriori evaluations of statistical significance. If the occurrence of an anomalous feature A in a given model M is  $P(A|M) \simeq 0.001$  (say) then that does not necessarily mean that the probability of the model given that the anomaly is observed P(M|A) is similarly low. One has to take into account all the other data that are not anomalous before deciding on a true measure of the significance of a departure. Attempts to do this rigorously have generally confirmed that current observations are not sufficiently compelling to suggest that the standard model needs to be abandoned [45, 46, 47, 48]. Moreover, other analyses suggest the further possibility that the WMAP temperature fluctuations may be affected by foregrounds or other systematic problems [49, 50, 51, 52]. Even

slight effects of this type could seriously hamper our attempts to uncover evidence of physics beyond the standard model.

But, although the evidence for the examples of global asymmetry discussed above is by no means overwhelming, taken together they do at least suggest the possibility that we may live in universe which is described by a background cosmology that is globally anisotropic, i.e. one not described by a Friedmann-Robertson-Walker (FRW) model and it is therefore incumbent upon us to consider alternatives to the standard model in order to learn best how to use the data to confirm or rule out variations on the standard cosmology.

The approach we follow here is to study the Bianchi models, i.e. cosmological models based on exact solutions to Einstein's General Theory of Relativity involving homogeneous but not necessarily isotropic spatial sections. The Bianchi classification groups all possible spatially homogeneous but anisotropic relativistic cosmological models into types depending on the symmetry properties of their spatial hypersurfaces [53, 54]; we discuss these models in more detail later in this thesis.

The Bianchi models are not particularly strongly motivated from the point of view of fundamental physics, but do nevertheless represent a promising and potentially profitable first step away from the standard cosmological framework. For example, it has been known for some time that interesting localized features in the CMB temperature pattern can occur in Bianchi models with negative spatial curvature [55, 56, 57, 58, 59, 60]. The physical origin of such features lies in the focusing effect of space on the geodesics

that squeezes the pattern of the anisotropic radiation field into a small region of the sky. The observed lack of large-scale asymmetries in the CMB temperature has in the past been used to place constraints on the global rotation and shear allowed in Bianchi models [60, 61, 62]. More recently, however, attention has shifted to the possibility of using the additional parameters available in such models to reproduce a cold spot such as that claimed to exist in the WMAP data. Since we now know that our Universe is close to isotropic, attention has focussed on the subset of the Bianchi types that contain the FRW model as a limiting case. The model which appears to best able to reproduce the anomalous cold spot is the Bianchi VII<sub>h</sub> case [63, 64, 65, 66, 67], although Bianchi V also has negatively curved spatial sections and can therefore, in principle, also produce localised features [68].

However, as well as forming distinctive features in the temperature pattern, anisotropic cosmological models also generate characteristic signatures in the polarized component of the background radiation. Thomson scattering generates polarization as long as there is a quadrupole anisotropy in the temperature field of the radiation incident upon the scattering particle. In the concordance cosmology the temperature and polarization patterns are (correlated) stochastic fields arising from their common source in scalar and tensor perturbations arising from inflation. In a Bianchi cosmology, however, the patterns are coherent and have a deterministic relationship to one another owing to their common geometric origin. It has recently been shown [68, 69, 70] that only in special cases are the properties of the polarization field produced in Bianchi VII<sub>h</sub> consistent with the latest

available WMAP polarization data [71] because such models generally involve a large odd-parity (B-mode) [72, 73] contribution that exceeds the experimental upper limit.

But their ability to produce localized features is not the only reason to be interested in the temperature and polarization patterns produced in Bianchi models. For example, history provides a host of connections between these models and the understanding of the interaction between electromagnetic radiation and gravitational waves [74, 75, 76, 77, 78, 79].

Our aim in this chapter is to give a relatively gentle introduction to the Bianchi models. Our aim in doing this is neither to provide an exhaustive set of alternatives to the standard cosmology nor to perform a detailed statistical analysis of the patterns we calculate. Instead we plan to elucidate some of the general properties of the radiation field in anisotropic cosmological models belonging to the different Bianchi types.

The outline is as follows. In the next section we describe the Bianchi classification in general terms for the benefit of the non-expert. In section 3 we introduce the specific formalism of Bianchi cosmological models, i.e. exact solutions of the Einstein equations involving space-times with symmetries described by the various Bianchi types.

#### 2.2 Bianchi Spaces

In the Friedmann models on which the standard Big Bang cosmology is based, hypersurfaces of constant time are defined to be those on which the matter density is the same throughout space. We can construct a more general definition of homogeneity by requiring that all comoving observers see essentially the same version of cosmic history. In mathematical terms this means that there must be some symmetry that relates what the Universe looks like as seen by observer A to what is seen in a coordinate system centered on any other observer B. The possible space-times consistent with this requirement possess symmetries that can be classified into into the Bianchi types.

The Bianchi classification is based on the construction of space-like hypersurfaces upon which it is possible to define at least three independent vector fields,  $\xi_i$ , that satisfy the constraint

$$\xi_{i;j} + \xi_{j;i} = 0. (2.1)$$

This is called Killing's equation and the vectors that satisfy it are called Killing vectors; the semicolons denote covariant derivatives;  $i, j, k, \ldots$  run from 1 to 3. Suppose the Killing vectors are denoted  $\xi_i$ . The commutators of the  $\xi_i$  are defined by

$$[\xi_i, \xi_j] \equiv \xi_i \xi_j - \xi_j \xi_i = C_{ij}^k \xi_k, \tag{2.2}$$

where the  $C_{ij}^k$  are called structure constants. These are antisymmetric, in the sense that,

$$C_{ij}^{k} = -C_{ji}^{k}. (2.3)$$

One can understand how the structure constants arise by considering symmetry transformations. In three dimensions, spatial homogeneity is related

to the existence of three independent sets of curves with tangent vectors  $\xi_i$ . An infinitesimal symmetry transformation takes an arbitrary point P (with coordinates  $x_i$ ) to the point P' with coordinates  $x_i + \delta x_i$ , where

$$\delta \mathbf{x} = \xi_{\mathbf{P}} \delta t \tag{2.4}$$

for  $\xi_{\rm P}$  some linear combination of the  $\xi_i$  defined at P. The same symmetry transformation takes the tip of an arbitrary infinitesimal vector  $\zeta_{\rm P} \delta s$  at P to a new position  $\xi_{\rm P} + \zeta_{\rm P} \delta s \delta t$  at P'. This means that

$$\zeta_{\rm P}\delta s \to \zeta_{\rm P'}'\delta s = \zeta_{\rm P}\delta s + \xi_{\rm P+\zeta_{\rm P}\delta s}\delta t - \xi_{\rm P}\delta t.$$
 (2.5)

It is now possible to compare the transformed vector  $\zeta'_{P'}$  with  $\zeta_{P'}$ , the 'actual' vector field defined at P'. The difference between the two vectors is the Lie derivative of  $\zeta$  taken along  $\xi$ :

$$\mathcal{L}_{\xi}\zeta \equiv \lim_{\delta t \to 0} \frac{\zeta_{P'}' - \zeta_{P}}{\delta t} = \xi \cdot \nabla \zeta - \zeta \cdot \nabla \xi. \tag{2.6}$$

This tells us, roughly speaking, by how much we must turn a vector after it is carried by a symmetry transformation from P to P' in order for it to point in the same direction as it did before the transformation.

Instead of choosing an arbitrary vector we can now take one of the  $\xi_i$ , and instead of an arbitrary direction we transform it along another of the  $\xi_i$ . The type of space is specified by the Lie derivatives obtained for this type of operation:

$$\mathcal{L}_{\xi_i} \xi_i = C_{ij}^k \xi_k; \tag{2.7}$$

since it is defined as the difference between two vectors the Lie derivative must itself be a vector and so it can be expressed as a linear combination of the three independent basis vectors. This gives us the structure constants we described above.

The set of L Killing vectors will have some L-dimensional group structure, say  $G_L$ , that depends on the equivalence classes of the structure constants  $C_{ij}^k$ . This is used to classify all spatially homogeneous cosmological models. The most useful form of this classification proceeds as follows. On any particular space-like hyper-surface, the Killing vector basis can be chosen so that the structure constants can be decomposed as

$$C_{ij}^{k} = \epsilon_{ijl} n^{lk} + \delta_j^k a_i - \delta_i^k a_j, \tag{2.8}$$

where  $\epsilon_{ijk}$  is the total antisymmetric tensor and  $\delta_i^j$  is the Kronecker delta. The tetrad basis can be chosen to diagonalise the tensor,  $n^{ij} = \text{diag}(n_1, n_2, n_3)$  and to set the vector,  $a_i = (a, 0, 0)$ . Then Jacobi identites are simply  $n_1 a = 0$  from equation (2.10) in tetrad basis. The possible combinations of  $n_i$  and a then fix the different Bianchi types according to the Table 2.1.

It is interesting also to think about the *generality* of the different types. This can be expressed in terms of the dimension p of the Bianchi group, which gives the dimension of the orbit of  $C_{ij}^k$  as a subset of all 9 of the distinct components. The Killing vectors must satisfy the Jacobi identities, so

$$\epsilon^{ijk}\left[\left[\xi_{i},\xi_{j}\right],\xi_{k}\right] = 0. \tag{2.9}$$

Bianchi Type	Class	a	$n_1$	$n_2$	$n_3$
I	A	0	0	0	0
II	Α	0	+	0	0
$VI_0$	A	0	0	+	-
$VII_0$	A	0	0	+	+
VIII	A	0	-	+	+
IX	Α	0	+	+	+
IV	В	+	0	0	+
V	В	+	0	0	0
$ VI_h $	В	+	0	+	_
$VII_h$	В	+	0	+	+

TABLE 2.1: The Bianchi types shown in terms of whether the various parameters used to construct the classification are zero, positive or negative; the designation of Class A or Class B depends on whether a = 0, or not, respectively. The parameter h is defined by  $h = a^2/n_1n_2$ . The spaces of particular interest in this paper are I, V, VII<sub>0</sub>, VII<sub>h</sub> and IX because these contain the isotropic FRW spaces as limiting cases; the others are shown just for completeness.

This implies that

$$n^{ij}a_j = 0, (2.10)$$

so that the orbits of any particular group type are at most six-dimensional. The (isotropic) spaces that feature in the Friedmann models have  $G_6$  symmetry groups with  $G_3$  subgroups, so that the zero curvature (K = 0) FRW model can be thought of as a special case of Bianchi Types I or VII<sub>0</sub>. Likewise the open (K < 0) FRW model is a special case of types V or VII<sub>h</sub>. The closed FRW case (K > 0) is a special case of Bianchi type IX.

We are interested in cosmological models that are close to the completely isotropic case described by the FRW metric, but not all the Bianchi types contain this as a special limiting case [53, 54]. Those that do are types I, V, VII<sub>0</sub>, VII<sub>h</sub> and IX; we do not discuss the other cases any further in this

Type	*R	K	
I	0	0	Flat
V	$-6a^{2}$	< 0	Open
$VII_0$	$-\frac{1}{2}(n_2-n_3)^2$	0	Flat
$VII_h$	$(-6a^2 - \frac{1}{2}(n_2 - n_3)^2)$	< 0	Open
IX	$n_1 n_2 + \tilde{n_1} n_3 + n_2 n_3 - \frac{1}{2} (n_1^2 + n_2^2 + n_3^2)$	> 0	Closed

TABLE 2.2: Dependence of the scalar curvature of the spatial sections  ${}^*R$  on the parameters a and  $n_i$  involved in the construction of the Bianchi classification for those models with an FRW limit.

thesis. Bianchi I and Bianchi  $VII_0$  are spatially flat, Bianchi IX is positively curved and Bianchi types V and  $VII_h$  have negative spatial curvature. The "open" (i.e. negatively curved) cases are of particular interest as they permit the focussing of anisotropic patterns into small regions of the sky. The scalar curvature (Ricci scalar) of the spatial sections which is given in terms of the Bianchi parameters as

\*
$$R = -\frac{1}{2} \left( (n_1 - n_2)^2 + (n_1 - n_3)^2 + (n_2 - n_3)^2 \right) + \frac{1}{2} \left( n_1^2 + n_2^2 + n_3^2 \right) - 6a^2.$$
 (2.11)

For Bianchi V we have  $n_1 = n_2 = n_3 = 0$  so that  $R = -6a^2$ . In Bianchi VII<sub>h</sub> we have  $n_1 = 0$  but  $n_2 \neq 0$  and  $n_3 \neq 0$ ; the parameter h is defined by  $h = a^2/n_2n_3$ , it is related to the parameter  $x_{para}$  which defines the 'spiralness' of the temperature patterns,

$$x_{para} = \sqrt{\frac{h}{1 - \Omega_0}} \tag{2.12}$$

For reference, the scalar curvature of the spatial sections of all the models we discuss hereafter are shown in Table 2.2.

The models we consider have a single preferred axis of symmetry. The alignment of the shear eigenvectors relative to this preferred axis determines not only the dynamical evolution of the model through the field equations, but also the temperature and polarization pattern which, as we shall see, gets imprinted into the cosmic background radiation.

#### 2.3 Bianchi Cosmologies

#### **2.3.1** Basics

The models we consider are based on Einstein's general theory of relativity and we use the field equations in equation (1.2). In terms of a coordinate system  $x^a$ , the metric  $g_{ab}$  is written

$$ds^{2} = g_{ab}dx^{a}dx^{b} = (h_{ab} - u_{a}u_{b})dx^{a}dx^{b}, (2.13)$$

where  $u^a$  is the fluid velocity;  $h_{ab}$  is the projection tensor; the signature of  $g_{ab}$  is (-+++). As we have already explained, the components of the metric  $g_{ab}$  describing a Bianchi space are invariant under the isometry generated by infinitesimal translations of the Killing vector fields. In other words, the time-dependence of the metric is the same at all points. The Einstein equations relate the energy-momentum tensor  $T_{ab}$  to the derivatives of  $g_{ab}$  so if the metric is invariant under a given set of operations then so are the physical properties encoded in  $T_{ab}$ .

Before proceeding further, let us comment further on the degree of generality of the various Bianchi models which we touched on in the previous section. An alternative way to quantify this, rather than looking at the group structure, is to work out the number of arbitrary constants needed to specify the solutions. This seems more interesting from a physical point of view, as we are interested in the solutions to the field equations rather than the groups themselves. The number of arbitrary constants depends on the form of the energy-momentum tensor. In Table 2.3 we give the results for vacuum and perfect fluid equations of state. The appearance of h = -1/9 as a special case in this table relates to the fact that two of the Einstein constraint equations become null identities for this particular choice of h. From the Table 2.3 it emerges that the "most general" vacuum solutions are types VIIh, VIh, VIII, VIh=-1/9 and IX, all of which have four arbitrary parameters. The least general is the Bianchi Type I vacuum solution, which has only one.

For cases describing perfect fluids the situation is a little more subtle. One would expect to have four additional parameters to specify these compared to the vacuum solutions, but the Table 2.3 shows that s=r+4 is not always the case. This is the case because the Einstein equations place additional restrictions on the form of  $T_{ab}$  allowed in Types I and II. For example, if a perfect fluid is added to the vacuum Type I solution then the form of the metric requires all the time-space components of the Ricci tensor to be identically zero. This means that the energy-momentum tensor  $T_{ab}$  must have

$$T_{0a} = 0. (2.14)$$

Bianchi Type	Group Dimension	Vacuum	Fluid
	p	r	s
I	0	1	2
II	3	2	5
$VI_0$	5	3	7
VII <sub>0</sub>	6	4	8
VIII	6	4	8
IX	6	4	8
IV	5	3	7
V	3	1	5
$VI_h$	6	4	8
$VII_h$	6	4	8
$VI_{h=-1/9}$	6	4	7

TABLE 2.3: The Bianchi types shown in terms of the group dimension p and number of arbitrary constants needed to specify the model on a given constant time surface, in vacuum (r) and with a perfect fluid equation of state (s).

This in turn means that the matter must be comoving, i.e. its velocity is  $u_a = \delta_a^0$ . Only one free parameter is therefore needed to specify the solution, the energy density  $\rho$ . The perfect fluid case of Bianchi VI<sub>h=-1/9</sub> is also peculiar, in that it is not as general as Bianchi VI<sub>h</sub>, VII<sub>h</sub>, VIII or IX because the degeneracy described above only appears in vacuum.

#### 2.3.2 Example: The Kasner Solution

General solutions in closed form of the Einstein equations are only known for some special cases of the Bianchi types, which demonstrates the difficulty of finding meaningful exact solutions in situations of restricted symmetry. There is, however, one very well known example - the Kasner solution [84]- which is a useful illustration of the sort of behaviour one can obtain. This solution belongs to Bianchi type I. The Kasner metric has the

form

$$ds^{2} = dt^{2} - X_{1}^{2}(t)dx_{1}^{2} - X_{2}^{2}(t)dx_{2}^{2} - X_{3}^{2}(t)dx_{3}^{2}.$$
 (2.15)

Substituting this metric into the Einstein equations (with  $\Lambda=0$  and a perfect fluid with pressure p and density  $\rho$ ) yields

$$\frac{\ddot{X}_i}{X_i} - \left(\frac{\dot{X}_i}{X_i}\right)^2 + 3\left(\frac{\dot{X}_i}{X_i}\right)\left(\frac{\dot{a}_s}{a_s}\right) = \frac{1}{2}\left(\rho - p\right),\tag{2.16}$$

in which  $a_s^3 = X_1 X_2 X_3$ . Note that this emerges from the diagonal part of the Einstein equations so the summation convention does not apply. One also obtains

$$\frac{\dot{X}_1 \dot{X}_2}{X_1 X_2} + \frac{\dot{X}_2 \dot{X}_3}{X_2 X_3} + \frac{\dot{X}_3 \dot{X}_1}{X_3 X_1} = \rho. \tag{2.17}$$

This is easy to interpret: the spatial sections expand at a rate  $\dot{X}_i/X_i$  in each direction. The mean rate of expansion is just

$$\frac{\dot{a}_s}{a_s} = \frac{1}{3} \left( \frac{\dot{X}_1}{X_1} + \frac{\dot{X}_2}{X_2} + \frac{\dot{X}_3}{X_3} \right). \tag{2.18}$$

In the neighbourhood of an observer at the centre of a coordinate system  $x_i$ , fluid particles will move with some velocity  $u_i$ . In general,

$$\frac{\partial u_i}{\partial x_j} = \frac{1}{2} \left( \frac{\partial u_i}{\partial x_j} - \frac{\partial u_j}{\partial x_i} \right) + \frac{1}{2} \left( \frac{\partial u_i}{\partial x_j} + \frac{\partial u_j}{\partial x_i} \right) = \omega_{ij} + \theta_{ij}, \tag{2.19}$$

where  $\omega_{ij}$  is the rate of rotation: in more familiar language, the vorticity vector  $\omega_i = \epsilon_{ijk}\omega_{jk}$  which is just the curl of  $u_i$ . The tensor  $\theta_{ij}$  can be decomposed into a diagonal part and a trace-free part according to

$$\theta_{ij} = \frac{1}{3}\delta_{ij}\theta + \sigma_{ij},\tag{2.20}$$

where  $\sigma_{ii} = 0$ . In this description  $\theta$ ,  $\sigma_{ij}$  and  $\omega_{ij}$  respectively represent the expansion, shear and rotation of a fluid element. In the Kasner model we have

$$\theta = 3\frac{\dot{a}_s}{a_s} \tag{2.21}$$

and

$$\omega_{ij} = 0. (2.22)$$

As we shall see below, more complicated Bianchi models have non-zero rotation. We can further write evolution equations for

$$\sigma_i = \frac{\dot{X}_i}{X_i} - \frac{\dot{a}_s}{a_s}.\tag{2.23}$$

In particular we get

$$\dot{\sigma}_i + \theta \sigma_i = 0 \tag{2.24}$$

which can be immediately integrated to give

$$\sigma_i = \frac{\Sigma_i}{a_s^3},\tag{2.25}$$

where the  $\Sigma_i$  are constants such that  $\Sigma_1 + \Sigma_2 + \Sigma_3 = 0$ . The Kasner solution itself is for a vacuum  $p = \rho = 0$ , which has a particularly simple behaviour described by  $X_i = A_i t^p$  where  $p_1 + p_2 + p_3 = p_1^2 + p_2^2 + p_3^2 = 1$ . Notice that in general these models possess a shear that decreases with time. They therefore tend to behave more like an FRW model as time goes on. Their behaviour as  $t \to 0$  is, however, quite complicated and interesting.

#### 2.3.3 Tetrad Frame

It is convenient to follow [54], introducing a tetrad basis constructed from a local coordinate system  $x^{\alpha}$  by

$$\mathbf{e}_a = e_a^\alpha \frac{\partial}{\partial x^\alpha} \tag{2.26}$$

such that

$$g_{ab} = e_a^{\alpha} e_b^{\beta} g_{\alpha\beta} = e_a^{\alpha} e_{b\alpha} = \text{diag}(-1, +1, +1, +1)$$
 (2.27)

meaning that the tetrad basis  $\mathbf{e}_a$  is orthonormal. The functions  $e_a^{\alpha}$  are components of the vector  $\mathbf{e}_a$  with respect to the basis  $\partial/\partial x^{\alpha}$  and Greeks indices,  $\alpha, \beta, \gamma, \ldots$ , are coordinate one running from 0 to 3. The Ricci rotation coefficients are defined by

$$\Gamma_{abc} = e_a^{\alpha} e_{c\alpha;\beta} e_b^{\beta}. \tag{2.28}$$

Semicolons denote covariant derivatives. In general, the operators defined by equation (2.26) do not commute: they generate a set of relations of the form

$$[\mathbf{e}_a, \mathbf{e}_b] = \gamma^c_{\ ab} \mathbf{e}_c. \tag{2.29}$$

These Ricci rotation coefficients and the commutation functions  $\gamma^a_{\ bc}$  are linear combinations of the other:

$$\Gamma_{abc} = \frac{1}{2} (\gamma_{abc} + \gamma_{cab} - \gamma_{bca}). \tag{2.30}$$

The matter flow is described in terms of the expansion  $\theta_{ab}$  and shear  $\sigma_{ab}$ :

$$u_{a;b} = \omega_{ab} + \theta_{ab} - \dot{u}_a u_b$$

$$\sigma_{ab} = \theta_{ab} - \frac{1}{3}, \qquad (2.31)$$

where  $\theta = Tr(\theta_{ab}) = \theta_{aa}$  and the magnitude of the shear is  $\sigma^2 = \sigma^{ab}\sigma_{ab}/2$ . We now take the time-like vector in our basis to be the fluid flow velocity so that  $u^a = \delta^a_0$  and  $u_a = -\delta^0_a$ . The remaining space-like vectors form an orthonormal triad, with a set of commutation relations like that shown in equation (2.29) but with an explicit time dependence in the "structure constants" describing the spatial sections:

$$[\mathbf{e}_i, \mathbf{e}_j] = \gamma_{ij}^k(t)\mathbf{e}_k. \tag{2.32}$$

Without loss of generality we can write

$$\gamma^k_{ij} = \epsilon_{ijl} n^{lk} + \delta^k_i a_i - \delta^k_i a_j, \tag{2.33}$$

for the tensor  $n_{ij} = \text{diag}(n_1, n_2, n_3)$  and vector  $a_i = (a, 0, 0)$  in the tetrad frame. The four remaining free parameters are used to construct the Bianchi classification described briefly above, and more in detail elsewhere [53, 54, 80, 81, 82, 83].

### Chapter 3

# Background radiation in Bianchi universes

## 3.1 Radiation Transport in Anisotropic Cosmologies

Having established some general results about Bianchi models, we now turn to the problem of calculating the temperature and polarization patterns they produce. Our general method is to generalize the Boltzmann so that it can be applied to a complete description of photons traveling through a curved space-time. This requires that we set up radiation distribution functions that incorporate all the Stokes parameters needed to specific polarized radiation. We also need to include a source term that describes the effects of Thomson scattering by free electrons for the entire history from decoupling to the observed epoch.

#### 3.1.1 Radiation Description

Our expansion of the distribution functions into multipoles is based on the usual Stokes parameters, and on spin-weighted spherical harmonics. The Boltzmann equation for polarized radiation propagating through spacetime can be described by a (complex) photon distribution comprising components with spin-weights 0 and 2, i.e.

$$N \equiv \binom{N^0}{N^2} = \frac{1}{ch_P^4 \nu^3} \binom{I + iV}{Q - iU},\tag{3.1}$$

Where I, Q, U and V are the usual Stokes parameters that describe polarized radiation. As we shall see, however, V (which measures circular polarization) does not arise in this context. The degree of (linear) polarization is defined by

$$P = \frac{\sqrt{Q^2 + U^2}}{I}. (3.2)$$

The polarization orientation is described by an angle  $\chi$ , where

$$\chi = \frac{1}{2} \arctan \frac{U}{Q}. \tag{3.3}$$

When the nonrelativistic particle move in Euclidean space under a force field  $\mathbf{F}$  with coordinate  $\mathbf{x}$  and momenta  $\mathbf{p}$ , the version of the Liouville equation describing the evolution of a phase space volume is

$$\frac{\partial}{\partial t} + \frac{\mathbf{p}}{m} \cdot \nabla \mathbf{x} + \mathbf{F} \cdot \nabla_{\mathbf{p}} \tag{3.4}$$

and its relativistic form is

$$p^{a} \frac{\partial}{\partial x^{a}} - \Gamma^{a}{}_{bc} p^{b} p^{c} \frac{\partial}{\partial p^{a}}.$$
 (3.5)

The unpolarized part of the radiation distribution is described by spin-zero quantities, N (i.e. quantities invariant with respect to rotations around the ray direction  $k^i$ ). In terms of an affine parameter  $\lambda$  along the photon path one calculates the total change of N as

$$\frac{dN}{d\lambda} = p^a e_a^\alpha \frac{\partial N}{\partial x^\alpha} + \frac{\partial N}{\partial p^a} \frac{dp^a}{d\lambda}$$
 (3.6)

and the photon path  $p^a(\lambda)$  is determined by the geodesic equation expressed in the tetrad notation we introduced above as

$$\frac{dp^c}{d\lambda} = -\Gamma^c{}_{ab}p^a p^b \tag{3.7}$$

so that

$$\frac{dN}{d\lambda} = p^a e_a^\alpha \frac{\partial N}{\partial x^\alpha} - \Gamma^c{}_{ab} p^a p^b \frac{\partial N}{\partial p^c}$$
(3.8)

in which  $p^a \equiv (\varepsilon, \varepsilon k^i)$ .  $\varepsilon$  is energy of photon. If the change in N along a photon path arises from collisions only, one obtains the following equation

$$\frac{1}{\varepsilon} \frac{dN}{d\lambda} = e_0^{\alpha} \frac{\partial N}{\partial x^{\alpha}} + k^i e_i^{\alpha} \frac{\partial N}{\partial x^{\alpha}} - \varepsilon \gamma^0 \frac{\partial N}{\partial \varepsilon} + \frac{\gamma^i}{\sqrt{2}} (m^i \bar{\eth} + \bar{m}^i \bar{\eth}) N, \tag{3.9}$$

Where

$$\gamma^{a} = \Gamma^{a}_{00} + \Gamma^{a}_{0i}k^{i} + \Gamma^{a}_{i0}k^{i} + \Gamma^{a}_{ik}k^{i}k^{k}. \tag{3.10}$$

We use spin differential operator,  $\eth = -(\partial/\partial\theta + i/\sin\theta \cdot \partial/\partial\phi)$  [97]. In the case of polarized radiation we need to extend the description of the

radiation field to include both spin-0 and spin-2 components. This requires us to generalize N which can be decomposed into parts  $N^0$  and  $N^2$ . In the Boltzmann equation for  $N^2$  these give rise to additional terms from change of angles i.e.  $\theta$  and  $\phi$ , and extra rotation  $\psi$  of polarization (see A.1, A.5); From the relation between the spin 0 and 2 operators the angular derivative term is given as

$$\frac{\gamma^{i}}{\sqrt{2}}(m^{i}\bar{\eth}_{2} + \bar{m}^{i}\bar{\eth}_{2})N^{2} = 2i\cos\theta \frac{d\phi}{d\lambda}N^{2} + \frac{\gamma^{i}}{\sqrt{2}}(m^{i}\bar{\eth} + \bar{m}\bar{\eth})N^{2}. (3.11)$$

We must replace  $N^2$  to  $N^2e^{-2i\psi}$  for the relative twisting of the directions  $m^i$  and a parallel propagated direction. This adds to the Liouville equation a term such as

$$-2iN^{2}\frac{d\psi}{d\lambda} = -2i\cot\theta \frac{d\phi}{d\lambda}N^{2} - 2N^{2}m^{i}\bar{m}^{k}\varepsilon(\Gamma^{k}_{0i} + k^{l}\Gamma^{k}_{li}). \tag{3.12}$$

First two extra terms cancel out in the Liouville equation then, we obtain simplified form such as

$$\mathcal{D}_{A}N^{A} \equiv e_{0}^{\alpha} \frac{\partial N^{A}}{\partial x^{\alpha}} + k^{i} e_{i}^{\alpha} \frac{\partial N^{A}}{\partial x^{\alpha}} - \varepsilon \gamma^{0} \frac{\partial N^{A}}{\partial \varepsilon} + \vartheta N^{A} + \delta_{A}^{2} i N^{2} (\Gamma^{k}_{0i} \epsilon^{ikl} k^{l} + \Gamma^{k}_{li} k^{l} k^{m} \epsilon^{ikm}).$$
(3.13)

We used the antisymmetry of a and c in  $\Gamma^a{}_{bc}$  and the relation,  $\frac{1}{2}(m^l\bar{m}^j-\bar{m}^lm^j)=-\frac{i}{2}\epsilon^{ljk}k^k$  for obtaining the imaginary terms. The operator  $\mathcal{D}_A$  on the left hand side preserves spin weight (A=0,2); the corresponding angular operator is  $\vartheta=\gamma^i/\sqrt{2}(m^i\bar{\eth}+\bar{m}^i\eth)$ .

#### 3.1.2 Scattering

We obtain the Boltzmann equation by the addition of a source term which describe Thomson scattering by free electrons to the right hand side of the Liouville equation,

$$\mathcal{D}_A N^A = \tau (-N^A + J_A). \tag{3.14}$$

Where the optical depth  $\tau$  is  $n_e \sigma_T$ ,  $n_e$  is the free electron number density and  $\sigma_T$  is the Thomson scattering cross section (Note: A = 0, 2; summation over B but not over A). From the corresponding emission term for the Stokes parameters [98], it takes the form

$$J_A = \int [p_{AB}(\theta, \phi, \theta', \phi') N^B(\theta', \phi') + \hat{p}_{AB}(\theta, \phi, \theta', \phi') \bar{N}^B(\theta', \phi')] \frac{d\Omega'}{4\pi}. \quad (3.15)$$

Where  $p_{AB}$  is the scattering  $2 \times 2$  matrices which depend on  $\theta$ ,  $\phi$ , and  $\hat{p}_{AB}$  on  $\theta'$ ,  $\phi'$ . The elements of  $p_{AB}$  may be expanded in terms of spin-weighted polynomials  $k^i$ ,  $k^{ij}$  and  $m^{ij}$ :

$$p_{00} = \frac{1}{2} + \frac{3}{8}k^{ik}k^{ik'} + \frac{1}{2}k^{i}k^{i'},$$

$$p_{02} = \bar{p}_{02} = -\frac{3}{4}k^{ik}\bar{m}^{ik'},$$

$$p_{22} = \frac{3}{2}m^{ik}\bar{m}^{ik'},$$

$$\hat{p}_{00} = \frac{1}{2} + \frac{3}{8}k^{ik}k^{ik'} - \frac{1}{2}k^{i}k^{i'},$$

$$p_{20} = \hat{p}_{20} = -\frac{3}{4}m^{ik}k^{ik'},$$

$$\hat{p}_{22} = \frac{3}{2}m^{ik}m^{ik'}.$$
(3.16)

The emission term  $J_A$  contains only harmonics up to l=2, since all other terms vanish in virtue of the orthogonality relations for spherical harmonics

(see A.2):

$$J_{0} = {}^{Re}N_{0}^{0} + \frac{i}{3}k^{iIm}N_{i}^{0} + \frac{1}{10}k^{ikRe}N_{ik}^{0} - \frac{3}{10}k^{ikRe}N_{ik}^{2},$$

$$J_{2} = -\frac{1}{5}m^{ikRe}N_{ik}^{0} + \frac{3}{5}m^{ikRe}N_{ik}^{2}.$$
(3.17)

The radiation modes with  $l \leq 2$  are damped as well as re-radiated by Thomson scattering, while higher-order modes l > 2 are only damped.

#### 3.1.3 Transfer Equation

The Boltzmann equation describes the statistical distribution of one particle in a fluid. It is used to study how a fluid transports physical quantities. We now expand the distribution function in our Boltzmann equation in terms of multipole components:

$$N^{0} = N_{0}^{0} + N_{i}^{0} k^{i} + N_{ij}^{0} k^{ij} + \dots,$$

$$N^{2} = N_{ij}^{2} m^{ij} + \dots,$$
(3.18)

Where  $k^i$  expresses the three-dimensional ray direction, i.e.

$$k^{i} = (\cos\theta, \sin\theta\cos\phi, \sin\theta\sin\phi),$$

$$k^{ik} = k^{i}k^{k} - \frac{1}{3}\delta^{ik},$$

$$m^{i} = \frac{1}{\sqrt{2}} \left(\frac{\partial k^{i}}{\partial \theta} + \frac{i}{\sin\theta} \cdot \frac{\partial k^{i}}{\partial \phi}\right),$$

$$m^{ij} = m^{i}m^{k},$$
(3.19)

in which  $m^i k_i = 0, m^i \bar{m}_i = k^i k_i = 1$  and the bar indicates complex conjugate. The number of indices of the k and m polynomials are characterizes the multipole order of the corresponding contributions to anisotropy and polarization. The integration is over the surface of the unit sphere:

$$\int k^{i}k^{k}\frac{d\Omega}{4\pi} = \frac{1}{3}\delta^{ik},$$

$$\int k^{ij}k^{kl}\frac{d\Omega}{4\pi} = \frac{1}{15}\Big(\delta^{ik}\delta^{jm} + \delta^{im}\delta^{jk} - \frac{2}{3}\delta^{ij}\delta^{kl}\Big),$$

$$\int m^{ij}\bar{m}^{km}\frac{d\Omega}{4\pi} = \frac{1}{10}(\delta^{ik}\delta^{jm} + \delta^{im}\delta^{jk}) - \frac{1}{15}\delta^{ij}\delta^{km},$$

$$\int m^{ij}\bar{m}^{km}n^{r}\frac{d\Omega}{4\pi} = \frac{i}{30}(\delta^{ik}\varepsilon^{mjr} + \delta^{jk}\varepsilon^{mir} + \delta^{jm}\varepsilon^{kir} + \delta^{im}\varepsilon^{kjr}), (3.20)$$

where the integration is taken over the unit sphere.

We are now in a position to write down equations for the evolution of the components of the distribution function, as follows:

$$\begin{split} \dot{N}_{0}^{0} - \frac{1}{3}\zeta\Gamma^{0}{}_{kk}N_{0}^{0} - \frac{2}{15}\zeta\Gamma^{0}{}_{kl}N_{kl}^{0} - \frac{1}{3}\Gamma^{k}{}_{ll}N_{k}^{0} - \frac{2}{5}\Gamma^{0}{}_{kl}N_{kl}^{0} &= -\tau i^{Im}N_{0}^{0}, \\ \dot{N}_{i}^{0} + (\hat{A}_{i}^{k}\zeta + \hat{B}_{i}^{k})N_{k}^{0} + \hat{C}_{i}^{kl}N_{kl}^{0} &= -\tau \Big(^{Re}N_{i} + \frac{2}{3}i^{Im}N_{i}^{0}\Big), \\ \dot{N}_{ij}^{0} + \hat{E}_{ij}\zeta N_{0}^{0} + (\hat{D}_{ij}^{k}\zeta + \hat{H}_{ij}^{k})N_{k}^{0} + (\hat{F}_{ij}^{kl}\partial_{\varepsilon} + \hat{G}_{ij}^{kl})N_{kl}^{0} \\ &= -\tau \Big(\frac{9}{10}^{Re}N_{ij}^{0} + \frac{3}{10}^{Re}N_{ij}^{2} + i^{Im}N_{ij}^{0}\Big), \\ \dot{N}_{ij}^{2} - \frac{1}{3}\Gamma^{0}{}_{kk}\zeta N_{ij}^{2} + \hat{K}_{ij}^{kl}N_{kl}^{2} \\ &= -\tau \Big(\frac{1}{5}^{Re}N_{ij}^{0} + \frac{2}{5}^{Re}N_{ij}^{2} + i^{Im}N_{ij}^{2}\Big), \end{split} \tag{3.21}$$

Where we used in the definition of  $\zeta$ :

$$\zeta \equiv \frac{\partial (\ln N_0^0)}{\partial \ln \varepsilon} = \varepsilon \frac{\partial (\ln N_0^0)}{\partial \varepsilon}.$$
 (3.22)

The coefficients arising in the Boltzmann equation can be obtained in the following form

$$\hat{A}_{i}^{k} = \frac{1}{5} (\Gamma_{ik}^{0} - \Gamma_{ki}^{0} + \Gamma_{ll}^{0} \delta_{ik}),$$

$$\hat{B}_{i}^{k} = -\Gamma_{0i}^{k} + \frac{1}{5} (\Gamma_{ki}^{0} - 4\Gamma_{ik}^{0} + \Gamma_{l0}^{l} \delta_{ik}),$$

$$\hat{C}_{i}^{kl} = -\frac{2}{5} (\Gamma_{li}^{k} + \Gamma_{mm}^{k} \delta_{il} + 3\Gamma_{00}^{k} \delta_{li}),$$

$$\hat{D}_{ij}^{k} = \frac{1}{3} \Gamma_{0l}^{0} \delta_{ij} - \frac{1}{2} \Gamma_{0i}^{0} \delta_{lj} - \frac{1}{2} \Gamma_{0j}^{0} \delta_{li},$$

$$\hat{E}_{ij} = \frac{1}{3} \Gamma_{ll}^{0} \delta_{ij} - \frac{1}{2} \Gamma_{ij}^{0} - \frac{1}{2} \Gamma_{ji}^{0},$$

$$\hat{F}_{ij}^{kl} = \frac{2}{21} \Gamma_{kl}^{0} \delta_{ij} - \frac{1}{7} (\delta_{ki} \delta_{lj} \Gamma_{mm}^{0} + \Gamma_{ki}^{0} \delta_{jl} + \Gamma_{kj}^{0} \delta_{il}),$$

$$\hat{G}_{ij}^{kl} = \frac{2}{21} \Gamma_{kl}^{0} \delta_{ij} + \frac{2}{7} (\Gamma_{ki}^{0} \delta_{jl} + \Gamma_{kj}^{0} \delta_{il}) - \Gamma_{0i}^{k} \delta_{lj} - \Gamma_{0j}^{k} \delta_{li}$$

$$-\frac{5}{7} (\Gamma_{ik}^{0} \delta_{jl} + \Gamma_{jk}^{0} \delta_{il}) + \frac{2}{7} \Gamma_{mm}^{0} \delta_{ik} \delta_{jl}$$

$$\hat{H}_{ij}^{k} = -\frac{1}{2} \Gamma_{ij}^{k} - \frac{1}{2} \Gamma_{ji}^{k} + \frac{1}{3} \Gamma_{mm}^{k} \delta_{ij} + \frac{1}{2} \Gamma_{00}^{j} \delta_{ik} + \frac{1}{2} \Gamma_{00}^{i} \delta_{jk} - \frac{1}{3} \Gamma_{00}^{k} \delta_{ij},$$

$$\hat{K}_{ij}^{kl} = -\frac{2}{9} \Gamma_{kl}^{0} \delta_{ij} + \frac{1}{3} (\Gamma_{0i}^{k} + \Gamma_{i0}^{k}) \delta_{lj} + \frac{1}{3} (\Gamma_{0k}^{j} + \Gamma_{k0}^{j}) \delta_{li} + \frac{i}{3} \delta_{ki} \delta_{lj} \Gamma_{tr}^{s} \epsilon_{rst}.$$

$$(3.23)$$

Since  $k^{ij}$  and  $m^{ij}$  are both symmetric and traceless, it follows that  $N^0_{ij}$  and  $N^2_{ij}$  are too. The coefficients listed above must therefore be made symmetric and traceless on the index pairs ij and kl. Since the connections are also represented by kinematic quantities (see A.3) we may obtain the coefficients as different notations (see A.4).

Equations (3.21) describe the behavior of the lowest-order angular modes of a general radiation field in a general space-time, with two main assumptions. First, in the orthonormal frame, we assume that the "spatial" derivatives vanish for all quantities N of interest because of homogeneity.

Second, we assume that the radiation field is described by a Planck distribution at all times. These assumptions reduce the set of equations needed to a linear system of coupled ordinary differential equations with "time"-dependent coefficients. The patterns that are produced therefore depend both on the background cosmology and the initial conditions.

Thomson scattering does not affect the component  $^{Re}N_0^0$  but it does the term  $^{Im}N_0^0$  that describes circular polarization. The mode describing linear polarization,  $N_{ij}^2$ , is coupled to higher-order modes of the radiation field but not directly through  $N_0^0$ . Any non-zero term  $\hat{C}_i^{kl}$  would produce a dipole variation of the radiation distribution represented by  $N_i^0$  but no dipole can be produced this way in the particular case of Bianchi I (nor indeed for the FRW case). The presence of a dipole component is inevitable in other Bianchi models since, even with  $N_i^0 = 0$  initially,  $N_i^0$  becomes different from zero if  $\Gamma^0_{0i} \neq 0$  or if  $N_{kl}^0 \Gamma^k_{li} + N_{ik}^0 \Gamma^k_{ll}$  differs from zero. In a similar manner a quadrupole component can always be generated from the isotropic mode  $N_0^0$ , if  $E_{ik}$  is different from zero which means that the fluid flow possesses some kind of shearing motion.

It is clear from the system of equations (3.21) that a gravitational field alone is not able to generate polarization. Initially unpolarized radiation collisionlessly propagating in an arbitrary gravitational field must remain unpolarized. However, a quadrupole mode of unpolarized radiation generates a linear polarization component at l=2, if Thomson scattering is present. This is the standard mechanism by which polarization is generated from radiation anisotropies in the early Universe. Since a quadrupole mode of unpolarized radiation is generated from the isotropic component

if  $E_{ik} \neq 0$ , the cosmological gravitational field could therefore be indirectly responsible for generating polarization if it first generates a quadrupole anisotropy. Equations (3.21) also show that an initial monopole  $N_0^0$  produces a non-zero quadrupole  $N_{ij}^0$  via the shear  $\hat{E}_{ij} = -\sigma_{ij}$  and  $N_i^0$  is subsequently coupled with  $N_{ij}^0$  by  $\hat{C}_i^{kl}$ . The effect of shear on the radiation is to generate a quadrupole anisotropy by redshifting the it anisotropically; in some models, dipole and higher order multipoles would also arise.

To summarize, then. In order to get interesting higher-order patterns in the radiation background we must either have non-zero shear if there is no initial quadrupole or have non-zero initial quadrupole and monopole terms if there is no shear.

#### 3.1.4 Geodesic Equation

We now follow the follow the convention in ref. [56] to construct the equations describing geodesics in the models we consider. From each components of equation (3.7) time variation of  $\varepsilon$  and direction vector  $k^i$  have the form such as

$$\frac{dp^0}{d\lambda} = \frac{d\varepsilon}{d\lambda} = -\varepsilon^2 \gamma^0, \tag{3.24}$$

$$\frac{dp^{i}}{d\lambda} = \frac{d\varepsilon}{d\lambda}k^{i} + \varepsilon \frac{dk^{i}}{d\lambda} = -\varepsilon^{2}\gamma^{i}. \tag{3.25}$$

Using relations

$$dp^{i} = k^{i}d\varepsilon + \varepsilon dk^{i} = k^{i}d\varepsilon + \varepsilon \left(\frac{\partial k^{i}}{\partial \theta}d\theta + \frac{\partial k^{i}}{\partial \phi}d\phi\right), \tag{3.26}$$

And orthogonality of  $\partial k^i/\partial \theta$ ,  $\partial k^i/\partial \phi$  and  $k^i$ , we obtain the time variations for  $\theta$  and  $\phi$ :

$$\frac{d\theta}{d\lambda} = \frac{1}{\varepsilon} \frac{dp^i}{d\lambda} \frac{\partial k^i}{\partial \theta} = -\varepsilon \Gamma^i{}_{jk} k^j k^k \frac{\partial k^i}{\partial \theta}, \qquad (3.27)$$

$$\frac{d\phi}{d\lambda} = \frac{1}{\varepsilon} \frac{dp^i}{d\lambda} \frac{1}{\sin \theta} \frac{\partial k^i}{\partial \phi} = -\varepsilon \Gamma^i{}_{jk} k^j k^k \frac{1}{\sin^2 \theta} \frac{\partial k^i}{\partial \phi}, \tag{3.28}$$

Where we also neglect the effect shear which would make  $(\Gamma^0_{ij} = 0)$ . As final step, we obtain variation terms:

$$\frac{1}{\varepsilon} \frac{d\theta}{d\lambda} = \sin \theta [a + \cos \phi \sin \phi (n_3 - n_2)], \tag{3.29}$$

$$\frac{1}{\varepsilon} \frac{d\theta}{d\lambda} = \sin \theta [a + \cos \phi \sin \phi (n_3 - n_2)], \qquad (3.29)$$

$$\frac{1}{\varepsilon} \frac{d\phi}{d\lambda} = \cos \theta [n_1 - n_3 + (n_3 - n_2) \cos^2 \phi]. \qquad (3.30)$$

The polarization angle is more complicated (see A.6). The change of  $\psi$  is expressed by

$$\frac{1}{\varepsilon} \frac{d\psi}{d\lambda} = im^i \bar{m}^k \Gamma^k_{li} k^l - \cos\theta b_l \gamma^l = \frac{1}{6} n_s^s - n_k^i k^{ik} + \cos\theta \frac{1}{\varepsilon} \frac{d\phi}{d\lambda}.$$
(3.31)

Although  $\Gamma^k_{li}$  contains the Bianchi vector  $a_i$ , there are only Bianchi vector  $n_i$  components in the change of  $\psi$  since  $a_i k^l k^m \epsilon^{ilm} = 0$  by symmetry of l and m indices. Therefore, it means that this term does not give the different results between the models such as Type I and V or VII<sub>h</sub> and VII<sub>0</sub> for  $\psi$ variation i.e. polarization (see Table 3.1).

The term  $d\psi/d\lambda$  is important since it gives the mixing terms between the E and B modes in the Boltzmann equation.

Type	$\frac{1}{\varepsilon} \frac{d\theta}{d\lambda}$	$\frac{1}{arepsilon} \frac{d\phi}{d\lambda}$	$\frac{1}{arepsilon} \frac{d\psi}{d\lambda}$
I	0	0	0
V	$a\sin\theta$	0	0
$VII_0$	0	$-n\cos\theta$	$-n\cos^2\theta$
$VII_h$	$a\sin  heta$	$-n\cos\theta$	$-n\cos^2\theta$
IX	0	0	n

TABLE 3.1: The angle variations of Bianchi types. Note that we consider the FRW limits i.e. Bianchi vectors as  $n_i = n$ .

#### 3.2 Conclusions

We obtain the formalism in order to compute the temperature and polarization patterns produced in anisotropic relativistic cosmologies described by various Bianchi types. We constructed an appropriate description of the radiation field in terms of spin-0 and spin-2 components representing the unpolarized and polarized parts, respectively.

The basic point that emerges from this study is related to the physical origin of CMB polarization: radiation affected by Thomson scattering from an electron in a radiation field possessing a quadrupole anisotropy will inevitably be partially linearly polarized. In the context of standard cosmological models, the environment of different electrons varies owing to the presence of density inhomogeneities and a background of gravitational waves. These sources of variation are stochastic so the variations in the polarized component of the radiation field, though correlated with the temperature variations, are essentially incoherent. In Bianchi cosmologies, however, global homogeneity requires that each electron sees the same quadrupole. The polarized part of the radiation field is therefore coherent,

and is in a fixed relationship to the temperature variation (once the model is specified).

### Chapter 4

# Temperature and Polarization Patterns

In this chapter we will present representative examples of the temperature and polarization patterns produced in the models we have discussed, computed by numerically integrating the system of equations derived in previous chapter. The patterns generated depend on the parameters chosen for the model in question and also, as we have explained in the previous chapter, on the choice of initial data. In the following, primarily pedagogical, discussion we do not attempt to normalize the models to fit current cosmological observations but restrict ourselves to phenomenological aspects of the patterns produced. The overall level of temperature anisotropy depends on the choice of parameters in the Bianchi models that express the extent of its departure from the FRW form. Since we do not tune this to observations, the amplitude is arbitrary, as is the cosmic epoch attributed

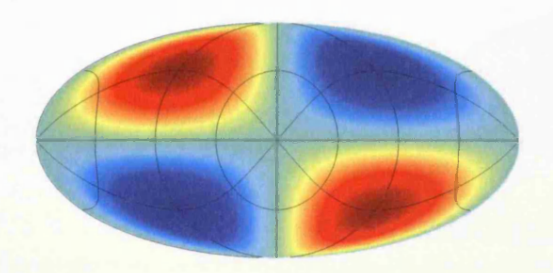


FIGURE 4.1: Initial configuration chosen for the temperature pattern. Where the initial conditions produce a pure quadrupole anisotropy of tesseral form, i.e. and l=2 spherical harmonic mode with m=1.

to each of the evolutionary stages. Moreover, the overall degree of polarization depends strongly on the ionization history through the optical depth  $\tau$  which appears in equation (3.14). We shall not attempt to model this in detail in this thesis either. What is important, however, is that the geometrical relationship between the temperature and polarization patterns does not depend on these factors; it is fixed by the geometric structure of the model, not on its normalization.

Of course we compute only the *coherent* part of the radiation field that arises from the geometry of the model. Any realistic cosmological model (i.e. one that produces galaxies and large-scale structure) must have density inhomogeneities too. Assuming these are of stochastic origin they would add incoherent perturbations on top of the coherent ones produced by the background model.

For illustrative purposes, in section 4.1, we have chosen cases where the initial conditions produce a pure quadrupole anisotropy of tesseral form, i.e. and l = 2 spherical harmonic mode with m = 1 as shown in Figure 4.1. We gratefully acknowledge the use of the Healpix software [85] in creating

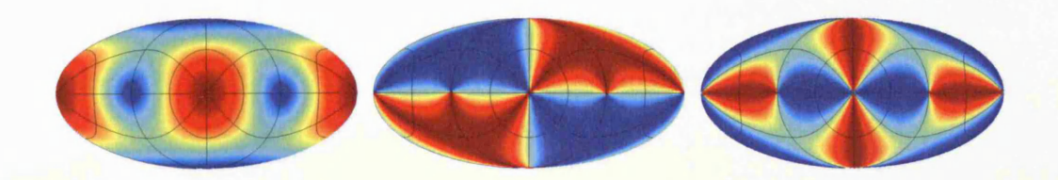


Figure 4.2: Polarization maps, i.e. degree of linear polarization (left), Stokes parameter Q (middle) and U (right) of Bianchi type I. The polarization patterns do not evolve with time.

this and all the other all-sky maps shown hereafter.

Other choices are, of course, possible. A quadrupole with m=0 would produce a zonal pattern, and one with m=2 would be a sectoral mode [52]; these choices are discussed at some length in ref. [70]. One could also generate more complicated patterns by having an observer who is not at rest in the frame we are using, which would introduce an additional dipole anisotropy. We will discuss this possibility in section 4.3.

#### 4.1 Bianchi Maps

The simplest case of all is obviously that of Bianchi I, but this is nevertheless of some interest because a Universe of this type could in principle account for the presence of a low quadrupole [86, 87]. In this example the temperature pattern does not evolve at all with time, so one can simply treat the initial quadrupole as a free parameter. The polarization patterns arising in this model, which do not evolve with time either, are shown in Figure 4.2.

We next turn our attention to Bianchi types V, VII<sub>h</sub> and VII<sub>0</sub>. These models have a single preferred axis of symmetry. The alignment of the shear eigenvectors relative to this preferred axis determines not only the dynamical evolution of the model through the field equations, but also the temperature and polarization pattern which, as we shall see, gets imprinted into the cosmic background radiation. Figure 4.3 shows (from bottom to top) the time evolution of the temperature pattern in these models. Note that, in Type V (left), the initial quadrupole retains its shape but gets focussed into a patch of decreasing size as time goes on. This is due to the effect of negative spatial curvature. In Bianchi Type VII<sub>0</sub> (right) the effect of rotation and shear is to twist the initial quadrupole into a spiral shape that winds up increasingly as the system evolves. In the middle case, Bianchi Type VII<sub>h</sub> we have a combination of the two cases either side: there is both a focussing and a twist. This case produces the most complicated temperature pattern.

In the following three figures we examine the polarization pattern produced in the models shown in Figure 4.2. First, in Figure 4.4, we have Bianchi V. These results show that while the polarization pattern alters with time in this case, its general orientation on the sky does not (as is the case with the temperature pattern). The implications of this for the production of cosmological B-mode polarization will be discussed by next section.

Figure 4.5 shows an example of Bianchi Type  $VII_h$ . Note the prodigious twisting of the polarized component of the radiation field, as well as a concentration of the degree of polarization defined by equation (3.2). This

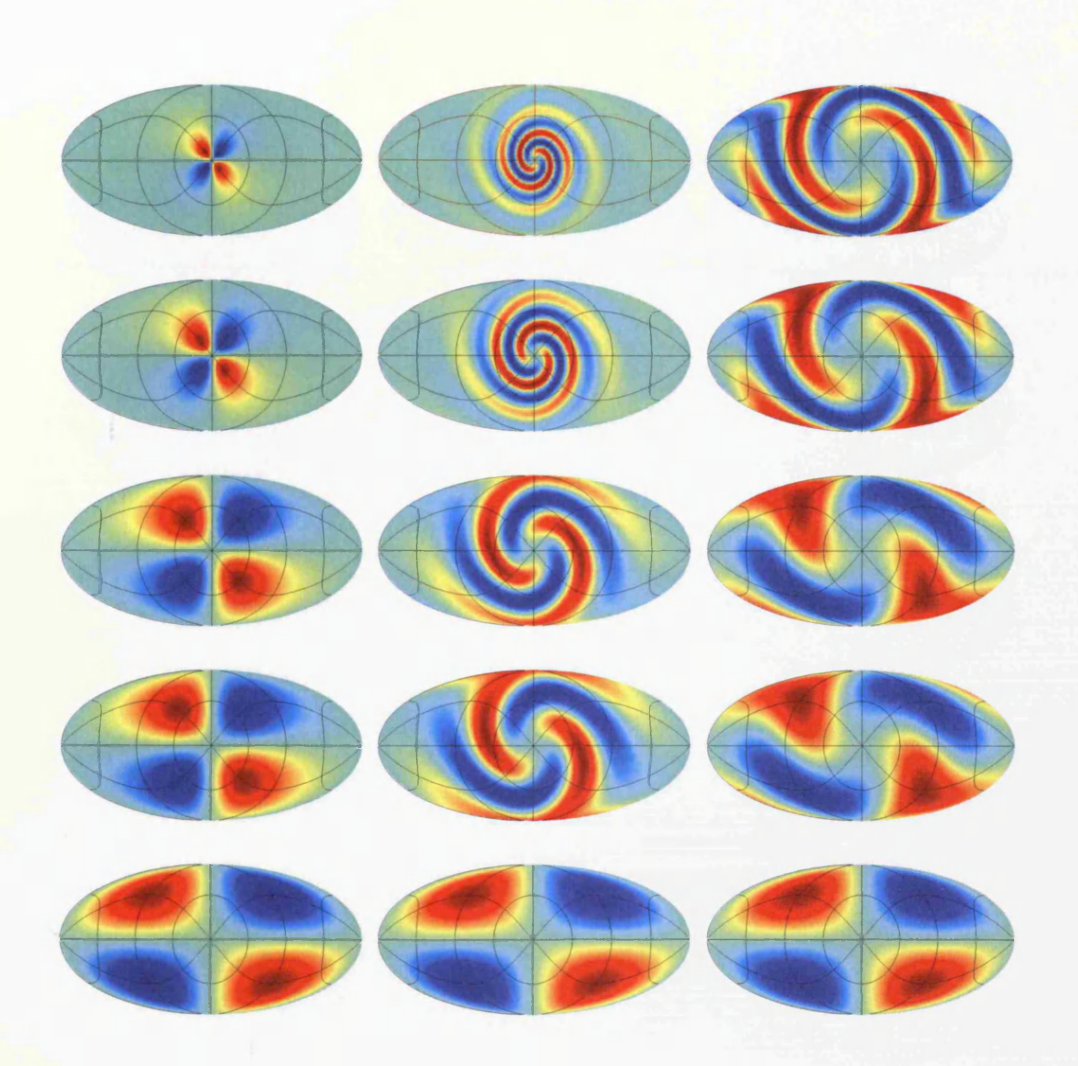


FIGURE 4.3: The time evolution of the temperature maps for Bianchi types V,  $VII_h$  and  $VII_0$ . Time increases from bottom to top. in Type V (left), the initial quadrupole retains its shape but gets focussed into a patch of decreasing size as time goes on. In Bianchi Type  $VII_0$  (right) the effect of rotation and shear is to twist the initial quadrupole into a spiral shape that winds up increasingly as the system evolves. In the middle case, Bianchi Type  $VII_h$  we have a combination of the two cases either side: there is both a focussing and a twist.

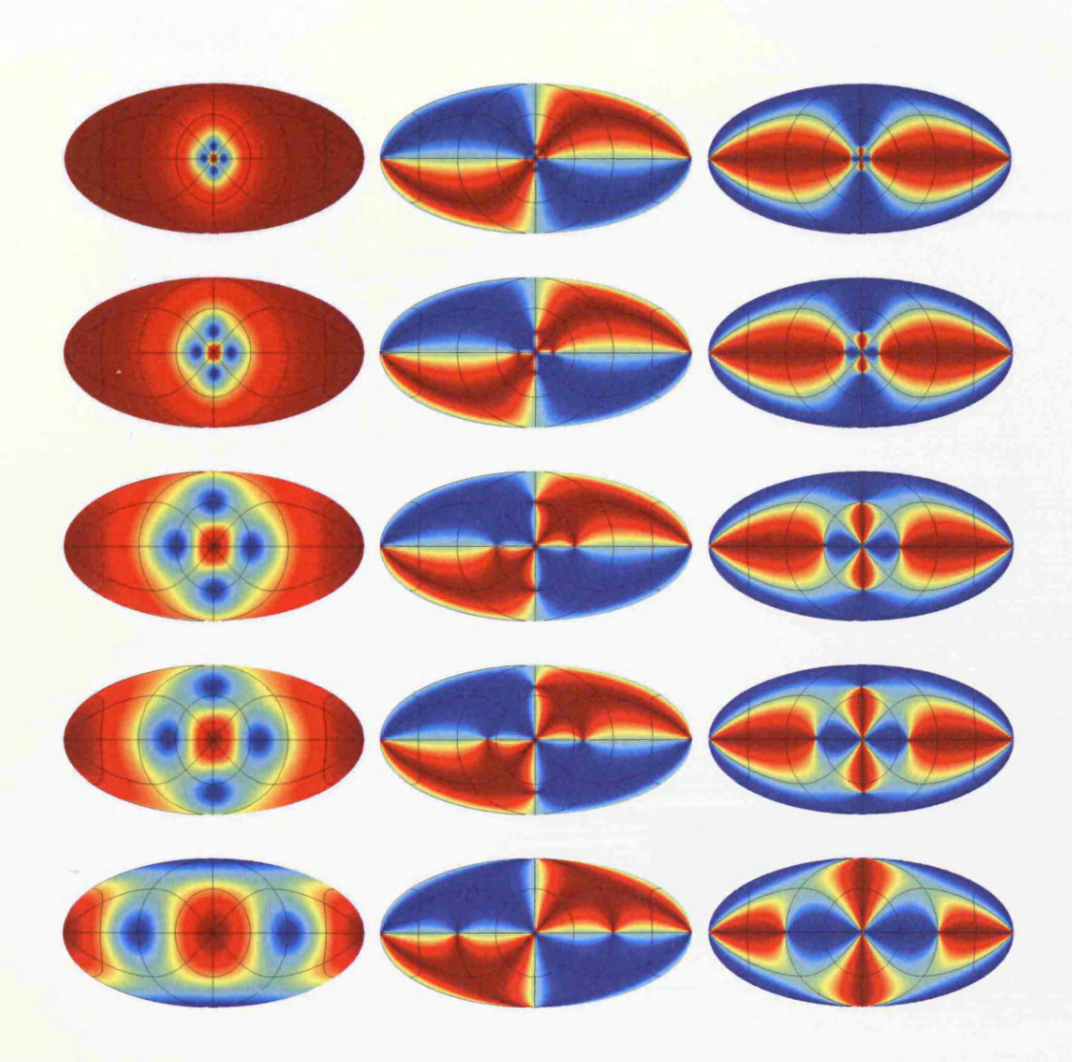


FIGURE 4.4: The time evolution of polarization maps for Bianchi V: degree of linear polarization (left); Stokes parameter Q (middle); and U(right). Time increases from bottom to top. While the polarization pattern alters with time in this case, its general orientation on the sky does not as is the case with the temperature pattern

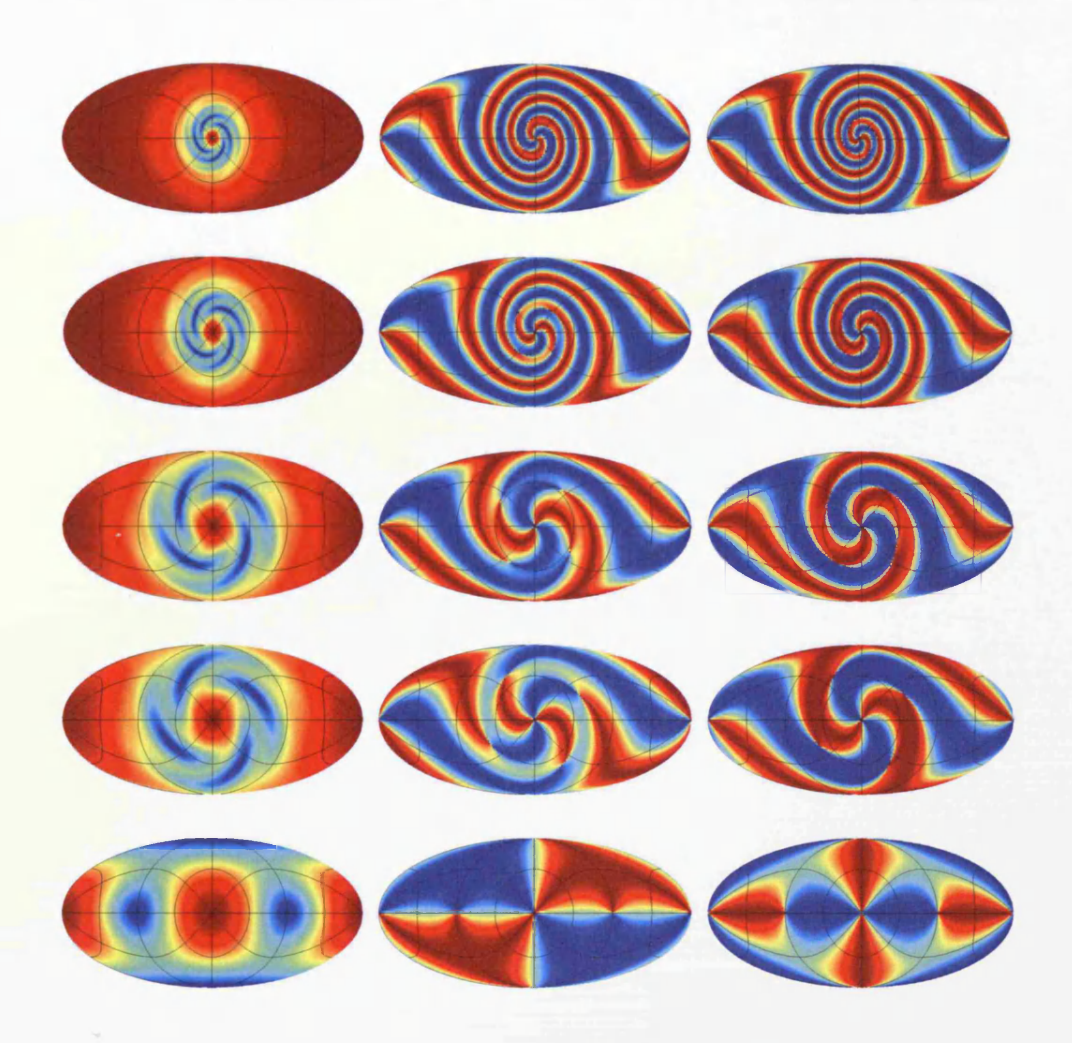


FIGURE 4.5: Same as Figure 4.4, but for Bianchi type  ${\rm VII}_h$ . The prodigious twisting of the polarized component of the radiation field, as well as a concentration of the degree of polarization. This case generically produces a large amount of mixing between Q and U during its time evolution.

case generically produces a large amount of mixing between Q and U during its time evolution.

Figure 4.6 shows, not unexpectedly, that Bianchi Type  $VII_0$  produces a similar interweaving of the Q and U configurations, but without the focussing effect in the total polarized fraction.

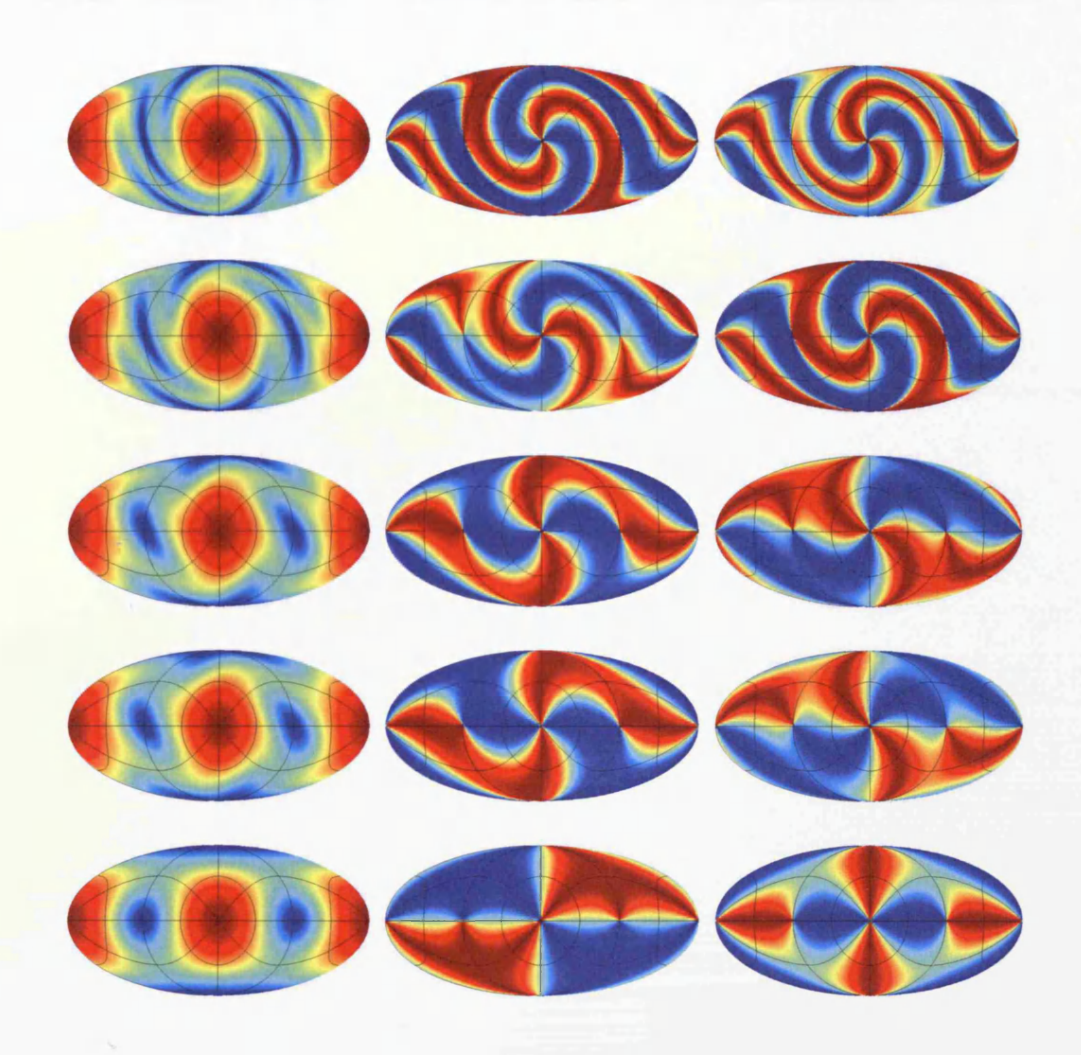


FIGURE 4.6: Same as Figure 4.4, but for Bianchi type  $VII_0$ . It produces a similar interweaving of the Q and U configurations, but without the focusing effect in the total polarized fraction.

Finally, for completeness we show results for Bianchi Type IX in Figure 4.7. This provides an interesting example of polarization behaviour because, in terms of polarization degree, the pattern does change at all with time but the Stokes maps Q and U do evolve. Bianchi Type IX models have positively curved spatial sections, and are equivalent in some sense to FRW models with the addition of circularly-polarized gravitational waves. These

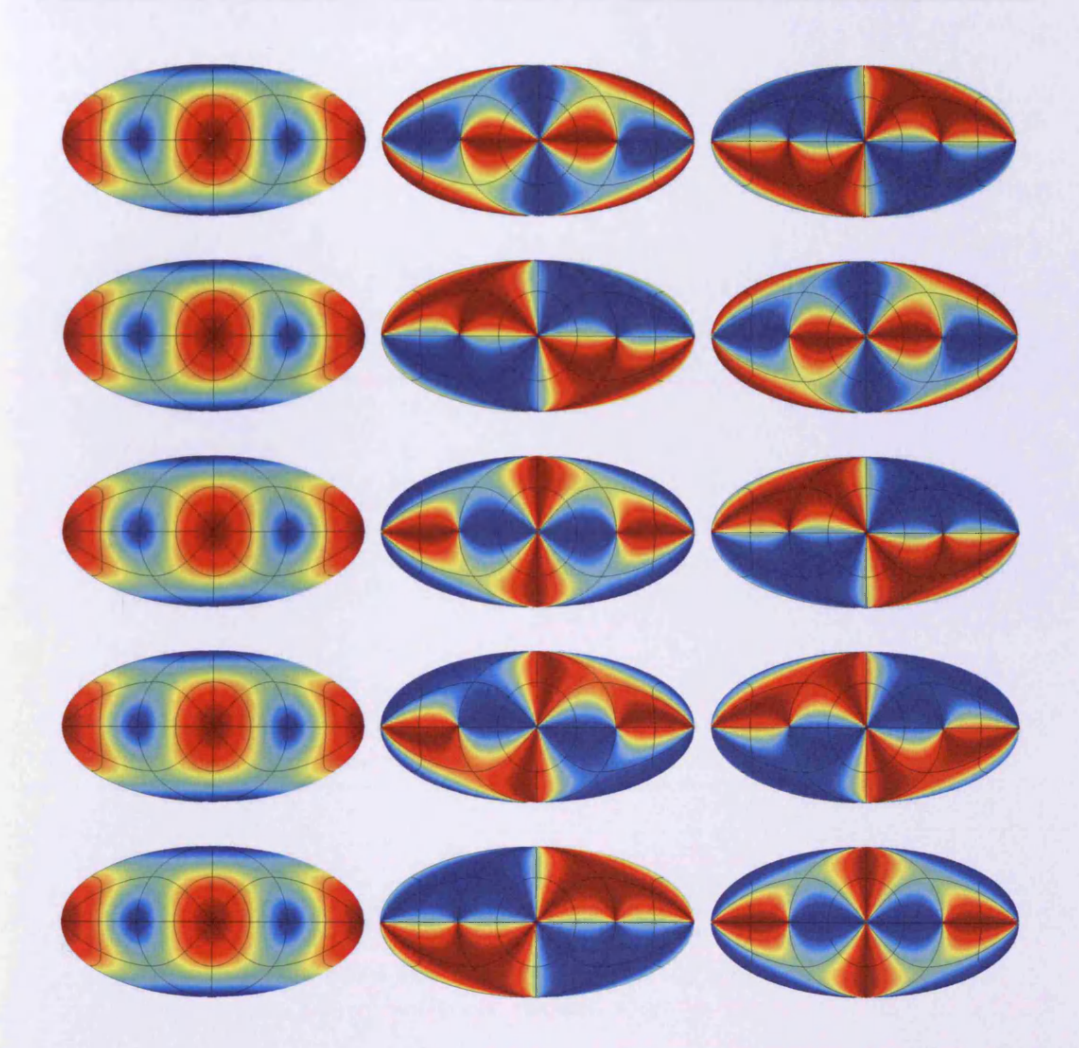


FIGURE 4.7: Same as Figure 4.4, but for Bianchi type IX. In terms of polarization degree, the pattern does change at all with time but the Stokes maps Q and U do evolve. The positive curvature does not allow for any focusing effects so the temperature pattern does not change with time either.

cause a rotation of the polarization angle but do not change the overall magnitude. The positive curvature does not allow for any focusing effects so the temperature pattern does not change with time either.

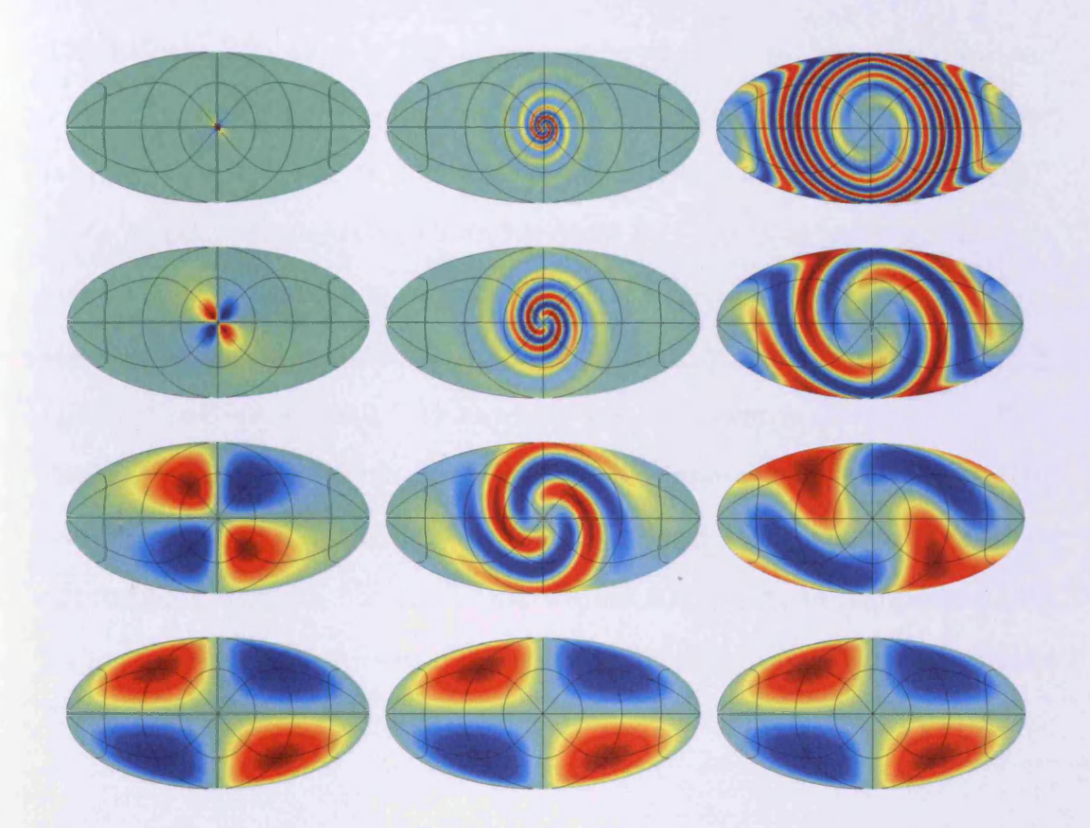


FIGURE 4.8: Temperature maps for Bianchi types V, VII<sub>h</sub> and VII<sub>0</sub> with different values of the density parameter,  $\Omega_0$ , which increases from top to bottom. It shows how  $\Omega_0$  affect the pattern on the maps for each of types we consider.

#### 4.2 Parameter Limits

The density parameter,  $\Omega_0$ , is an important parameter characterizing the universe model. Figure 4.8 shows how  $\Omega_0$  affect the pattern on the maps for each of types we consider. All Bianchi types have a very similar appearance to type I when  $\Omega_0$  approaches unity (bottom). On the other hand, lower values of the density parameter gives the focussed but decreased size of patterns for open models i.e. type V and VII<sub>h</sub>, and denser twisted one for VII<sub>0</sub>.

The Bianchi VII<sub>h</sub> type is parameterized by  $\Omega_0$ , and h. If we take various limits of them, we may obtain these subclasses i.e. I, V and VII<sub>0</sub> on some stage as shown in Figure 4.9. Let us begin with the image (left, middle), given density parameter is 0.3 and h equal 0.1, has been used through out this thesis as the sample of type VII<sub>h</sub>. As the h is increased (to top), the twisted effects become weaker and the type V appears which has only focussed pattern as limit. Meanwhile, for the lower h (to bottom), very dense spiral pattern turns up rather than focusing one. The type VII<sub>0</sub> can be obtained if x which is defined by h and  $\Omega_0$  in equation (2.12) is approaching infinite. For  $\Omega_0$  limits, Figure 4.8 is a good comparison. As  $\Omega_0$  is increased (to left) the images show the same tendencies like Figure 4.8.

#### 4.3 Bianchi Maps, Initial Dipole

Multipoles of different orders are both produced and correlated through terms arising in the Boltzmann equation. As we explained in some detail in Chapter 3, the dipoles of Bianchi type I, VII<sub>0</sub> and IX among of the models which we have studied are not generated by another multipoles. In order to investigate the possible effect of a dipole in the initial conditions, we explored the behaviour of the radiation fields produced by picking this as a free parameter. This is not particularly well motivated from a physical point of view, but does generate a more complex set of pattern morphologies and is therefore of interest from a phenomenological point of view.

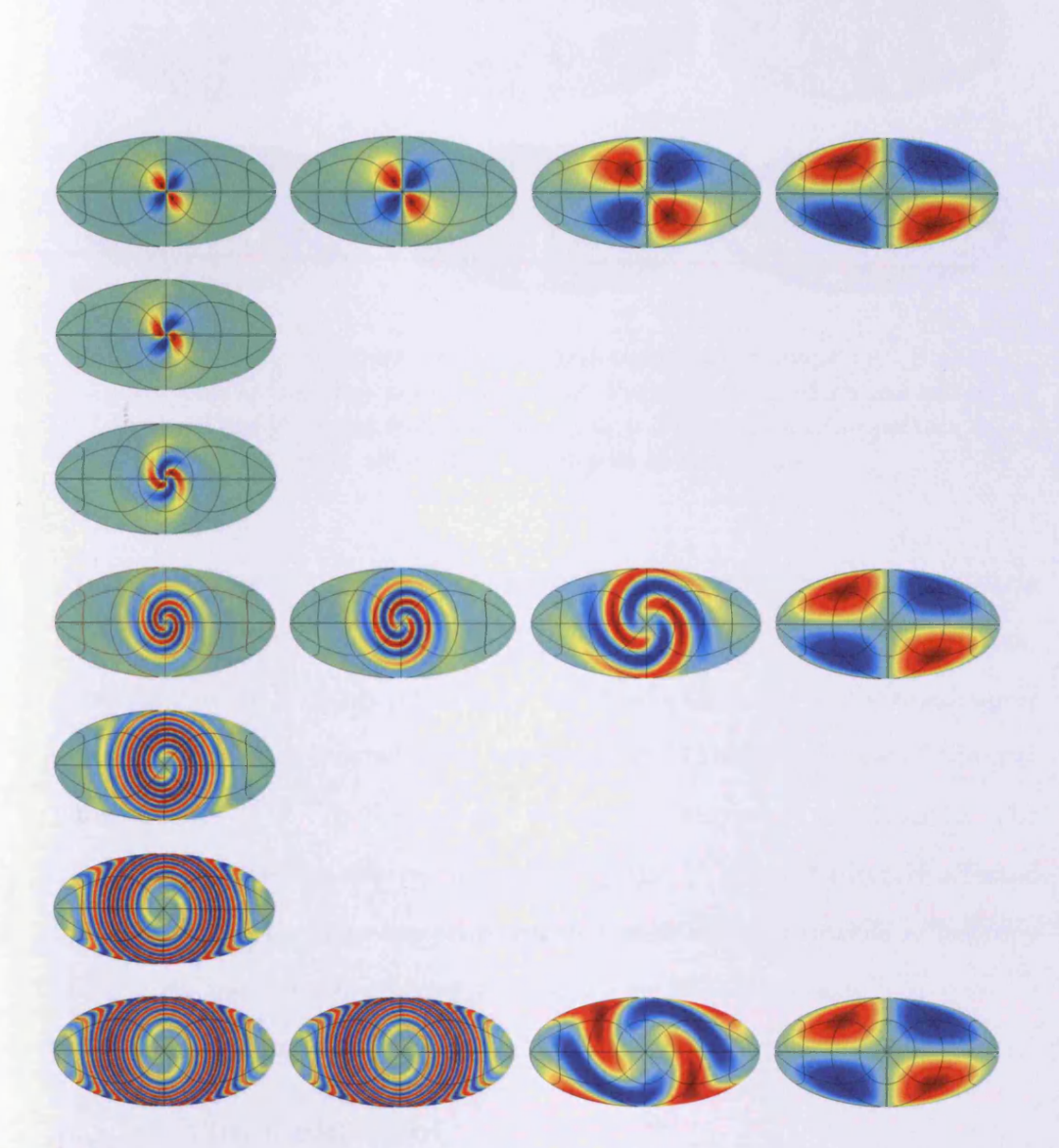


FIGURE 4.9: Temperature maps for Bianchi  ${\rm VII}_h$  type as parameters limits: h is decreased from top to bottom and  $\Omega_0$  is increased from left to right. If we take various limits of them, we obtain these subclasses i.e. I, V and  ${\rm VII}_0$  on some stage.

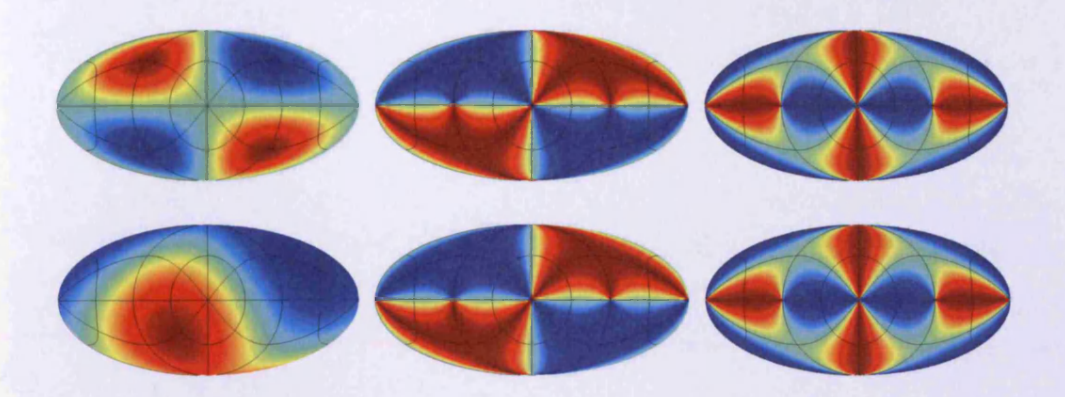


FIGURE 4.10: Temperature (left) and polarization maps i.e. Stokes parameter Q (middle) and U (right) of Bianchi type I which has initial dipole. Time increases from bottom to top. The temperature pattern is highly affected by the dipole at early time.

An initial dipole can affect the pattern considerably, especially at early times, even in the simplest case of Bianchi I type. At early time, the temperature pattern is highly affected by the dipole but later on the quadrupole overwhelms all patterns which is very similar to the type I case of the previous section. The dipole is merely about 0.1 percent of quadrupole. The polarization patterns, Stokes parameter Q and U, are not directly affected by the dipole since they are only coupled with the quadrupole anisotropy of the radiation intensity which is, effectively, the temperature.

#### 4.3.1 The Cold Spot

The quadrupole is affected hugely not only from the monopole but also the dipole, as we see the Figure 4.16. What happens in the quadrupole patterns is that one of cold regions is getting focussed into a smaller part of sky which look like the Cold Spot. On the other hand, the dipole forces

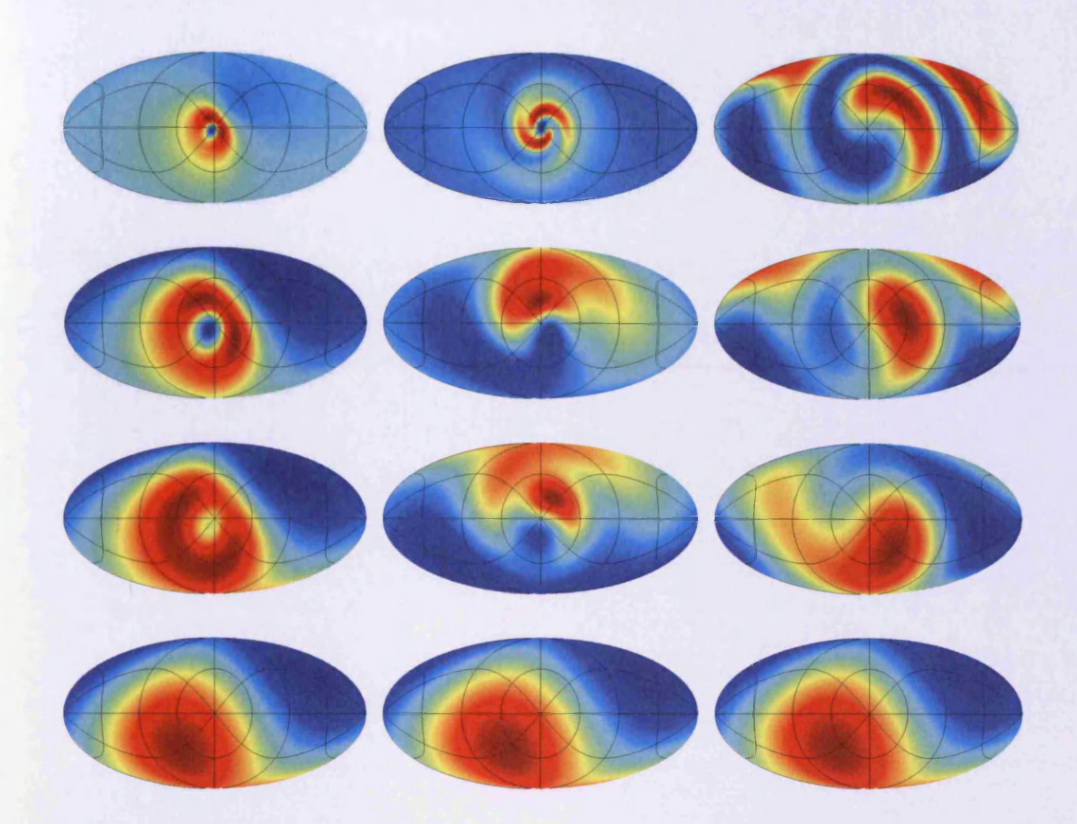


FIGURE 4.11: The time evolution of temperature maps from early stage (bottom) to late time (top) for Bianchi V (left),  $\mathrm{VII}_h$  (middle) and  $\mathrm{VII}_0$  (left). These models have a initial dipole.

a hot region to make a ring around a cold region. However, if the initial dipoles are tiny then it has very much same patterns like a what we have seen in previous section. The two following equations from the Boltzmann equation show how this happens:

$$\dot{N}_{i}^{0} + (\zeta \hat{A}_{i}^{k} + \hat{B}_{i}^{k}) N_{k}^{0} + \hat{C}_{i}^{kl} N_{kl}^{0} = -\tau (^{Re} N_{i}^{0} + \frac{2}{3} i^{Im} N_{i}^{0}) 
\dot{N}_{ij}^{0} + \zeta \hat{E}_{ij} N_{0}^{0} + \hat{H}_{ij}^{k} N_{k}^{0} + (\hat{F}_{ij}^{kl} \zeta + \hat{G}_{ij}^{kl}) N_{kl}^{0} = -\tau \left(\frac{4}{5} {}^{Re} N_{ij}^{0} + \frac{3}{10} {}^{Re} N_{ij}^{2} + i^{Im} N_{ij}^{0}\right)$$
(4.1)

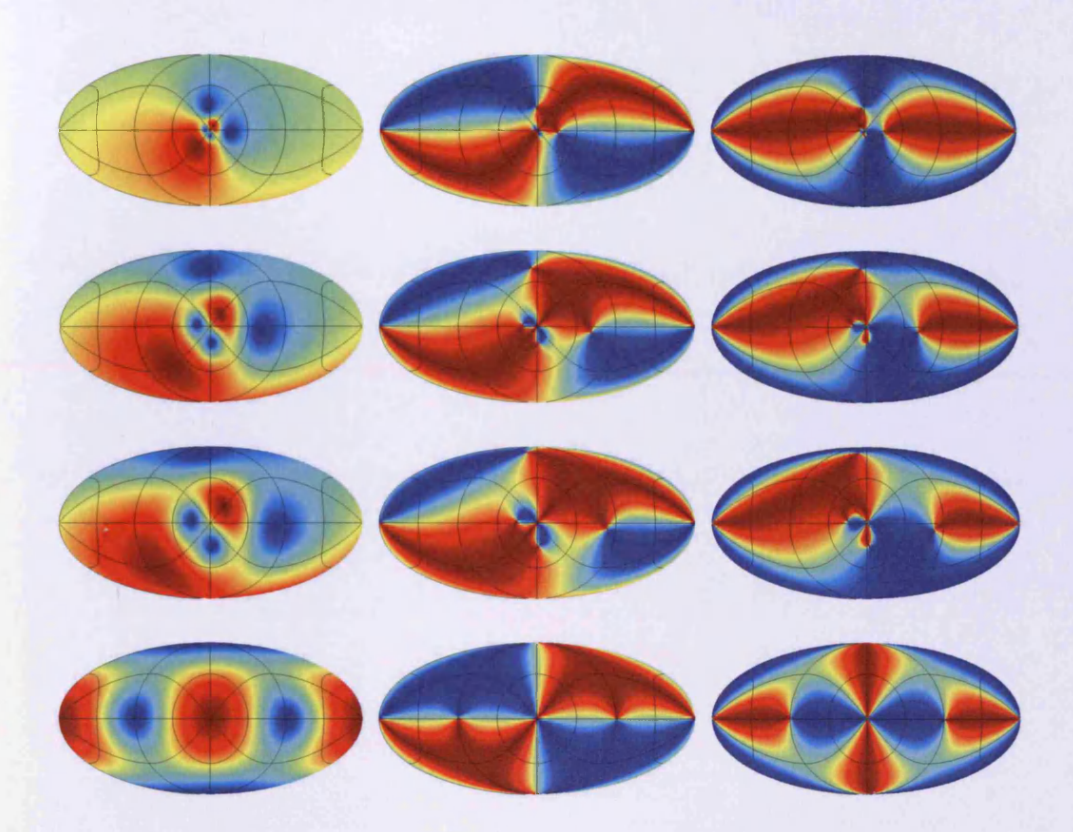


Figure 4.12: The time evolution polarization maps from early stage (bottom) to late time (top) for Bianchi V type: degree of polarization (right), Stokes parameter Q (middle) and U (left)

The dipole and quadrupole components are coupled by coefficients  $\hat{C}_i^{kl}$  and  $\hat{H}_{ij}^k$ , as given

$$\hat{C}_{i}^{kl} = \frac{2}{5} \left( \epsilon_{iks} n_{l}^{s} + \frac{1}{2} \epsilon_{kls} n_{i}^{s} - 3a_{k} \delta_{il} + a_{i} \delta_{kl} \right)$$

$$\hat{H}_{ij}^{k} = \frac{1}{2} \left( \epsilon_{ljk} n_{i}^{l} - \epsilon_{ilk} n_{j}^{l} + \epsilon_{ijl} n_{k}^{l} \right) + \left( \delta_{j}^{k} a_{i} - \delta_{j}^{i} a_{k} \right)$$

which are governed by the Bianchi vectors,  $a_i$  and  $n_j^i$ . The quadrupoles arise from the monopole through the shear term,  $\hat{E}_{ij} = \sigma_{ij}$ , and keep the same shape or symmetry of hot and cold tails as long as the influence of the dipole is very weak. However, once dipoles start to act on the quadrupole,

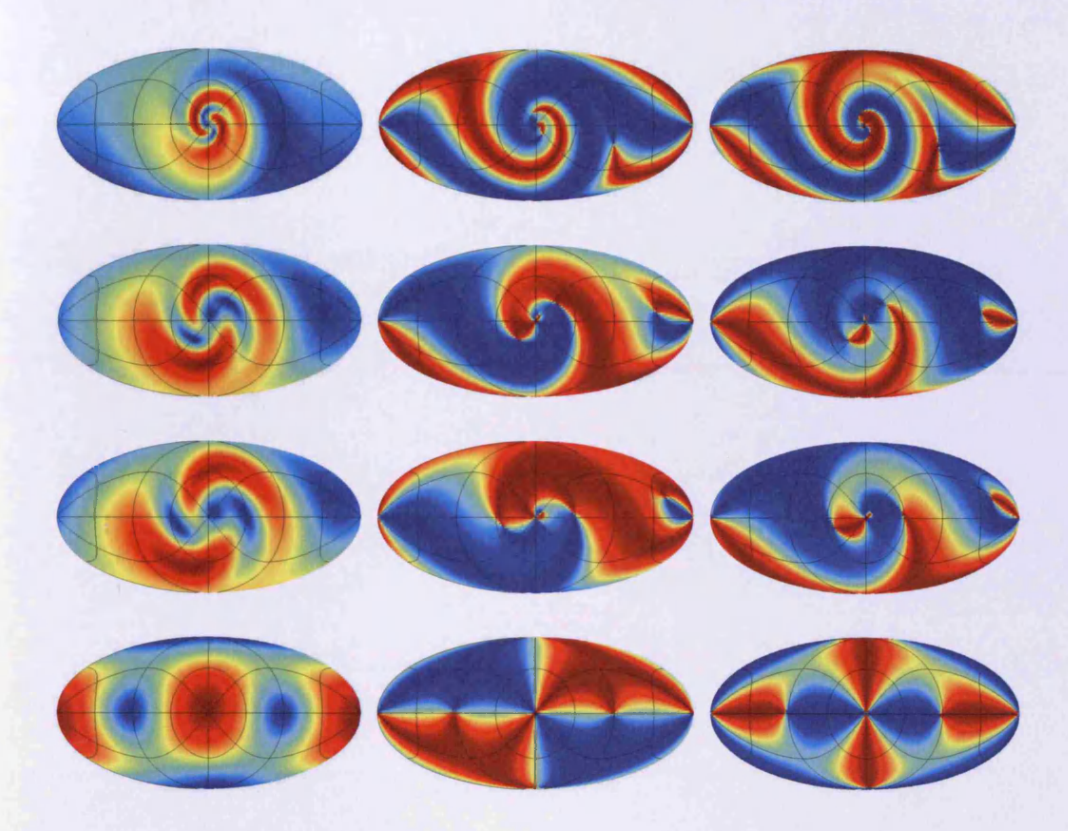


FIGURE 4.13: Time evolution polarization maps from early stage (bottom) to late time (top) for Bianchi  $VII_h$  type: degree of polarization (right), Stokes parameter Q (middle) and U (left)

it twists the patterns in different direction by coefficient  $\hat{H}_{ij}^k$ , making a strong cold spot and a hot ring.

#### 4.3.2 Implications for E and B Modes

It has become conventional to decompose the polarized component of the cosmic microwave background into modes classified according to their parity. The even modes are called E-modes and the odd modes are the B-modes. The latter are of particular interest in the context of inflationary cosmology as they cannot be sourced by scalar perturbations and are

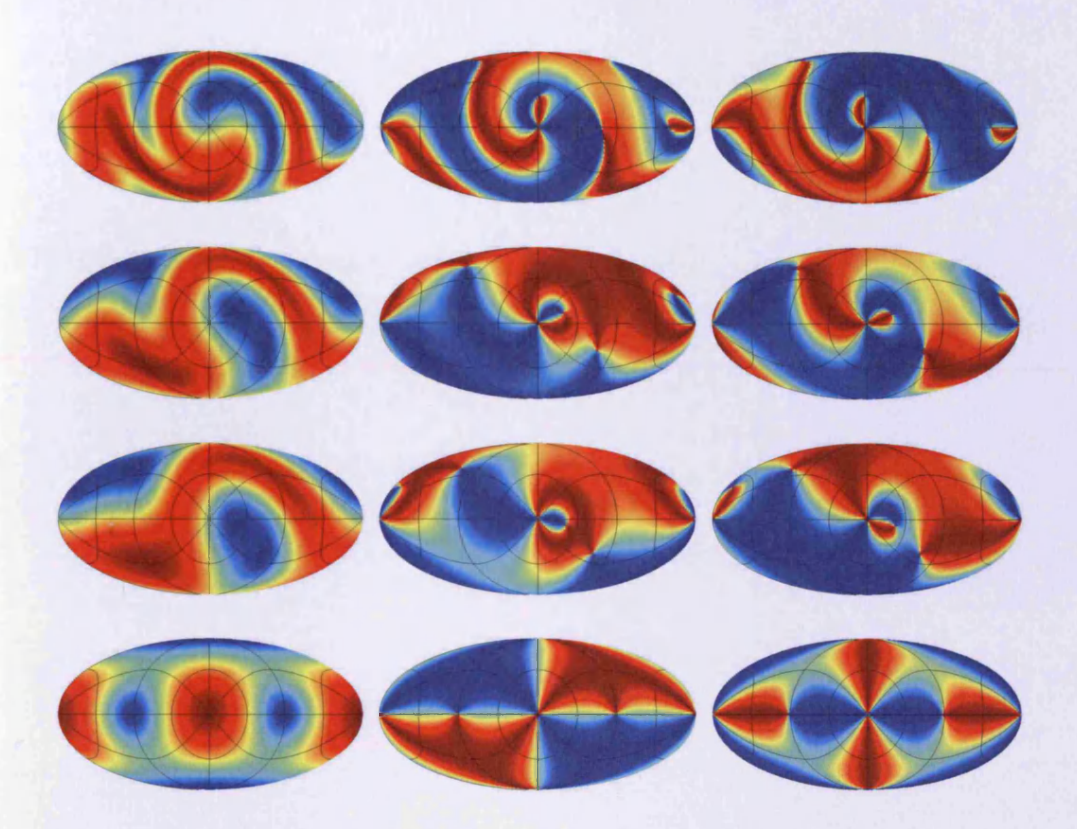


FIGURE 4.14: Time evolution polarization maps from early stage (bottom) to late time (top) for Bianchi VII<sub>0</sub> type: degree of polarization (right), Stokes parameter Q (middle) and U (left)

therefore generally supposed to be a signature of the presence of primordial tensor perturbations, i.e. gravitational waves [72, 73]

$$N^{2} \equiv N_{ij}^{2} m^{ij} = (Q - iU)(\hat{n}) = \sum_{lm} a_{-2,lm} {}_{-2}Y_{lm}(\hat{n}), \qquad (4.2)$$

$$\bar{N}^2 \equiv \overline{N_{ij}^2 m^{ij}} = (Q + iU)(\hat{n}) = \sum_{lm}^{lm} a_{2,lm} \,_{2}Y_{lm}(\hat{n})$$
 (4.3)

$$a_{E,lm} = -(a_{2,lm} + a_{-2,lm})/2, a_{B,lm} = i(a_{2,lm} - a_{-2,lm})/2 (4.4)$$

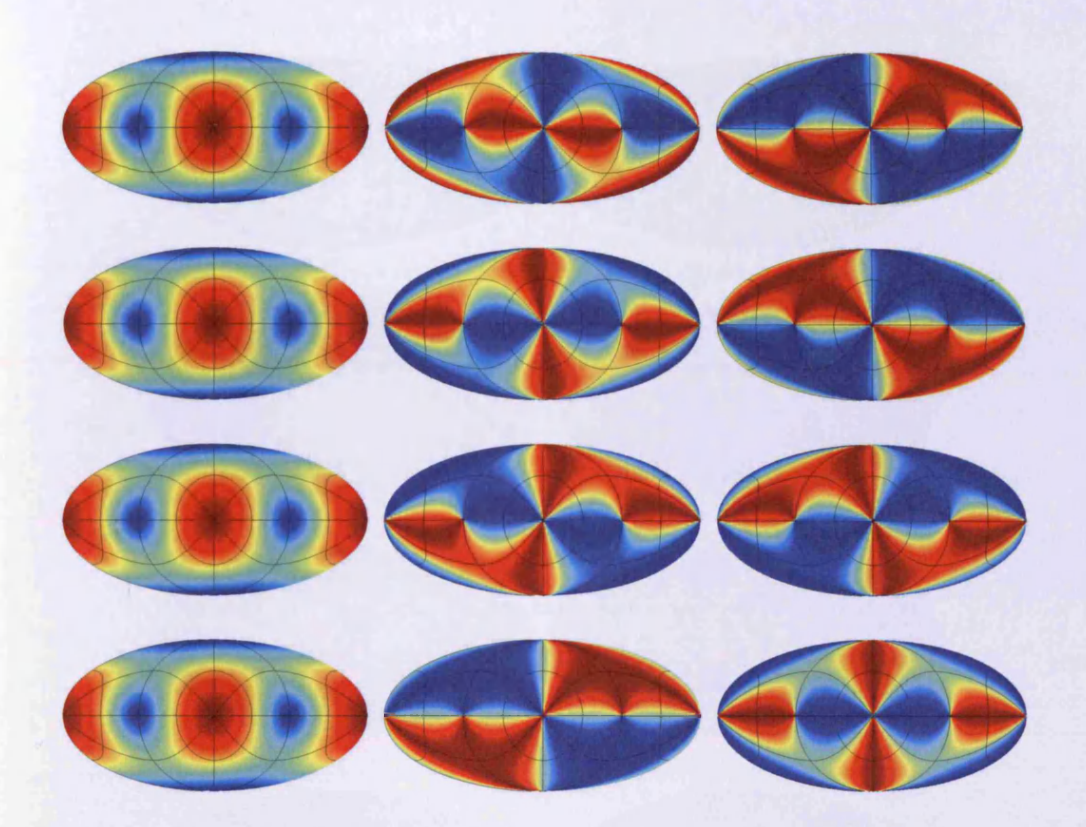


Figure 4.15: Time evolution polarization maps from early stage (bottom) to late time (top) for Bianchi IX type: degree of polarization (right), Stokes parameter Q (middle) and U (left)

The equations of the previous chapter for the evolution of the polarized radiation distribution allow us to establish some firm implications for the E and B modes just by considering their symmetry. It may not easy to understand from the Boltzmann equation how E and B modes evolve, however we obtain the results between the linear combinations of  $N_{ij}^2$  and E, B modes in B.1: The E-modes can be described by the real parts of  $N_{ij}^2$ , while linear combinations of the imaginary parts of  $N_{ij}^2$  represent B-modes. First, the scattering term  $J^A$  produces a pure E-mode quadrupole anisotropy. Here

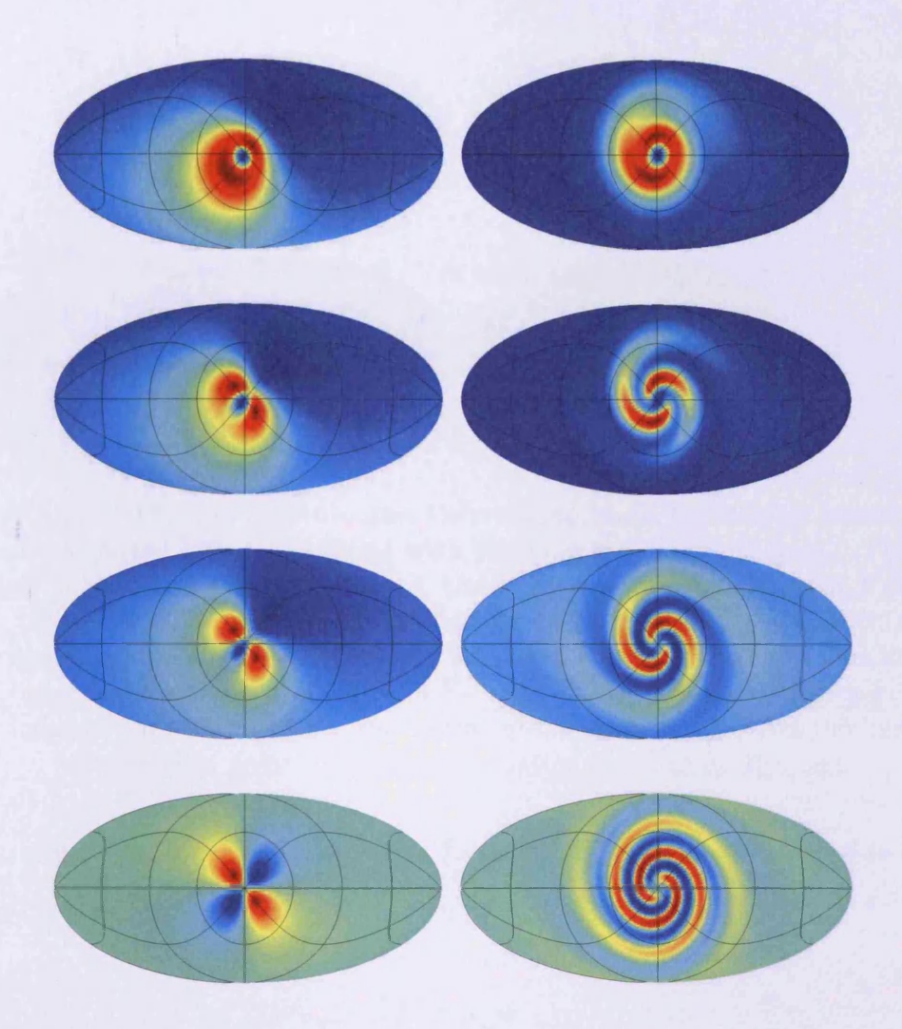


FIGURE 4.16: Quadrupole patterns for Bianchi V (left) and  ${\rm VII}_h$  (right) which show how they are affected by increased initial dipoles from pure quadrupole without initial dipole (bottom) to affected quadrupole which makes a cold spot and hot ring around it (top).

is again, polarization equation from the Boltzmann equation

$$\dot{N}_{ij}^2 + \zeta \hat{K}_{ij}^{kl} N_{kl}^2 + \hat{L}_{ij}^{kl} N_{kl}^2 + i \hat{M}_{ij}^{kl} N_{kl}^2 = -\tau \left( \frac{1}{5} {}^{Re} N_{ij}^0 + \frac{2}{5} {}^{Re} N_{ij}^2 + i {}^{Im} N_{ij}^2, \right) \tag{4.5}$$

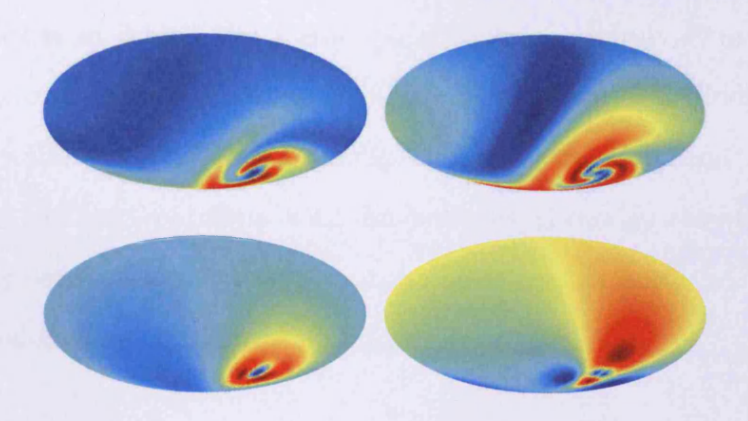


FIGURE 4.17: Temperature and Polarization maps for Bianchi models with localized features (aligned with the known CMB Cold Spot). The left panels show the temperature, the right the total polarization  $P = \sqrt{Q^2 + U^2}$ . The top row shows an example of Bianchi VII<sub>h</sub> with a compact spiral feature produced by focusing and twisting; the polarized component contains a significant B-mode. The bottom row shows a Bianchi V model in which the initial quadrupole is focussed but not twisted. The polarized field in the latter case has no B-mode.

with a coefficient  $\hat{M}_{ij}^{kl}$  which comes from  $d\psi/dt$ , time variation of twisted angle, is given

$$\hat{M}_{ij}^{kl} = \frac{1}{7} \left( \frac{11}{3} n_s^s \delta^{ik} - 4n_k^i \right) \delta^{jl}, \tag{4.6}$$

which swaps the real and imaginary of  $N_{ij}^2$  and thus corresponds to E and B mixing terms. However, depending on the initial conditions, the redshifting effect of shear can produce either E or B modes (just as a gravitational wave perturbation of FRW can). In general the E and B modes can be mixed there is twisting of the geodesics described by equation (4.5). In Bianchi VII<sub>h</sub> these effects are unavoidable so, even if there is no initial B-mode, one is inevitably generated as the Universe evolves. In Bianchi V, however, the coefficient  $\hat{M}_{ij}^{kl}$  term in equation (4.5) vanishes. Since initial conditions

therefore exist in which the initial polarization is purely E-mode, there are models of this type that can produce spots without B modes. Figure 4.17 shows illustrative fiducial examples of Bianchi VII<sub>h</sub> and Bianchi V that show localized patterns with an without B-modes respectively. A richer range of spot and pattern morphologies can be achieved with more complicated choices of the initial conditions [68].

#### 4.4 Conclusions

The goal of this work was to compute the temperature and polarization patterns produced in anisotropic relativistic cosmologies described by various Bianchi types. We focussed on those types that contain the standard homogeneous and isotropic FRW background as a limiting case. We integrated the equations for the radiation field numerically, and presented illustrative examples here.

We also have shown that it is possible, in a Bianchi V cosmological model, to generate a localized temperature anomaly quantitatively similar to the know Cold Spot without necessarily producing a large B mode polarization. Observational limits on the B mode alone are therefore not sufficient to exclude global anisotropy as a possible explanation of the famous Cold Spot. Although the set of Bianchi models that can evade the limits set by B mode polarization is small, a more rigorous analysis requires a fuller parametrization in which the Bianchi parameters are constrained with other cosmological parameters (such as the optical depth) using a complete description of the polarized radiation field. Note also that the overall level of

polarization depends strongly on the optical depth to Thomson scattering and, hence, on the ionization history. The polarization is produced coherently by a geometrical effect in Bianchi models and is typically therefore larger than in the perturbed FRW case for both E- and B-modes, with a total polarization of 10 per cent being possible.

# Chapter 5

# Statistical Characterization of Anisotropies

We showed in the previous chapter that localized features in the temperature pattern, qualitatively similar to the Cold Spot observed in the Wilkinson Microwave Anisotropy Probe (WMAP) data, can be generated in models with negative spatial curvature, i.e. Bianchi types V and VII<sub>h</sub>. However, we clearly need some way to characterize the non-Gaussianity and/or anisotropy present in the radiation field produced by these models if we are going to be able to make any progress towards understanding statistical features.

### 5.1 Pixel Distribution Histogram

We first investigate the characterization of the patterns produced by such models in terms of simple statistical descriptors of non-Gaussianity. These models do not possess stochastic perturbations but are inhomogeneous over the celestial sphere. Analysis of their temperature and polarization patterns using standard descriptors will consequently produce signals different from what one would see in the presence of stationary Gaussian noise. In this sense, all the Bianchi models are inherently non-Gaussian. We are investigating the behaviour of these models in order to find an optimal way to isolate the effect of anisotropy from that of non-Gaussianity. We introduce the method for testing statistical Gaussianity and apply it to the WMAP foreground reduced temperature map and also Bianchi type maps. We propose to test the statistical significance of this asymmetrical signal via following distributions. The Pixel Distribution Histogram (PDH) is simply a count of the pixel values. An important property of distribution histogram is that they tells us some clues of anisotropic features of map. The concept to understand this diagram is pretty much same like a Gaussian distribution that describes a data that cluster around a mean or average: The degree of concentration around the average temperature, which in this case is taken to be zero, tells us the homogeneity of the parameters on the maps. The perfect homogeneous map gives us delta function around a mean. On the other hand, we might read anisotropy from the asymmetry of distribution. We now explore the PDH for a number of examples.

#### 5.1.1 Applications

ILC maps. The WMAP Internal Linear Combination (ILC) method is a model-independent, self-contained method of estimating the pure CMB component from the foregrounds contaminated maps by a regional variance minimalization of the linear combination of one degree pre-smoothed multifrequency observations. Here we use maps obtained by a variation of this method, the Harmonic Internal Linear Combination (HILC) which involves using a harmonic ILC method which is an ILC in the pixel domain but with pixel-dependent weight [94]. The Figure 5.2 shows the Pixel Distribution Histogram (PDH) of temperature and Stokes parameters, Q and U. The y axis indicates for the normalized pixel numbers which is divided by total pixel number and x axis does also normalized by maximum of parameters e. temperature or Stokes parameters and so on. So this histogram represent how many pixels are obtained by each normalized temperature. As we see the Figure 5.2, the Q and U histograms are very focussed around the average since these are spread out over the sky rather uniform than the temperature pattern. So now one may ask where the Cold Spot can be seen on the histogram? As we already mentioned above, if there is anisotropy on the map, one can read it from asymmetry of histogram: one can see it on left wing of profile since it is 'cold' and size of it can be read by numbers of pixels on the y axis. From our simulations, however, it appears that it is difficult to detect a significant contribution from the Cold Spot owing to contamination of the map. These maps contain a mixture of emission from various astrophysical origin such as galactic and extragalactic foregrounds, as well as by instrumental noise. Moreover, subtracting such

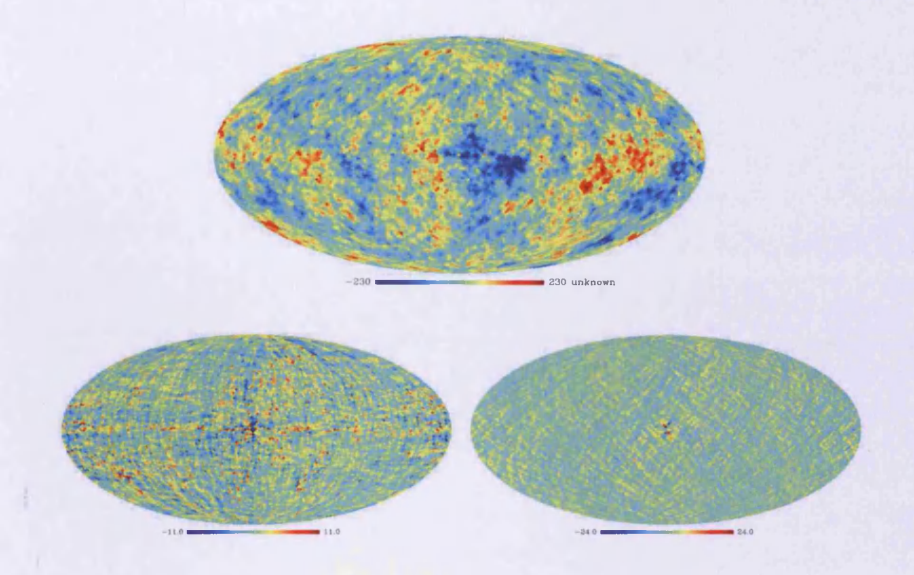


FIGURE 5.1: The Harmonic Internal Linear Combination (HILC5YR) temperature and polarization (Q and U) maps.

contaminations from the maps is not easy to do since the knowledge for individual sources is not sufficiently well known.

Bianchi maps. As we studied in previous chapters, Bianchi universes have their own characterized patterns that change significantly during time evolution. This tendencies also appear in the Pixel Distribution Histogram (PDH) as different shapes. We shall categorize those models as two groups: The Bianchi V and VII<sub>h</sub> types which have a focussed patterns are belonging to group A. Meanwhile, the group B contains Bianchi VII<sub>0</sub> and IX which have a rotation although these rotations come from different forms of angles,  $\phi$  and  $\psi$ . Let us begin with simplest type, Bianchi I. As we see in the Figure 5.3 the temperature pattern is evenly spread on the map although somewhat more distributed around the average. The profiles of Stokes parameters Q and U, both have symmetry from the mean, however, there

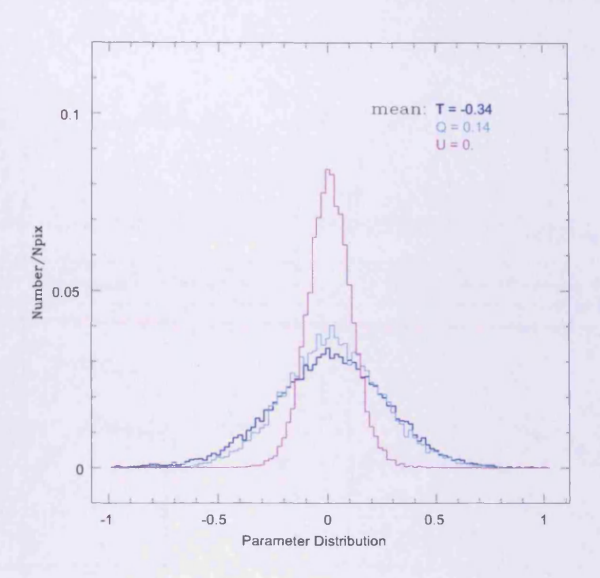


FIGURE 5.2: The Pixel Distribution Histogram (PDH) of Stokes parameters for the HILC maps. The y axis indicates the normalized pixel numbers which is the number of pixels at each given temperate divided by the total number of pixels. The Normalized Parameter along the y axis is whole range of parameters covered by the plot, but normalized so they can be plotted on the same axes.

is discrete; The histogram U has maximum peak on the mean value but Q has two maximum peaks from away from the mean. The patterns of Bianchi type I (and also type IX) do not change with time, but other types of models, i.e. group A, have their own characterized patterns during time evolution in the Figure 5.4. In the early stages, their patterns are almost identical such as Bianchi I. As temperature patterns are gradually move to prefer direction and focussed, temperature distribution of rest of area far from the spot become even. The distributions of histogram are also changed such that number of pixels around the average start to increase. Although the models in group A display similar feature, type V shows stronger inclination than  $VII_h$  type. The members of group B such as Bianchi  $VII_0$  have

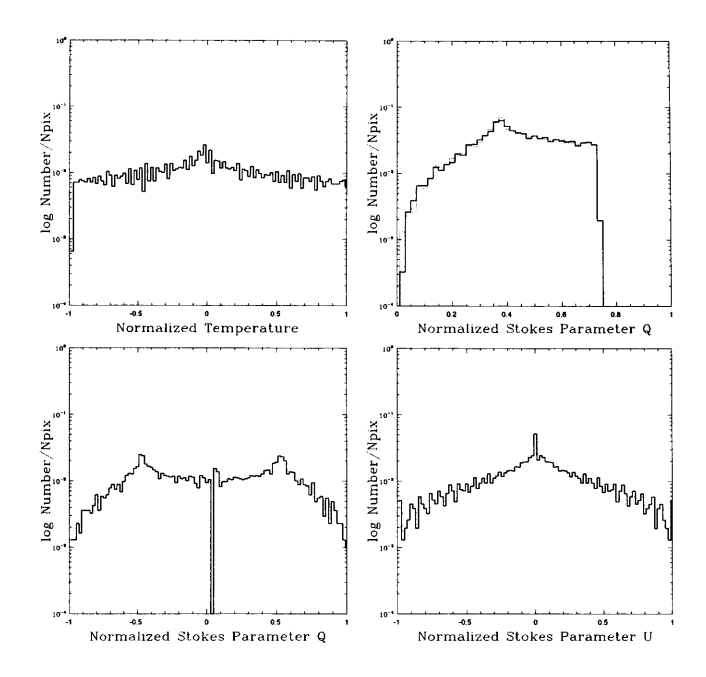


Figure 5.3: The PDH of temperature pattern (top) and polarization maps i.e. polarization amplitude (lower, left), Stokes parameter Q (lower, middle) and U (lower, right) of Bianchi type I.

rotation without focussing and provide a good comparison to explain how focussing pattern affects the pixel distribution. The profiles of histogram are merely changed as time goes on. Moreover, it almost has the same pattern as Bianchi I type, which means that rotation, Bianchi VII $_0$  type has, does not affect the histogram. Since the type IX has exactly same pattern like type I, all types in group B have same patterns like Bianchi I in spite of rotation. We also simulate for polarization of each groups and find out each group has similarity as we expected. The late-time shape of polarization amplitude in group A is steeper than early stages which are almost the same as type I. Bianchi type V obtain stronger tendency similar to temperature histogram. The profiles of Stokes parameter Q and U pose flatter inclination than early time. The profiles of polarization amplitude in group B are identical with Bianchi type I. The shapes of Stokes parameter

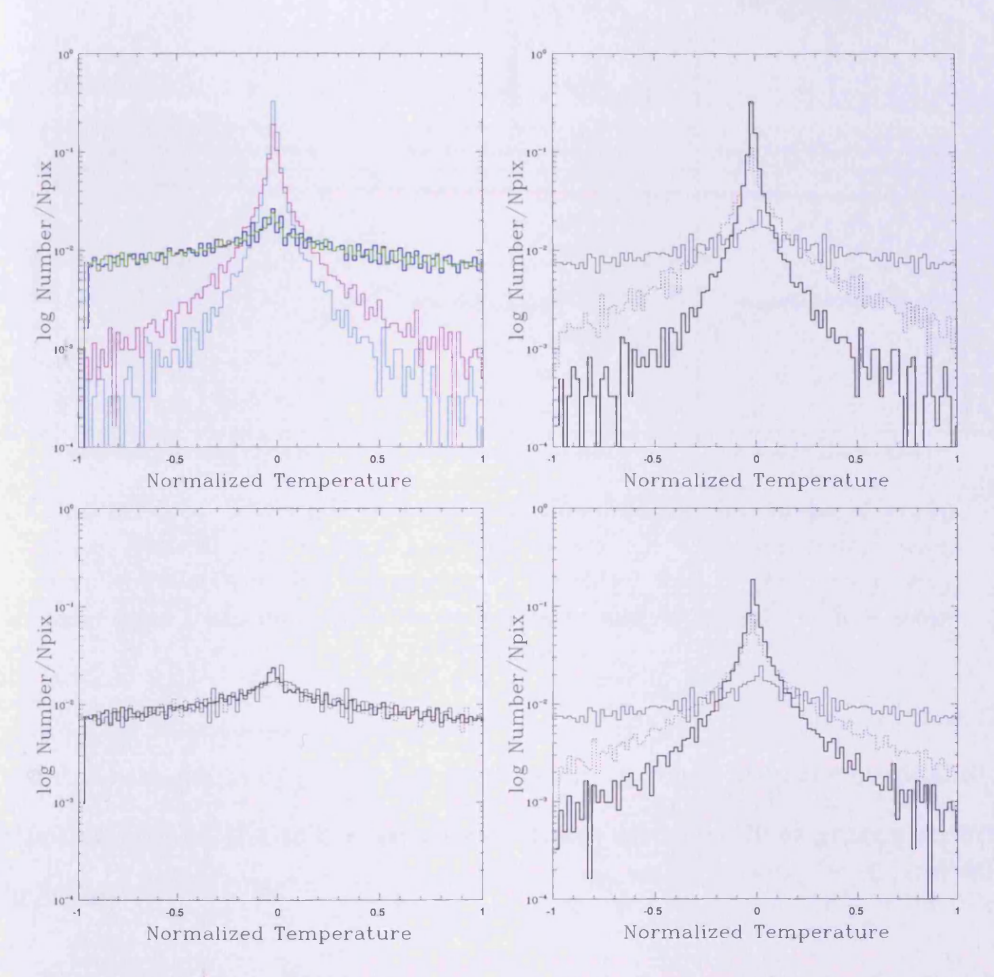


FIGURE 5.4: The PDH of the normalized temperature for the Bianchi maps; 1.Comparison between the models at late time (left, top) represented by different colours as cyan for type V, as magenta for type VII $_h$ , as green for type VII $_0$  and as blue for type I. 2. The time evolution PDH from very early time (thin line), time between early and late (dot) to late stage (thick line) for models i.e. Bianchi V (top), VII $_h$  (lower,right) and VII $_0$ (lower,left) types.

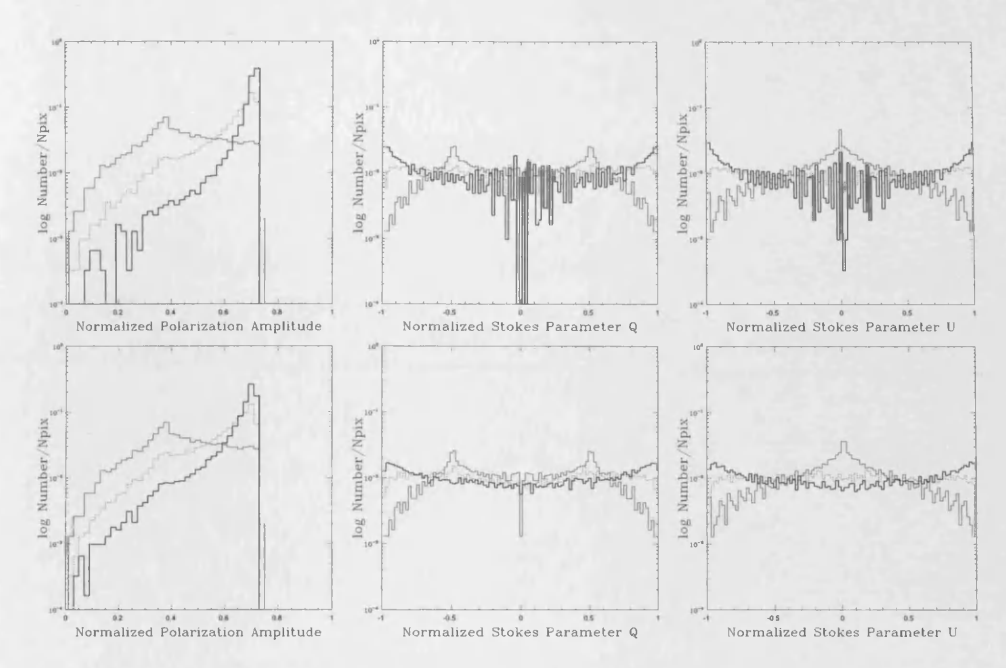


FIGURE 5.5: The PDH of time evolution Polarization maps of group A i.e. Bianchi type V (top) and  ${\rm VII}_h$  (bottom): The total polarization amplitude(left), stokes parameter Q (middle) and U (left) from very early time (thin line), time between early and late (dot) to late stage (thick line)

distributions also very similar far from group A: They keep the original distribution around the tails even though there are some fluctuations around the mean.

Bianchi types with initial dipole. The profiles of the PDH in these cases are not symmetric since those cases highly affected by dipole. As we see in Figure 5.7, type I has an extremely flat shape and group A has an excess of pixels in cold regions. We studied open models such type V and VII<sub>h</sub> as possible explanation of the Cold Spot in Chapter 4. There are some tests how total density parameter,  $\Omega_0$  affects to PDH in this chapter. Under the lower density parameter, histograms are roughly symmetric for each

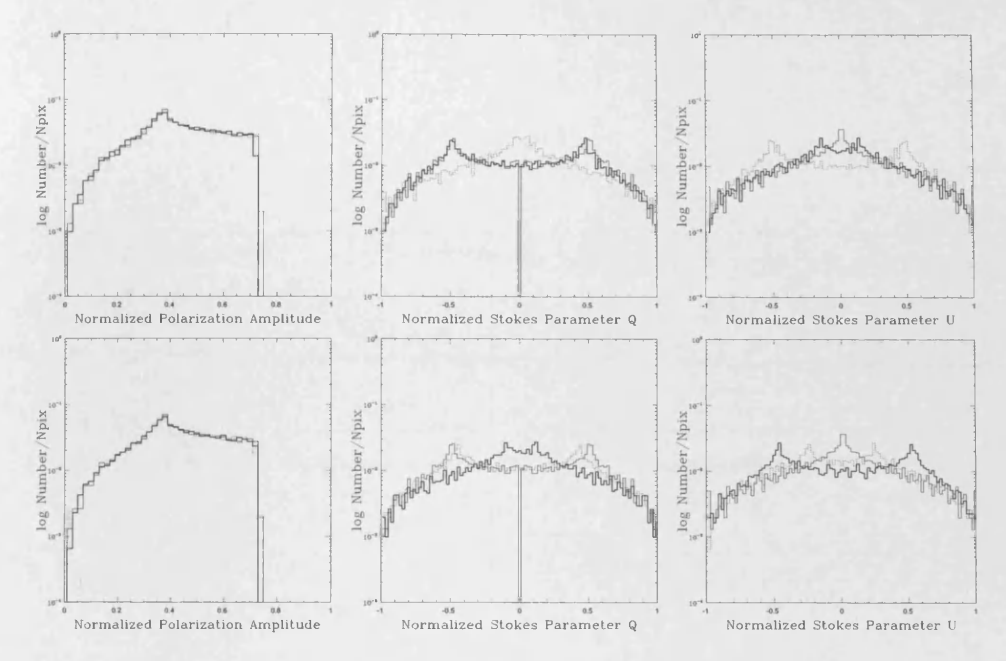


Figure 5.6: Same as Figure 5.5, but with group B i.e. Bianchi type  $\rm VII_0$  (top) and IX (bottom).

dipole and quadrupole. A higher density parameter breaks the symmetry around the mean and makes the profiles uneven: The dipole patterns obtain more pixels in the hotter area, however, the quadrupole case has more pixels in colder regions. On the other hand, higher density parameter does not break the symmetry of the histogram of Stokes parameters Q and U but makes it flatter (see Figure 5.8 and Figure 5.9).

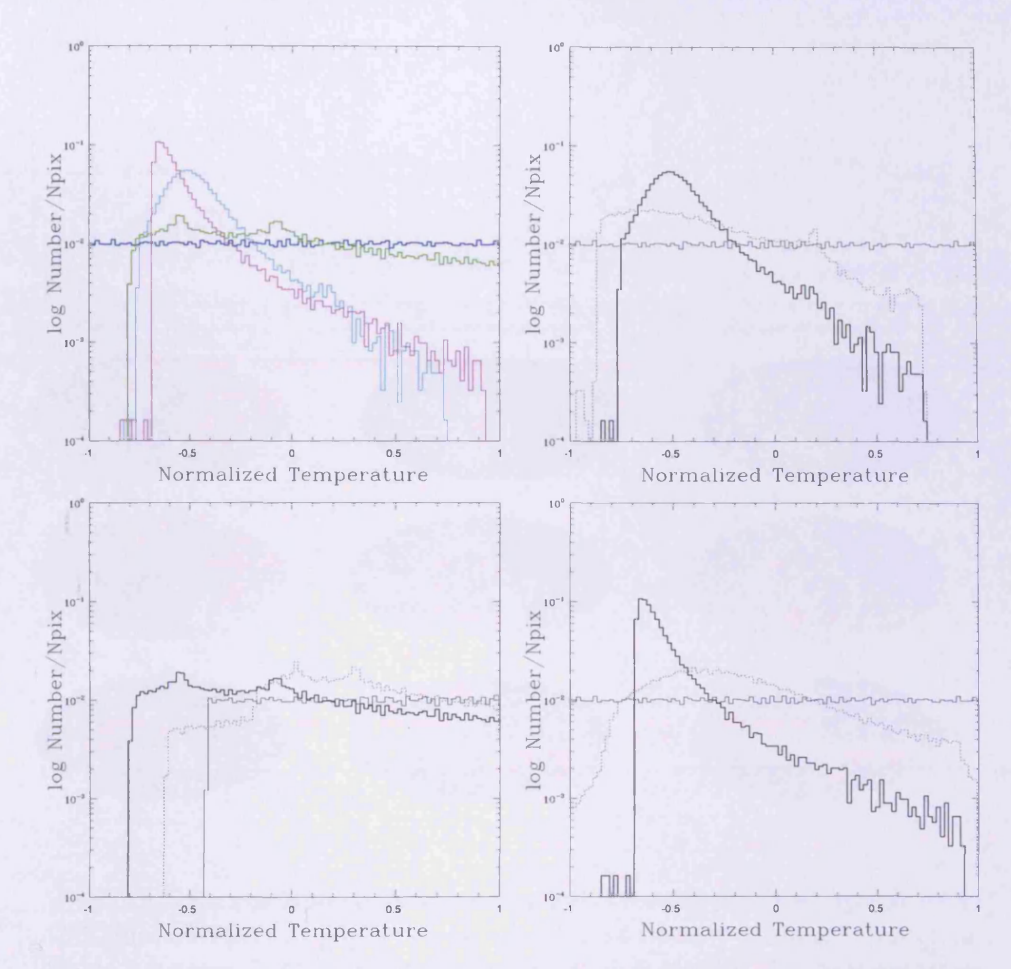


FIGURE 5.7: Same as Figure 5.4, but for Bianchi types which have initial dipole.

### 5.2 Multipole Vectors from Bianchi Universe

#### 5.2.1 Method

The WMAP data show anomalies at large angular scales. The planar extreme of the octopole, alignment of octopole and quadrupole and correlations of quadrupole and octopole with the Ecliptic Plane defined by the solar system as we explained in Chapter 2. Spherical harmonics have proved

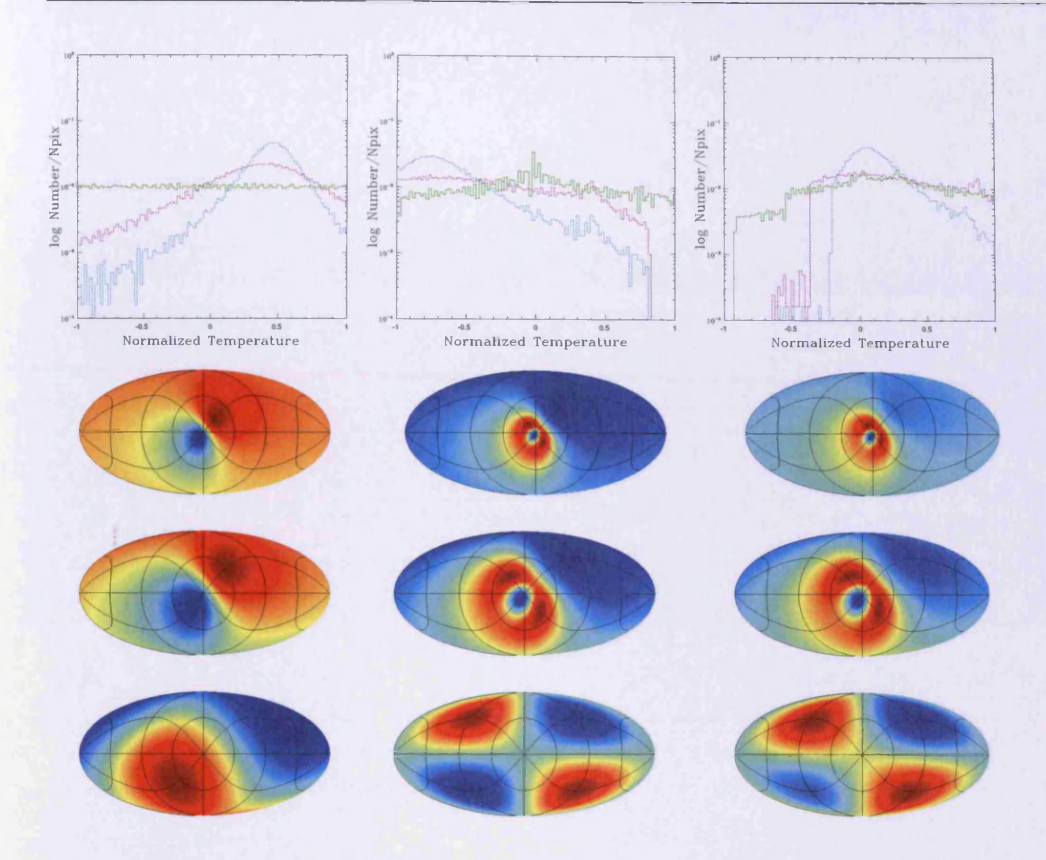


FIGURE 5.8: For Bianchi V type, the PDH for dipole (left), quadrupole (middle) and overall (right) maps as different density parameters such as  $\Omega_0=0.3$  (green),  $\Omega_0=0.6$  (magenta),  $\Omega_0=1$  (cyan). The temperature patterns also are simulated for multipoles as rely on density parameters such as  $\Omega=0.3$  (second row),  $\Omega_0=0.6$  (third row),  $\Omega_0=1$  (fourth row).

a popular tool to analyze the CMB data, yet a generally effective way of identifying correlations between them in CMB maps is yet to emerge that can verify such properties as the reported CMB anomalies. So in an effort to use the spherical harmonics to provide a more meaningful explanation of non-Gaussianities found, multipole vectors are now considered. The multipole vector was first introduced over one century ago [95] and there has been attempts to understand the multipole vectors in order to explain the CMB anomalies at large angular scale [29, 30, 32, 33, 38, 39]. However,

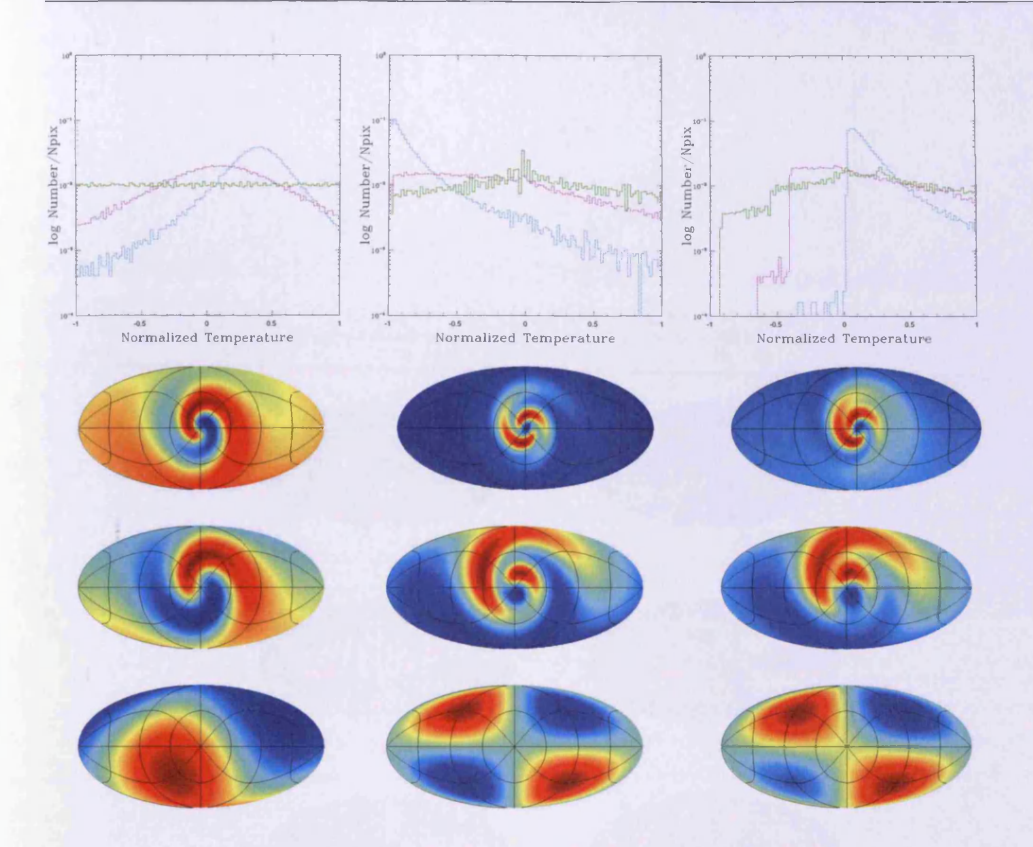


FIGURE 5.9: Same as Figure 5.8 but for Bianchi  $VII_h$  type.

for this study, we follow the rigorous formalism based on the mathematical background of concept from a polynomial point of view in [31].

We start by summarizing the background terminology. Every homogeneous polynomial  $F_R$  which has degree l in x, y and z can be written in the form

$$F_R(x, y, z) = \lambda \cdot (a_1 x + b_1 y + c_1 z) \cdot (a_2 x + b_2 y + c_2 z) \cdot \dots \cdot (a_l x + b_l y + c_l z) + S_R \cdot G_R.$$
(5.1)

The  $G_R$  is homogeneous polynomial of degree l-2 and  $S_R$  is given by  $x^2 + y^2 + z^2$ . Moreover, the polynomials,  $F_R$ ,  $G_R$ ,  $S_R$  and all variables are in real (i.e. pixel) space. Unlike the equation (10) in [30], this theorem satisfies

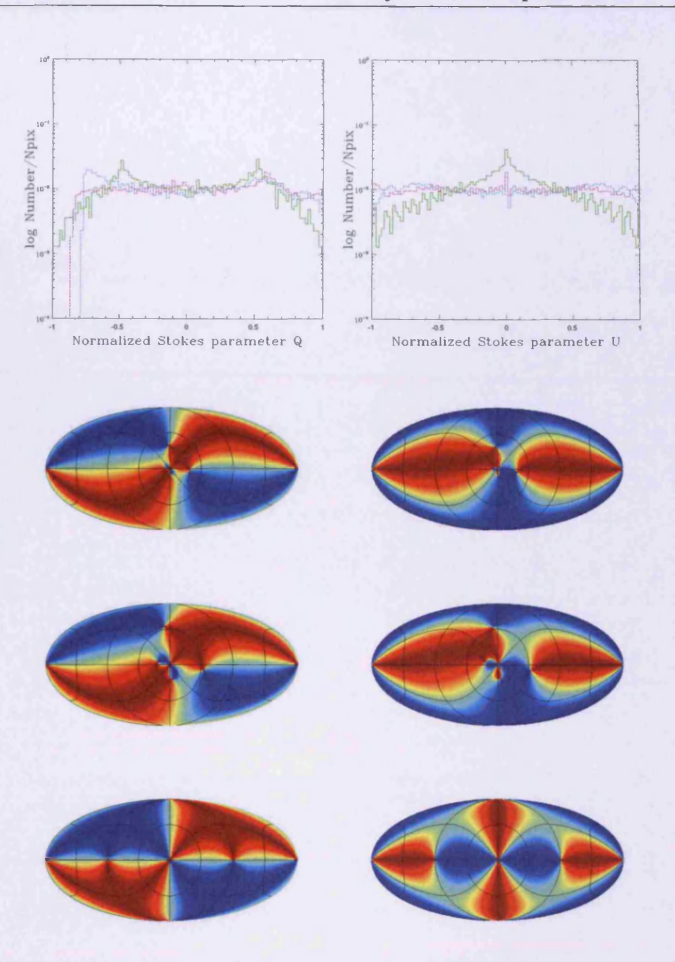


FIGURE 5.10: Normalized Stokes parameters, Q (top, left) and U (top, right), the PDH for Bianchi V type as different density parameters such as  $\Omega=0.3$  (magenta),  $\Omega=0.6$  (green),  $\Omega=1$  (cyan). These patterns also are simulated as relying on density parameters such as  $\Omega=0.3$  (second row),  $\Omega=0.6$  (third row),  $\Omega=1$  (fourth row).

in general and the polynomial  $F_R$  does not necessary have to be either homogeneous or harmonics. If we consider the value of the polynomial on the unit sphere the quadratic term  $S_R = 1$  gives so the  $F_R$  is expressed by the product of linear parts with  $G_R$  term.

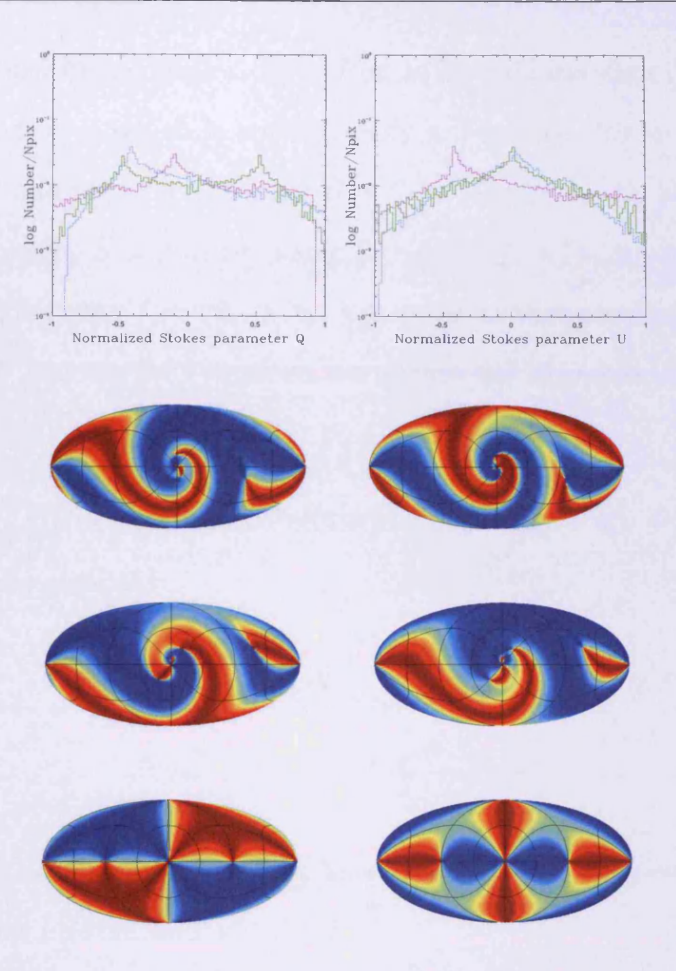


FIGURE 5.11: Same as Figure 5.10, but for Bianchi type  $VII_h$ 

The polynomial may be extended to complex polynomial F i.e.

$$F(x, y, z) = \lambda \cdot L_1 \cdot L_2 \cdots L_l + S \cdot G \tag{5.2}$$

The x, y and z are complex numbers although the coefficients of F are real. We are also interested in the value of the polynomial on the unit sphere, however, in this situation, complex space, the quadratic curve  $S = x^2 + y^2 + z^2$  is not identically 1 but 0. By Bézout's theorem, which asserts that the number of points of two curves is equal to the product of their degree, there

are 2l points in which complex curve F(x,y,z)=0 intersects the quadratic curve S(x,y,z)=0 which is topologically a 2-sphere. Since the complex curve F=0 intersect the complex S=0 in 2l points, the product curve of  $L_i$  also intersect S=0 in the same 2l points,  $f_i=(x_i,y_i,z_i)$ . Moreover, its complex conjugate  $\bar{f}_i=(\bar{x}_i,\bar{y}_i,\bar{z}_i)$  has to lie in the intersection in which both F and S become 0. Therefore, we obtain the 2l points of intersection such as  $\{f_1,\bar{f}_1,\cdots,f_l,\bar{f}_l\}$ .

Each pair  $\{f_l, \bar{f}_l\}$  determines a unique line  $L_i = a_i x + b_i y + c_i z = 0$  with real coefficients such as

$$a_{i}x_{i}^{Re} + b_{i}y_{i}^{Re} + c_{i}z_{i}^{Re} = 0$$

$$a_{i}x_{i}^{Im} + b_{i}y_{i}^{Im} + c_{i}z_{i}^{Im} = 0$$
(5.3)

with coefficients normalized to unit length, i.e.  $a_i^2 + b_i^2 + c_i^2 = 1$ . Note that the i index has no sum and  $1 \le i \le l$ .

In order to find the multipole vectors,  $v_i^l = (a_i, b_i, c_i)$  of each l, we need to find out the pair of  $f_i$  which lie on the curve F = 0 and S = 0 in the complex projective plane. i.e. finding the roots which satisfy F = 0 on the 2-sphere (S=0). what requires is to factorize a homogenous, harmonic polynomial, F into linear factors such as product of  $L_i$ . However, this is not possible from analytic considerations since they are not linear equations far from the dipole. Fortunately, the curve S = 0 can be parameterized as single variable and polynomial F also can be described in terms of reduced variables:

$$F(x, y, z) = F(i(\alpha^2 - 1), -2i\alpha, \alpha^2 + 1).$$
 (5.4)

From equation (5.4), first of all, find the roots  $\alpha$  which satisfy F = 0 and S = 0 or the product of  $L_i = 0$ . Once we find the roots of  $\alpha$ , the pair of  $\{f_i, \bar{f}_i\}$  can be expressed as x, y and z. The next step involves finding the multipole vectors from equation (5.3) using  $f_i = (x^{Re}, y^{Re}, z^{Re}) + i(x^{Im}, y^{Im}, z^{Im})$  or its conjugate  $\bar{f}_i$  since two points give same result.

Let us now apply this terminology to cosmological application, temperature patterns on the CMB sky. The  $l^{th}$  multipoles,  $T_l$ , also can be represented by polynomial F on 2-sphere (S=0) or product of  $L_i$ . By the given relation of  $x=i(\alpha^2-1), y=-2i\alpha, z=\alpha^2+1$ , spherical harmonics can be expanded as  $\alpha$  terms (see C.1), therefore, the dipole  $(T_1)$ , quadrupole  $(T_2)$  and octopole  $(T_3)$  are described as  $\alpha$  terms with the  $a_{lm}$  as coefficients. Once we read off the  $a_{lm}$ s from maps, we may find the roots  $\alpha$  which satisfy equations  $T_l=0$  for each l. These roots give a pair of  $\{f_l, \bar{f}_l\}$ , therefore, from equation (5.3) we obtain solution sets  $v_i^l=(a_i,b_i,c_i)$  which are multipole vectors for each l.

Dipole: l=1.

$$T_{1} = \sum_{m} a_{1m} Y_{1m}$$

$$= \sqrt{\frac{3}{2\pi}} (a_{11}^{Re} x - a_{11}^{Im} y + \frac{a_{10}}{\sqrt{2}} z)$$
(5.5)

The dipole vector does not need to be represented by the  $\alpha$  notation since it is linear equation as x, y and z. By polynomial notation, the dipole is

also represented as

$$F = L_1 = \lambda_1 (a_1 x + b_1 y + c_1 z). \tag{5.6}$$

From the normalization, we obtain the multipole vector such as

$$v_1 = \left(\sqrt{\frac{2}{3C_1}}a_{11}^{Re}, -\sqrt{\frac{2}{3C_1}}a_{11}^{Im}, \frac{1}{\sqrt{3C_1}}a_{10}\right)$$
 (5.7)

With the coefficient,

$$\lambda_1 = \sqrt{\frac{3}{2\pi}} \sqrt{a_{11}^{2Re} + a_{11}^{2Im} + \frac{1}{2}a_{10}^2} = \sqrt{\frac{3}{2\pi}} \sqrt{a_{11}^2 + \frac{1}{2}a_{10}^2} = \frac{3}{2} \sqrt{\frac{C_1}{\pi}} (5.8)$$

where the  $C_1 = 1/3(2|a_{11}|^2 + a_{10}^2)$  is the angular power spectrum  $C_l$  of the monopole.

Quadrupole: l=2. We need to expand this as  $\alpha$  notation since multipoles, from the quadrupole to higher order, can not be described as linear equations. The quadrupole on a sphere has two multipole vectors,  $v_1^2$  and  $v_2^2$  from  $F = \lambda_2 \cdot L_1 \cdot L_2 = \lambda_2 \cdot (a_1x + b_1y + c_1z) \cdot (a_2x + b_2y + c_2z)$ . In order to find them, we transfer the quadrupole expression from spherical harmonics to  $\alpha$  notation for efficient computing,

$$T_{2} = \sum_{m} a_{2m} Y_{2m}$$

$$= (\sqrt{\frac{3}{2}} a_{20} - a_{22}^{Re} + 2ia_{21}^{Re}) \alpha^{4} - 4(a_{22}^{Im} - ia_{21}^{Im}) \alpha^{3} + (\sqrt{6}a_{20} + 6a_{22}^{Re}) \alpha^{2} + 4(a_{22}^{Im} + ia_{21}^{Im}) \alpha + \sqrt{\frac{3}{2}} a_{20} - a_{22}^{Re} - 2ia_{21}^{Re}$$

$$(5.9)$$

Octopole: l=3. In the same way we have done for the quadrupole, since the octopole obtain three multipole vectors,  $v_1^3$ ,  $v_2^3$  and  $v_3^3$  from  $F=\lambda_3 \cdot L_1 \cdot L_2 \cdot L_3 = \lambda_3 (a_1x + b_1y + c_1z) \cdot (a_2x + b_2y + c_2z) \cdot (a_3x + b_3y + c_3z)$ , we have the  $6^{th}$  order of equation as  $\alpha$ :

$$T_3 = \sum_m a_{3m} Y_{3m}$$
  
=  $A_6 \alpha^6 + A_5 \alpha^5 + A_4 \alpha^4 + A_3 \alpha^3 + A_2 \alpha^2 + A_1 \alpha + A_0.$  (5.10)

With the coefficients such as

$$A_{6} = 5a_{30} - \sqrt{30}a_{32}^{Re} + (-5\sqrt{3}a_{31}^{Re} + \sqrt{5}a_{33}^{Re})i$$

$$A_{5} = -4\sqrt{30}a_{32}^{Im} + (-10\sqrt{3}a_{31}^{Im} + 6\sqrt{5}a_{33}^{Im})i]$$

$$A_{4} = 5[3a_{30} + \sqrt{30}a_{32}^{Re} - (\sqrt{3}a_{31}^{Re} + 3\sqrt{5}a_{33}^{Re})i$$

$$A_{3} = -20(\sqrt{3}a_{31}^{Im} + \sqrt{5}a_{33}^{Im})i$$

$$A_{2} = \bar{A}_{4}, \quad A_{1} = -\bar{A}_{5}, A_{0} = \bar{A}_{6}.$$

Each multipole has 2l roots of  $\alpha$  which give  $(f_i, \bar{f}_i)$  pair, however, only l components are used to find the multipole since their conjugators give same results as we mentioned earlier.

#### 5.2.2 Results

The Figure 5.2.2 is good example which shows how strongly multipoles are correlated. The dipole (left) lies exactly on the top of sphere which is the centre of the image. The two quadrupole vectors (middle) are located on

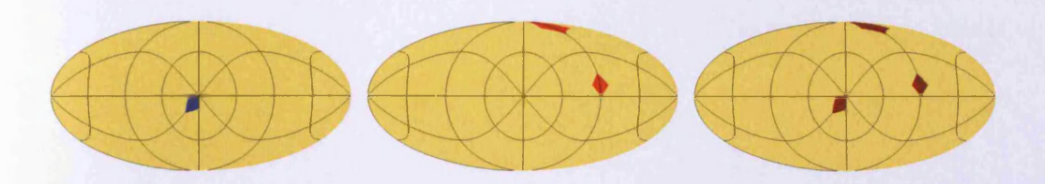


FIGURE 5.12: The multipole vectors from BianchiV map such as The dipole (left), quadrupole (middle) and octopole (right).

the same spots on which two of octopole vectors (right) are placed. The remaining octopole vector is in the centre, i.e. the same place as the dipole.

Now we plot the dipole, quadrupole and octopole on the same 2-sphere for all the Bianchi maps, at different redshifts, to see how exactly they overlap (see Figure 5.13).

Bianchi Maps. First of all, in all types of models, we see the quadrupole and octopole vectors lie on the same plane, except for one of the octopole vector located in north pole which is chosen to be in centre of the image. For Bianchi V and VII<sub>h</sub> types, the dipole vectors lie very near the north pole in the early stage but not exactly on it. However, as time goes on, the dipole vector is overlapped by one of the octopole vectors on north pole. The dipole vector of Bianchi VII<sub>0</sub> type is different from Bianchi VII<sub>h</sub>. In Bianchi VII<sub>0</sub> type, there is no particular correlation between the dipole and other multipoles since the dipole is not coupled with the other multipoles (quadrupole and octopole). However, one similarity with the other models, type V and VII<sub>h</sub> is that the quadrupole and octopole are on the same plane. For the Bianchi V (left), at the beginning of the stage, the dipole vector is 'almost' on the z-axis. One of octopole vectors is exactly on the z-axis, top

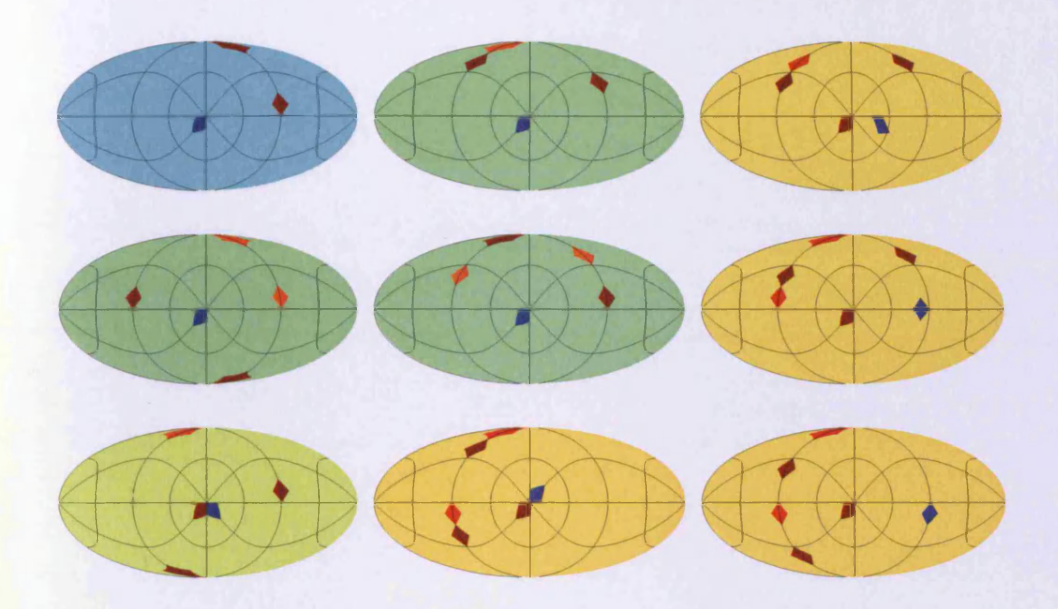


FIGURE 5.13: The multipole vectors from the Bianchi V (left),  $VII_h$  (middle) and  $VII_0$  (right) maps from early stage (bottom panel) to late time (top panel). These vectors are represented by dots as dark blue for dipole, as light red for quadrupole and as brown for octopole. Background colours also indicate if any of the multipoles over-lap; yellow for no overlapped multipoles (right row and bottom of middle row), green for overlapped dipole and octopole, light yellow (bottom of left row) for quadrupole and octopole and light blue (top of left row) if all the multipole vectors are overlapped.

of north, on the other hand, two present Bianchi V case on the top left of Figure 5.13, it shows that the dipole and octopole are on the same spot, in the middle of the image, which is exactly on the z-axis. Meanwhile, one of components of quadrupole and octopole vectors are on the same spot on the x-y plane. This means that the more recent Bianchi V models has extreme correlation between the multipoles.

Bianchi Maps with initial dipole. In early stage, at the bottom of Figure 5.14, the quadrupole and octopole vectors have not much difference

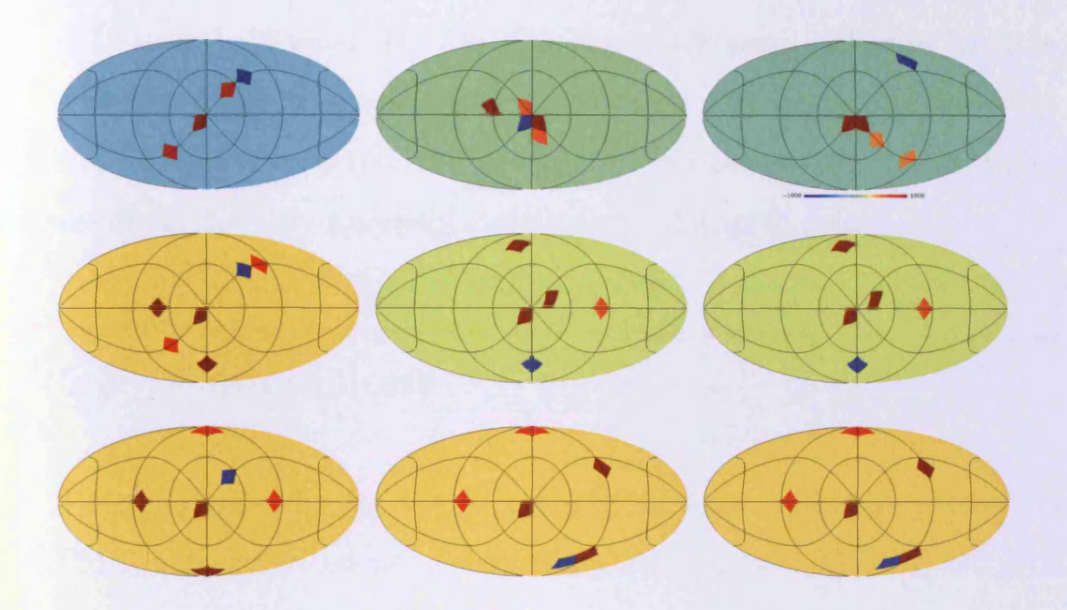


FIGURE 5.14: Same figure, but for initial dipole.

from previous cases which do not have initial dipole: Two quadrupole vectors and two octopole vectors are still placed on the same plane, and one remaining octopole vector is located on the north-pole. However, dipole vector lies in an arbitrary position since there is no correlation between dipole and another multipoles in Boltzmann equation for given initial dipole. A remarkable feature develops during time evolution: the quadrupole and octopole vectors move gradually away from the original plane. As Bianchi V, which contains the initial dipole, in the top of Figure 5.14, they appear somehow aligned with even dipole and settle to the new plane which seems to be parallel to z-axis or orthogonal from original plane in which they aligned at the beginning. Moreover, it shows the strong correlation between them such that the dipole and quadrupole vectors are overlapped and quadrupole and octopole vectors are on the same spot. We also can see this alignment from temperature patterns of Bianchi V with initial dipole

in Chapter 4. However, Bianchi VII<sub>h</sub> case in left panel of Figure 5.14, the octopole vectors has overlapped with another multipoles such as the dipole (top) and quadrupole (middle) vectors. One noticeable change of multipole vectors is that they gradually move towards the north pole.

#### 5.3 Conclusions

The aim of this chapter was to characterize the temperature patterns in CMB maps generated using anisotropic Bianchi type V,  $VII_h$  and  $VII_0$  universes. The overall aim of investigating this behavior was to find an optimal way to isolate the effect of anisotropy from that of non-Gaussianity. Note when we talk about non-Gaussianity here is not related to a stochastic field; there are no fluctuations in the Bianchi maps. Two different methods were introduced.

The pixel analysis was chosen because at first glance it might seem the simplest and most obvious test to implement. The pixel distribution histograms were found for each of the maps and compared to results expected in a universe consistent with the concordance model. The type  $VII_0$  map showed the most deviation from the null hypothesis; types V and  $VII_h$  showed similar results which looked to tend towards the null hypothesis. The reason these two give smaller anomalies was because the focusing effect on each meant that more and more of the map area looked uniform like the null hypothesis. So the metric was good at picking out non-Gaussianity in cases where the map had only a twisted feature, but not when there was focussing.

Multipole analysis is also a relatively new technique. It has been used to identify non-Gaussianities in the WMAP data, and has been particularly successful in identifying anisotropies i.e. asymmetries and/or preferred directions. Also, multipole vectors are calculated using spherical harmonic coefficients which we already knew were a very effective way of identifying correlations in Bianchi (if not other anisotropic) maps. But the advantage of multipole vectors, over spherical harmonics, is that they give results in real, or pixel, space which is much more informative to the user. The results when applied to the Bianchi maps show strong correlations exist between the multipole vectors for low l, often with them overlapping, and hence showing preferred directions.

So this analysis has shown that the correlations present in the the CMB maps from Bianchi universes can be quantified using these relatively simple tools.

# Chapter 6

## Conclusions and Discussion

The goal of this thesis has been to compute the temperature and polarization patterns produced in anisotropic relativistic cosmologies described by various Bianchi types. We focussed on those types that contain the standard homogeneous and isotropic FRW background as a limiting case. We stress again that these models are not consistent with parameter determinations of the standard cosmological framework so they are probably not viable alternative models for the structure of the Universe. We do, however, feel that they comprise an interesting and fairly general set of alternative hypothesis against which we can attempt to tune our statistical techniques.

In order to construct the distributions generated in these models we constructed an appropriate description of the radiation field in terms of spin-0 and spin-2 components representing the unpolarized and polarized parts, respectively. We integrated the equations for the radiation field numerically, and presented a number of illustrative examples.

The basic point behind this this study is related to the physical origin of CMB polarization: radiation affected by Thomson scattering from an electron in a radiation field possessing a quadrupole anisotropy will inevitably be partially linearly polarized. In the context of standard cosmological models, the environment of different electrons varies owing to the presence of density inhomogeneities and a background of gravitational waves. These sources of variation are stochastic so the variations in the polarized component of the radiation field, though correlated with the temperature variations, are essentially incoherent. In Bianchi cosmologies, however, global homogeneity requires that each electron sees the same quadrupole. The polarized part of the radiation field is therefore coherent, and is in a fixed relationship to the temperature variation (once the model is specified).

We applied techniques borrowed from the literature to this problem and constructed a set of numerical codes capable of computing the temperature and polarization patterns for general cases of each model. In addition we also derived a number of specific results analytically. We have shown, for example, that it is possible, in a Bianchi V cosmological model, to generate a localized temperature anomaly qualitatively similar to the known Cold Spot without necessarily producing a large B-mode polarization. This requires a specific choice of model, however, and we have no fundamental argument as to why the Universe should be described by this geometry.

We stress again that there are severe difficulties with anisotropic universes as explanations for the overall pattern of observed CMB anomalies. Most important among these is that a significant (negative) spatial curvature seems to be at odds with measurements that clearly prefer a flat universe

[15, 16]. Nevertheless, these models may provide important clues that can lead to more effective and efficient use of observations to test exotic cosmologies. For example, there are other ways in which the polarization angle for CMB photons can be rotated [92]; the lack of any observed B-mode allows present observations to place strong constraints on such models also [93].

We then analysed the maps we generated using some simple of statistical measures of anisotropy. The motivation for this is that it is important to understand how standard statistical techniques, designed to be applied to stationary stochastic fluctuations, perform when applied to patterns which are neither stochastic nor stationary (nor indeed standard). If a statistical technique does not register anything significant when applied to a highly asymmetric model, it is unlikely to yield anything significant when subjected to subtler tests.

We explored the properties of the pixel distributions first because at first glance it might seem the simplest and most obvious test to implement. The pixel distribution functions were found for each of the maps and compared to results expected in a universe consistent with the concordance model. The type  $VII_0$  map showed the most deviation from the null hypothesis; types V and  $VII_h$  showed similar results which looked to tend towards the null hypothesis. The reason these two give smaller anamolies was because the focusing effect on each meant that more and more of the map area looked uniform like the null hypothesis. So the metric was good at picking out non-Gaussianity in cases where the map had only a twisted feature, but not when there was focussing.

Multipole analysis is also a relatively new technique. It has been used to identify non-Gaussianities in the WMAP data, and has been particularly successful in identifying anisotropies i.e. asymmetries and/or preferred directions. Also, multipole vectors are calculated using spherical harmonic coefficients which we already knew were a very effective way of identifying correlations in Bianchi (if not other anisotropic) maps. But the advantage of multipole vectors, over spherical harmonics, is that they give results in real, or pixel, space which is much more informative to the user. The results when applied to the Bianchi maps show strong correlations exist between the multipole vectors for low l, often with them overlapping, and hence showing strongly preferred directions.

Interesting though these results are, they represent only a first step towards the statistical characterization of CMB asymmetry. The statistical tools we have demonstrated here are very simple and a wide range of alternative descriptions will also need to be evaluated. These Bianchi models yield patterns which have highly correlated spherical harmonic components in contrast to the case of a homogeneous Gaussian random field in which the harmonic modes are independent. It is important to understand how CMB fluctuations arising from Bianchi-type universes impact on orthodox analysis procedures and whether they produce characteristic signatures when analysed in this way, particularly in the presence of additional stochastic fluctuations. Higher-order statistics will be necessary to provide a fuller characterization of the coherent anisotropic fluctuations we have studied here.

Moreover, present and future CMB experiments are largely aimed at improving the precision of *polarization* measurements in order to find evidence of a stochastic background of primordial gravitational waves. Techniques advocated to measure polarization pattern over the celestial sphere are therefore also generally tuned to detect signals of an incoherent nature. The presence of coherent signals in the CMB could be an indication of physics beyond the standard cosmological framework. It is especially interesting, therefore, to generalize the statistical methods used so far to study temperature anisotropies (described by a spin-0 scalar field) to the more complicated case of the polarized component (which requires a description in terms of spin-2 objects). The traditional method for analysing polarization is via a decomposition into odd and even parity modes. While this does yield interesting insights into the behaviour of the Bianchi models discussed above, it is by no means obvious that it furnishes optimal descriptors for coherent fields such as these.

We have only made very preliminary steps towards using analysing the polarization produced in these models and the primary aim of our future work will be to take this aspect of the study further. This will hopefully lead us to better ways of searching for departures from the concordance cosmology using the next generation of datasets.

# Appendix A

### A.1 Liouville Equation

Associated with spin s quantities are the spin raising and lowering operators  $\eth$  and  $\bar{\eth}$ , respectively

$$\vec{\eth}_s F^s = -\sin^s \theta \left( \frac{\partial}{\partial \theta} + \frac{i}{\sin \theta} \frac{\partial}{\partial \phi} \right) (\sin^{-s} \theta F^s) = (s \cot \theta + \vec{\eth}_0) F^s 
\bar{\vec{\eth}}_s F^s = -\sin^{-s} \theta \left( \frac{\partial}{\partial \theta} - \frac{i}{\sin \theta} \frac{\partial}{\partial \phi} \right) (\sin^s \theta F^s) = (-s \cot \theta + \bar{\vec{\eth}}_0) F^s (A.1)$$

which gives the relation between the spin zero and spin operator is  $\eth_s = \eth_0 + s \cot \theta$  and  $\bar{\eth}_s = \bar{\eth}_0 - s \cot \theta$ .

Let us apply to in the Liouville equation to find the extra term for  $N^2$  from angle variation part:

$$\frac{\gamma^{i}}{\sqrt{2}}(m^{i}\bar{\eth}_{s} + \bar{m}\eth_{s})N^{s} = \frac{\gamma^{i}}{\sqrt{2}}[m^{i}(-s\cot\theta + \bar{\eth}_{0})N^{s} + \bar{m}^{i}(s\cot\theta + \bar{\eth}_{0})N^{s}]$$

$$= \frac{\gamma^{i}}{\sqrt{2}}[-s\cot\theta(m^{i} - \bar{m}^{i})N^{s} + (m^{i}\bar{\eth}_{0} + \bar{m}^{i}\bar{\eth}_{0})N^{s}]$$

$$= is\cos\theta\frac{1}{\varepsilon}\frac{d\phi}{d\lambda}N^{s} + \frac{\gamma^{i}}{\sqrt{2}}(m^{i}\bar{\eth} + \bar{m}\bar{\eth})N^{s}. \tag{A.2}$$

From the result of this equation, the convection part for  $N^2$  is given by

$$\frac{\gamma^{i}}{\sqrt{2}}(m^{i}\bar{\eth}_{2} + \bar{m}\eth_{2})N^{2} = 2i\cos\theta\frac{1}{\varepsilon}\frac{d\phi}{d\lambda}N^{2} + \frac{\gamma^{i}}{\sqrt{2}}(m^{i}\bar{\eth} + \bar{m}\eth)N^{2}. (A.3)$$

### A.2 Scattering

It is easily seen that the emission term  $J_A$  contains only harmonics up to l=2 using orthonormal relations in equation (3.20). If we substitute equation (3.18) in equation (3.15), we take the following forms:

$$J_{0} = \int \left[ p_{0B} N^{B} + \hat{p}_{0B} \bar{N}^{B} \right] \frac{d\Omega'}{4\pi}$$

$$= \int \left[ (1 + \frac{3}{4} k^{ik} k^{ik'})^{Re} N^{0} + k^{i} k^{i'} i^{Im} N^{0} - \frac{3}{4} (k^{ik} \bar{m}^{ik'} N^{2} + \bar{k}^{ik} \bar{m}^{ik'} N^{2}) \right] \frac{d\Omega'}{4\pi}$$

$$= \int^{Re} N^{0} \frac{d\Omega'}{4\pi} + \frac{3}{4} k^{ik} \int^{Re} N^{0} k^{ik'} \frac{d\Omega'}{4\pi} + k^{i} i \int^{Im} N^{0} k^{i'} \frac{d\Omega'}{4\pi}$$

$$- \frac{3}{4} k^{ik} \int \left( N^{2} \bar{m}^{ik'} + \bar{k}^{ik} \bar{m}^{ik'} N^{2} \right) \frac{d\Omega'}{4\pi}$$

$$= {}^{Re} N^{0}_{0} + \frac{i}{3} k^{iIm} N^{0}_{i} + \frac{1}{10} k^{ikRe} N^{0}_{ik} - \frac{3}{10} k^{ikRe} N^{2}_{ik}$$
(A.4)

$$J_{2} = \int \left[ p_{2B} N^{B} + \hat{p}_{2B} \bar{N}^{B} \right] \frac{d\Omega'}{4\pi}$$

$$= \int \left[ -\frac{3}{2} m^{ik} k^{ik'Re} N^{0} + \frac{3}{2} m^{ik} (\bar{m}^{ik'} N^{2} + \bar{m}^{ik'} N^{2}) \right] \frac{d\Omega'}{4\pi}$$

$$= -\frac{3}{2} m^{ik} \int_{Re}^{Re} N^{0} k^{ik'} \frac{d\Omega'}{4\pi} + \frac{3}{2} m^{ik} \int_{Re}^{Re} (N^{2} \bar{m}^{ik'} + \bar{N}^{2} \bar{m}^{ik'}) \frac{d\Omega'}{4\pi}$$

$$= -\frac{1}{5} m^{ikRe} N^{0}_{ik} + \frac{3}{5} m^{ikRe} N^{2}_{ik}. \tag{A.5}$$

#### A.3 Ricci rotation coefficients

The  $\gamma^a_{\ bc}$  has a direct geometrical interpretation as a component of a Lie derivative [54, 80]:

$$\gamma_{i0}^{0} = \dot{u}_{i},$$

$$\gamma_{ij}^{0} = -2\epsilon_{ijk}\omega^{k},$$

$$\gamma_{0i}^{i} = -\theta_{i},$$

$$\gamma_{j0}^{i} = \theta_{ij} + \epsilon_{ijk}\omega^{k} - \mathbf{e}_{i} \cdot \dot{\mathbf{e}}_{j},$$

$$\gamma_{0j}^{i} = -\sigma_{ij} - \epsilon_{ijk}\omega^{k} + \mathbf{e}_{i} \cdot \dot{\mathbf{e}}_{j} \quad (i \neq j),$$

$$\gamma_{ji}^{i} = \mathbf{e}_{j} \cdot \nabla_{i}\mathbf{e}_{i},$$

$$\gamma_{ik}^{i} = \delta_{k}^{i}a_{j} - \delta_{j}^{i}a_{k} + \epsilon_{jkl}n_{i}^{l}$$
(A.6)

From equation (2.30) the rotation coefficients and the commutation functions are linear combinations of the other:

$$\Gamma^{0}_{0i} = \dot{u}_{i},$$

$$\Gamma^{0}_{ij} = \theta_{ij} - \epsilon_{ijk}\omega^{k},$$

$$\Gamma^{i}_{j0} = \theta_{ij} + \epsilon_{ijk}\omega^{k},$$

$$\Gamma^{i}_{0j} = \mathbf{e}_{i} \cdot \dot{\mathbf{e}}_{j},$$

$$\Gamma^{i}_{jk} = \delta^{j}_{k}a_{i} - \delta^{i}_{j}a_{k} + \frac{1}{2}(\epsilon_{ljk}n^{l}_{i} - \epsilon_{ilk}n^{l}_{j} + \epsilon_{ijl}n^{l}_{k}).$$
(A.7)

The first three sets contain the kinematic variables. The quantities  $a_i$  and  $n_{ij}$  in the last set determine the 9 spatial rotation coefficients.

The antisymmetry of  $\Gamma^c_{\phantom{c}ab}\eta_{cd}$  in b and d leads to

$$\begin{split} &\Gamma^{0}{}_{a0} &= 0 \\ &\Gamma^{0}{}_{0i} &= \Gamma^{i}{}_{00}, \\ &\Gamma^{0}{}_{ji} &= \Gamma^{i}{}_{j0}, \\ &\Gamma^{i}{}_{0j} &= -\Gamma^{j}{}_{0i}, \\ &\Gamma^{i}{}_{kj} &= -\Gamma^{j}{}_{ki}. \end{split}$$

Note that some papers take the different definition of Ricci coefficients [57, 99]:

$$\Gamma_{abc} = e_a^{\alpha} e_{b\alpha;\beta} e_c^{\beta}.$$

By above notation, the coefficients is antisymmetry not of b and c but of a and b:

$$\Gamma_{abc} + \Gamma_{bac} = 0$$

Which gives

$$\Gamma_{abc} = \frac{1}{2}(\gamma_{acb} + \gamma_{cab} - \gamma_{bca}).$$

### A.4 Coefficients of Boltzmann Equation

From the results in A.3 the coefficients of the Boltzmann equations are also represented by different components:

$$\hat{A}_{i}^{k} = -\frac{1}{5}(\theta \delta^{ik} + 2\theta_{ik}) = -\frac{1}{3}\theta \delta_{ik} - \frac{2}{5}\sigma_{ik}, 
\hat{B}_{i}^{k} = -\frac{3}{5}\sigma_{ik}, 
\hat{C}_{i}^{kl} = \frac{2}{5}\left(\epsilon_{iks}n_{l}^{s} + \frac{1}{2}\epsilon_{kls}n_{i}^{s} - 3a_{k}\delta_{il} + a_{i}\delta_{kl}\right), 
\hat{D}_{ij}^{k} = 0, 
\hat{E}_{ij} = -\theta_{ij}, 
\hat{F}_{ij}^{kl} = -2\theta\delta^{ik}\delta^{jl} - \frac{24}{7}\sigma_{il}\delta^{jk}, 
\hat{G}_{ij}^{kl} = -\frac{6}{7}\sigma_{ik}\delta_{jl}, 
\hat{H}_{ij}^{k} = \frac{1}{2}(\epsilon_{ljk}n_{l}^{l} - \epsilon_{ilk}n_{j}^{l} + \epsilon_{ijl}n_{k}^{l}) + (\delta_{j}^{k}a_{i} - \delta_{j}^{i}a_{k}), 
\hat{K}_{ij}^{kl} = -\frac{1}{7}\left(-\frac{1}{3}\theta\delta_{ik} + \sigma_{ik}\right), 
\hat{L}_{ij}^{kl} = \frac{6}{7}(\theta_{ik} - \theta\delta_{ik})\delta^{jl}, 
\hat{M}_{ij}^{kl} = \frac{1}{7}\left(\frac{11}{3}n_{s}^{s}\delta^{ik} - 4n_{k}^{i}\right)\delta^{jl}.$$
(A.8)

We used the results for obtaining  $\hat{M}^{kl}_{ij}$  such as

$$\begin{split} \epsilon^{uvi}\Gamma^v_{\ ku}\delta^{jl} + \epsilon^{uvl}\Gamma^v_{\ ju}\delta^{ik} &= (\epsilon^{uvi}\Gamma^v_{\ ku}\delta^{jl} + \epsilon^{uvk}\Gamma^v_{\ iu})\delta^{jl} \\ &= (2n^l_l\delta_{ik} - 2n^l_i\delta_{kl} - 2n^l_k\delta_{il})\delta^{jl} \\ &= (2(n_1 + n_2 + n_3)\delta_{ik} - 4n^i_k)\delta^{jl} \end{split}$$



which comes from

$$\epsilon^{uvi}\Gamma^{v}_{ku} = \frac{1}{2}\epsilon^{uvi}(\epsilon_{lku}n^{l}_{v} - \epsilon_{vlu}n^{l}_{k} + \epsilon_{vkl}n^{l}_{u}) + \epsilon^{uvi}(\delta^{u}_{k}a^{l}_{v} - \delta^{v}_{k}a_{u})$$

$$= n^{l}_{l}\delta_{ik} - 2n^{i}_{k} - 2\epsilon^{uki}a_{u}, \tag{A.9}$$

and the relations:

$$\epsilon_{ijk}\epsilon_{ilm} = \delta_{jl}\delta_{km} - \delta_{jm}\delta_{kl}$$

$$\epsilon_{ijk}\epsilon_{ijm} = 2\delta_{km}.$$
(A.10)

#### A.5 Extra terms from the geodesic equation

If we consider the case which do not necessarily have isotropic FRW limit, the geodesic equation has extra terms by shear:

$$\left(\frac{d\theta}{d\lambda}\right)_{\sigma} = \frac{\partial k_{i}}{\partial \theta} \Gamma^{0}_{ki} k^{k} = \frac{\partial k^{i}}{\partial \theta} \theta_{ik} k^{k} 
= \frac{1}{3} \theta k^{i} \frac{\partial k_{i}}{\partial \theta}_{=0} + \frac{\sigma_{ii} k^{i} \frac{\partial k_{i}}{\partial \theta}}{\partial \theta}_{\equiv 0} + \sigma_{12} \left(k^{2} \frac{\partial k_{1}}{\partial \theta} + k^{1} \frac{\partial k_{2}}{\partial \theta}\right) 
+ \sigma_{13} \left(k^{3} \frac{\partial k_{1}}{\partial \theta} + k^{1} \frac{\partial k_{3}}{\partial \theta}\right) + \sigma_{23} \left(k^{3} \frac{\partial k_{2}}{\partial \theta} + k^{2} \frac{\partial k_{3}}{\partial \theta}\right), \quad (A.11)$$

And

$$\left(\frac{d\phi}{d\lambda}\right)_{\sigma} = \frac{b_{i}}{\sin\theta} \Gamma^{0}_{ki} k^{k} = \frac{\partial k^{i}}{\partial\theta} \theta_{ik} k^{k} 
= -\sin\phi \theta_{k2} k^{k} + \cos\phi \theta_{k3} k^{k} 
= -\sin\phi \left(\frac{1}{3}\theta \delta_{k2} + \sigma_{k2}\right) k^{k} + \cos\phi \left(\frac{1}{3}\theta \delta_{k3} + \sigma_{k3}\right) k^{k} 
= -\sin\phi (\sigma_{k2} k^{k}) + \cos\phi (\sigma_{k3} k^{k}).$$
(A.12)

## A.6 Variation of Complex Vector, $m^i$ .

By relations such as

$$\eth m^{i} = 0 \quad \rightarrow \quad \frac{\partial m^{i}}{\partial \theta} = -\frac{1}{\sqrt{2}}k^{i},$$

$$\bar{\eth} m^{i} = \sqrt{2}k^{i} \quad \rightarrow \quad \frac{\partial m^{i}}{\partial \phi} = -i(\cos\theta m^{i} + \frac{1}{\sqrt{2}}\sin\theta k^{i}), \qquad (A.13)$$

The change of complex vector  $m^j$  is given as

$$dm^{j} = \frac{\partial m^{j}}{\partial \theta} d\theta + \frac{\partial m^{j}}{\partial \phi} d\phi$$

$$= -\frac{1}{\sqrt{2}} (d\theta + i \sin \theta d\phi) k^{j} - i m^{j} \cos \theta d\phi$$

$$= -\frac{1}{\sqrt{2}\varepsilon} (a_{l} + i b_{l}) p^{l} k^{j} - \frac{i}{\varepsilon} m^{j} \cot \theta b_{l} dp^{l}$$

$$= -\frac{1}{\varepsilon} (m_{l} k^{j} + i m^{j} \cot \theta b_{l}) dp^{l}. \tag{A.14}$$

Then finally we obtain the equation such as

$$\varepsilon dm^{j} = -k^{j} m_{l} dp^{l} - i m^{j} \cot \theta b_{l} dp^{l}. \tag{A.15}$$

If the directions of polarization are rotated,  $m^j=e^{-i\psi}S^j$ , its covariant derivative is

$$m_{,b}^{j}p^{b} = -i\frac{d\psi}{d\lambda}m^{j} + S_{,b}^{j}p^{b}.$$
 (A.16)

Then  $m^j_{;b}p^b \times i\bar{m}_j$  gives

$$\frac{d\psi}{d\lambda} = i\bar{m}_{j}(m_{,b}^{j}p^{b}) - i\bar{m}_{j}S_{,b}^{j}p^{b}$$

$$= i\bar{m}_{j}(\frac{dm^{j}}{d\lambda} + \Gamma_{bl}^{j}m^{l}p^{b})$$

$$= i\frac{\bar{m}_{j}}{\varepsilon} \left[ -k^{j}m_{l}\frac{dp^{l}}{d\lambda} + \varepsilon\Gamma_{bl}^{j}m^{l}p^{b} \right] + \frac{1}{\varepsilon}\cot\theta b_{l}\frac{dp^{l}}{d\lambda}. \quad (A.17)$$

First term is canceled out because  $m_j k^j = 0 = \overline{m_j k^j} = \overline{m}_j k^j$ .

Then the change of  $\psi$  is

$$\frac{d\psi}{d\lambda} = i\bar{m}_{j}\Gamma^{j}_{bl}m^{l}p^{b} + \frac{1}{\varepsilon}\cot\theta b_{l}\frac{dp^{l}}{d\lambda} 
= i\bar{m}_{j}m^{l}\varepsilon(\Gamma^{j}_{0l} + \Gamma^{j}_{il}k^{i}) - \varepsilon\cot\theta b_{l}\gamma^{l} 
= \frac{1}{2}\epsilon^{ljk}\Gamma^{j}_{il}\varepsilon k^{i}k^{k} - \varepsilon\cot\theta b_{l}\gamma^{l} 
= \frac{1}{2}\epsilon^{ljk}\Gamma^{j}_{il}\varepsilon k^{i}k^{k} + \cos\theta\frac{d\phi}{d\lambda}.$$
(A.18)

Where we used the antisymmetry of a and c in  $\Gamma^a{}_{bc}$  and the relation,  $\tfrac{1}{2}(m^l\bar{m}^j-\bar{m}^lm^j)=-\tfrac{i}{2}\epsilon^{ljk}k^k.$ 

From equation (A.9) we obtain

$$\epsilon^{ikm} \Gamma^k_{li} k^l k^m = (n_s^s \delta^{ml} - 2n_l^m - \epsilon^{ilm} a_i) k^l k^m = n_s^s - 2n_l^m k^l k^m.$$
 (A.19)

# Appendix B

## **B.1** $a_{E,lm}$ and $a_{B,lm}$ from $N^2$

From the multipole expansion of  $N^2$  which has spin weight two:

$$\begin{split} N^2 &= m^{ij}N_{ij}^2 + \dots \\ &= \frac{1}{12C_2} \Big[ \frac{2}{\sqrt{6}} N_{112}^2 Y_{20} + N_{12}^2 (_2 Y_{21} - _2 Y_{2-1}) - i N_{13}^2 (_2 Y_{21} + _2 Y_{2-1}) \\ &+ \frac{1}{2} N_{22}^2 (_2 Y_{22} + _2 Y_{2-2}) - \frac{1}{\sqrt{6}} N_{222}^2 Y_{20} - i N_{23}^2 (_2 Y_{22} - _2 Y_{2-2}) \\ &- \frac{1}{2} N_{33}^2 (_2 Y_{22} + _2 Y_{2-2}) - \frac{1}{\sqrt{6}} N_{332}^2 Y_{20} \Big] + \dots \\ &= \frac{1}{12C_2} \Big[ \frac{2}{\sqrt{6}} \Big( N_{11}^2 - \frac{1}{2} (N_{22}^2 + N_{33}^2) \Big)_2 Y_{20} + (N_{12}^2 - i N_{13}^2)_2 Y_{21} - (N_{12}^2 + i N_{13}^2)_2 Y_{2-1} \\ &+ \frac{1}{2} (N_{22}^2 - N_{33}^2 - 2i N_{23}^2)_2 Y_{22} + \frac{1}{2} (N_{22}^2 - N_{33}^2 + 2i N_{23}^2)_2 Y_{2-2} \Big] + \dots \end{split}$$

We obtain the  $a_{2,lm}$  components of  $N_{ij}^2$ :

$$a_{2,20} = \frac{1}{6\sqrt{6}C_2} \left( N_{11}^2 - \frac{1}{2} (N_{22}^2 + N_{33}^2) \right) \quad a_{-2,20} = \frac{1}{6\sqrt{6}C_2} \left( \bar{N}_{11}^2 - \frac{1}{2} (\bar{N}_{22}^2 + \bar{N}_{33}^2) \right),$$

$$a_{2,21} = \frac{1}{12C_2} (N_{12}^2 - iN_{13}^2) \qquad a_{-2,21} = \frac{1}{12C_2} (\bar{N}_{12}^2 - i\bar{N}_{13}^2),$$

$$a_{2,2-1} = -\frac{1}{12C_2} (N_{12}^2 + iN_{13}^2) \qquad a_{-2,2-1} = -\frac{1}{12C_2} (\bar{N}_{12}^2 + i\bar{N}_{13}^2),$$

$$a_{2,22} = \frac{1}{24C_2} (N_{22}^2 - N_{33}^2 - 2iN_{23}^2) \qquad a_{-2,22} = \frac{1}{24C_2} (\bar{N}_{22}^2 - \bar{N}_{33}^2 - 2i\bar{N}_{23}^2),$$

$$a_{2,2-2} = \frac{1}{24C_2} (N_{22}^2 - N_{33}^2 + 2iN_{23}^2) \qquad a_{-2,2-2} = \frac{1}{24C_2} (\bar{N}_{22}^2 - \bar{N}_{33}^2 + 2i\bar{N}_{23}^2).$$

$$(B.1)$$

Where we used the relation,  $a_{-2,lm} = (-1)^m \bar{a}_{2,l-m}$ .

Instead of  $a_{\pm 2,lm}$ , it is useful to use their linear combinations

$$a_{E,lm} = -\frac{1}{2}(a_{2,lm} + a_{-2,lm}), \quad \bar{a}_{E,lm} = (-1)^m a_{E,l-m}.$$
 (B.2)

By the equation (B.1) E-modes can be represented by using  $N_{ij}^2$ :

$$a_{E,20} = -\frac{1}{6\sqrt{6}C_2} \left( {^{Re}N_{11}^2 + \frac{1}{2} (^{Re}N_{22}^2 + ^{Re}N_{33}^2)} \right)$$

$$a_{E,21} = -\frac{1}{12C_2} (^{Re}N_{12}^2 - i^{Re}N_{13}^2)$$

$$a_{E,2-1} = \frac{1}{12C_2} (^{Re}N_{12}^2 + i^{Re}N_{13}^2)$$

$$a_{E,22} = -\frac{1}{24C_2} (^{Re}N_{22}^2 - ^{Re}N_{33}^2 - 2i^{Re}N_{23}^2)$$

$$a_{E,2-2} = \frac{1}{24C_2} (^{Re}N_{22}^2 - ^{Re}N_{33}^2 + 2i^{Re}N_{23}^2)$$
(B.3)

From results in the equation (B.3) real parts of  $N_{ij}^2$  produce the E-modes.

As the same method of decomposition of E-modes, we also can obtain the B-modes. There is linear combination such as

$$a_{B,lm} = \frac{i}{2}(a_{2,lm} - a_{-2,lm}), \quad \bar{a}_{B,lm} = (-1)^m a_{B,l-m}.$$
 (B.4)

From the equation (B.1) B-modes can be obtained from  $N_{ij}^2$ :

$$a_{B,20} = -\frac{1}{6\sqrt{6}C_2} \left( {}^{Im}N_{11}^2 + \frac{1}{2} ({}^{Im}N_{22}^2 + {}^{Im}N_{33}^2) \right)$$

$$a_{B,21} = -\frac{1}{12C_2} ({}^{Im}N_{12}^2 - i{}^{Im}N_{13}^2)$$

$$a_{B,2-1} = \frac{1}{12C_2} ({}^{Im}N_{12}^2 + i{}^{Im}N_{13}^2)$$

$$a_{B,22} = -\frac{1}{24C_2} ({}^{Im}N_{22}^2 - {}^{Im}N_{33}^2 + 2i{}^{Im}N_{23}^2)$$

$$a_{B,2-2} = -\frac{1}{24C_2} ({}^{Im}N_{22}^2 - {}^{Im}N_{33}^2 - 2i{}^{Im}N_{23}^2)$$

We see that imaginary parts of  $N_{ij}^2$  produce the B-modes.

# Appendix C

### C.1 Spherical Harmonics as $\alpha$ Notations

From the relations between the Cartesian coordinate directions and  $\alpha$  which is given by x, y and z, let us represent the spherical harmonics to x,y and z and also  $\alpha$  forms as the given form of  $x = i(\alpha^2 - 1), y = -2i\alpha, z = \alpha^2 + 1$ ,

$$\begin{split} l &= 1 \\ Y_{11} &= \sqrt{\frac{3}{8\pi}}(x+iy) = \sqrt{\frac{3}{8\pi}}\Big(i(\alpha^2-1)+2\alpha\Big) \\ Y_{10} &= -\sqrt{\frac{3}{4\pi}}z = -\sqrt{\frac{3}{4\pi}}(\alpha^2+1) \\ Y_{1-1} &= -\sqrt{\frac{3}{8\pi}}(x-iy) = -\sqrt{\frac{3}{8\pi}}\Big(i(\alpha^2-1)-2\alpha\Big) \end{split}$$

$$l = 2$$

$$Y_{20} = \frac{1}{4}\sqrt{\frac{5}{\pi}}(-x^2 - y^2 + 2z^2) = \frac{3}{4}\sqrt{\frac{5}{\pi}}(\alpha^4 + 2\alpha^2 + 1)$$

$$Y_{21} = \frac{1}{2}\sqrt{\frac{15}{2\pi}}(x + iy)z = \frac{1}{2}\sqrt{\frac{15}{2\pi}}(i\alpha^4 + 2\alpha^3 + 2\alpha - i)$$

$$Y_{2-1} = -\frac{1}{2}\sqrt{\frac{15}{2\pi}}(x - iy)z = -\frac{1}{2}\sqrt{\frac{15}{2\pi}}(i\alpha^4 - 2\alpha^3 - 2\alpha - i)$$

$$Y_{22} = \frac{1}{4}\sqrt{\frac{15}{2\pi}}(x + iy)^2 = \frac{1}{4}\sqrt{\frac{15}{2\pi}}(-\alpha^4 + 4i\alpha^3 + 6\alpha^2 - 4i\alpha - 1)$$

$$Y_{2-2} = \frac{1}{4}\sqrt{\frac{15}{2\pi}}(x - iy)^2 = \frac{1}{4}\sqrt{\frac{15}{2\pi}}(-\alpha^4 - 4i\alpha^3 + 6\alpha^2 + 4i\alpha - 1)$$

$$\begin{split} I &= 3 \\ Y_{30} &= \frac{1}{4} \sqrt{\frac{7}{\pi}} z (2z^2 - 3x^2 - 3y^2) = \frac{1}{4} \sqrt{\frac{7}{\pi}} (5\alpha^6 + 15\alpha^4 + 15\alpha^2 + 5) \\ Y_{31} &= -\frac{1}{8} \sqrt{\frac{21}{\pi}} (x + iy) (4z^2 - x^2 - y^2) \\ &= \frac{1}{4} \sqrt{\frac{7}{\pi}} \left( -\frac{\sqrt{3}}{2} \right) (5i\alpha^6 + 10\alpha^5 + 5i\alpha^4 + 20\alpha^3 - 5i\alpha^2 + 10\alpha - 5i) \\ Y_{3-1} &= \frac{1}{8} \sqrt{\frac{21}{\pi}} (x - iy) (4z^2 - x^2 - y^2) \\ &= \frac{1}{4} \sqrt{\frac{7}{\pi}} \left( \frac{\sqrt{3}}{2} \right) (5i\alpha^6 - 10\alpha^5 + 5i\alpha^4 - 20\alpha^3 - 5i\alpha^2 - 10\alpha - 5i) \\ Y_{32} &= \frac{1}{4} \sqrt{\frac{105}{2\pi}} (x + iy)^2 z = \frac{1}{4} \sqrt{\frac{7}{\pi}} \sqrt{\frac{15}{2}} (-\alpha^6 + 4i\alpha^5 + 5\alpha^4 + 5\alpha^2 - 4i\alpha - 1) \\ Y_{3-2} &= \frac{1}{4} \sqrt{\frac{105}{2\pi}} (x - iy)^2 z = \frac{1}{4} \sqrt{\frac{7}{\pi}} \sqrt{\frac{15}{2}} (-\alpha^6 - 4i\alpha^5 + 5\alpha^4 + 5\alpha^2 + 4i\alpha - 1) \\ Y_{33} &= -\frac{1}{8} \sqrt{\frac{35}{\pi}} (x + iy)^3 = \frac{1}{4} \sqrt{\frac{7}{\pi}} \left( -\frac{5}{4} \right) (-i\alpha^6 - 6\alpha^5 + 15i\alpha^4 + 20\alpha^3 - 15i\alpha^2 - 6\alpha + i) \\ Y_{3-3} &= \frac{1}{8} \sqrt{\frac{35}{\pi}} (x - iy)^3 = \frac{1}{4} \sqrt{\frac{7}{\pi}} \frac{5}{4} (-i\alpha^6 + 6\alpha^5 + 15i\alpha^4 - 20\alpha^3 - 15i\alpha^2 + 6\alpha + i) \end{split}$$

```
(0.00000, 0.00000, 1.00000)
(-0.99850, -0.05481, 0.00000)
(-0.05481,-0.99850, 0.00000)
(-0.99977, -0.02168, 0.00000)
(-0.02168, -0.99976, 0.00000)
 0.00000, 0.00000, 1.00000)
(0.00000, 0.00000, 1.00000)
(-0.99995, -0.00951, 0.0000)
(-0.00951, -0.99995, 0.0000)
(-0.00526, 0.99999, 0.0000)
(0.99999, -0.00526, 0.0000)
(0.00000, 0.00000, 1.0000)
(0.00030, -0.00224, 1.00000)
(0.00000, -1.00000, 0.00000)
(-1.00000, 0.00000, 0.00000)
(0.00000, -1.00000, 0.00000)
(1.00000, 0.00000, 0.00000)
(0.00000, 0.00000, 1.00000)
```

Table C.1: Numerical results from multipole vectors of Bianchi type V (left row of the Figure 5.13)

### C.2 Numerical results for multipole vectors

There are lists of multipole vectors of each  $l, v_{li}^l$  where  $1 \leq i \leq l$ .

```
(0.00000, 0.00000, 1.00000)
           (-0.71725, 0.69682, 0.00000)
           (-0.99613, 0.08792, 0.00000)
           (-0.83216, 0.55453, 0.00000)
           (-0.42358, -0.90586, 0.00000)
           (0.00000, 0.00000, 1.00000)
\begin{array}{c} v_1^1 \\ v_1^2 \\ v_2^2 \\ v_3^3 \\ v_3^3 \end{array}
           (0.00000, 0.00000, 1.00000)
           (-0.54948, 0.83551, 0.00000)
           (-0.80230, -0.59693, 0.00000)
           (-0.99073, 0.13582, 0.00000)
           (-0.11340, -0.99355, 0.00000)
           (0.00000, 0.00000, 1.00000)
\begin{array}{c} v_1^1 \\ v_1^2 \\ v_2^2 \\ v_3^3 \\ v_3^3 \end{array}
           (-0.00003, -0.00258, 1.00000)
           (0.00000, 1.00000, 0.00000)
           (-1.00000, 0.00000, 0.00000)
           (-0.86034, 0.50971, 0.00000)
           (0.50971, 0.86034, 0.00000)
           (0.00000, 0.00000, 1.00000)
```

Table C.2: Numerical results from multipole vectors of Bianchi type  $VII_h$  (middle row of the Figure 5.13)

```
(0.06792, -0.50486, 0.86052)
           (-0.48615, 0.87388, 0.00000)
           (-0.87388, 0.48615, 0.00000)
           (-0.70711, 0.70711, 0.00000)
           (-0.70711, -0.70711, 0.00000)
           (0.00000, 0.00000, 1.00000)
\begin{array}{c} v_1^1 \\ v_1^2 \\ v_2^2 \\ v_3^3 \\ v_3^3 \end{array}
           (0.04839, -0.96621, 0.25316)
           (-0.04771, 0.99886, 0.00000)
           (-0.99886, 0.04771, 0.00000)
           (-0.70711, 0.70711, 0.00000)
           (-0.70711, -0.70711, 0.00000)
           (0.00000, 0.00000, 1.00000)
\begin{array}{c} v_1^1 \\ v_1^2 \\ v_2^2 \\ v_3^3 \\ v_3^3 \end{array}
           (0.04689, -0.99880, 0.01413)
           (0.00000, 1.00000, 0.00000)
           (-1.00000, 0.00000, 0.00000)
           (-0.70711, 0.70711, 0.00000)
           (0.70711, 0.70711, 0.00000)
            0.00000, 0.00000, 1.00000)
```

Table C.3: Numerical results from multipole vectors of Bianchi type  $VII_0$  (right row of the Figure 5.13)

```
(-0.55930, -0.55930, 0.61185)
(-0.58660, -0.58660, 0.55838)
(0.12651, 0.12651, 0.98387)
(0.62506, 0.62506, 0.46754)
(-0.29255, -0.29255, 0.91040)
(0.00000, 0.00000, 1.00000)
(-0.52805, -0.52805, 0.66508)
(-0.68121, -0.68121, 0.26816)
(0.60129, 0.60129, 0.52620)
(0.86161, -0.02224, 0.50709)
(-0.02224, 0.86161, 0.50709)
(0.00000, 0.00000, 1.00000)
(-0.51447, -0.51447, 0.68603)
(0.01856, -0.99964, 0.01930)
(-0.99964, 0.01856, 0.01930)
(-0.01857, 0.99964, 0.01930)
(0.99964, -0.01857, 0.01930)
(0.00000, 0.00000, 1.00000)
```

Table C.4: Numerical results from multipole vectors of Bianchi type V with initial dipole (left row of the Figure 5.14).

```
(0.09866, 0.09475, 0.99060)
(0.31912, -0.21715, 0.92250)
(-0.07985, 0.02137, 0.99658)
(0.10705, -0.19653, 0.97464)
(-0.03002, 0.64083, 0.76709)
(0.00000, 0.00000, 1.00000)
(0.84745, -0.06328, 0.52709)
 0.02925,-0.99553, 0.08977)
(0.02128, 0.05346, 0.99834)
(-0.95001, 0.18662, 0.25031)
(-0.01887, -0.33716, 0.94126)
(0.00000, 0.00000, 1.00000)
(0.85556, -0.47404, 0.20809)
(-0.02311, 0.99857, 0.04817)
(-0.99597, 0.02305, 0.08669)
 0.85337,-0.51756, 0.06243)
(-0.50070, -0.86540, 0.01966)
 0.00000, 0.00000, 1.00000)
```

TABLE C.5: Numerical results from multipole vectors of Bianchi type  $VII_h$  with initial dipole (middle row of the Figure 5.14).

```
(-0.70711, -0.70711, 0.00000)
     0.70649, -0.70649, 0.04189)
=
     0.34443, -0.34443, 0.87335)
    (-0.70711, -0.70711, 0.00000)
    (0.20679, -0.20679, 0.95628)
    (0.00000, 0.00000, 1.00000)
    (-0.70711, -0.70711, 0.00000)
    (-0.70404, 0.70404, 0.09300)
    (-0.14300, 0.14300, 0.97934)
    (0.70711, 0.70711, 0.00000)
    (0.24060, -0.24060, 0.94033)
    (0.00000, 0.00000, 1.00000)
    (-0.70711, -0.70711, 0.00000)
    (-0.00143, 0.99928, 0.03780)
    (-0.99928, 0.00143, 0.03780)
    (0.70685, -0.70685, 0.02678)
    (0.70711, 0.70711, 0.00000)
    (0.00000, 0.00000, 1.00000)
```

Table C.6: Numerical results from multipole vectors of Bianchi type VII<sub>0</sub> with initial dipole (right row of the Figure 5.14).

## Bibliography

- [1] Friedmann A 1922 Z. Phys. 10 377
- [2] Lemaitre G A 1929 Ann. Soc. Sci. Brux. A 47 49-59; [in English] 1931Mon. Not. R. Astron. Soc. 91 483
- [3] Hubble E A 1929 Proc. Natl Acad. Sci. 15 168-173
- [4] Penzias A A and Wilson R W 1965 Astrophys. J. 142 419
- [5] Einstein A 1915 Sitz. Ber. Preuss. Akad. Wiss. 844
- [6] Dicke R H, Peebles P J E Roll P G and Wilkinson D T 1965 Astrophys.
  J. 142 414
- [7] Guth A H 1981 Phys. Rev. D 23 347
- [8] Linde A D 1982 Phys. Lett. B 116 335
- [9] Starobinskij A A 1979 Sov. Phys. JETP. **30** 682
- [10] Ellis G F R 1975 Royal Astronomical Society, Quarterly Journal 16 245
- [11] Cherepashchuk A M and Chernin A D 2008 Moscow University Physics Bulletin 63 5
- [12] Baryshev Yu V, Sylos Labini F, Montuori M and Pietronero L 1994 Vistas Astron. 38 419

- [13] Barrow J.D. 1986 in *Gravitation in Astrophysics*, eds Carter B. and Hartle J.B., Proceedings of NATO ASI Series B, **156** 239
- [14] Mather J C et al 1994 Astrophys. J. 420 439
- [15] Bennett C L et al 2003 Astrophys. J. Supp. 148 1
- [16] Hinshaw G et al 2009 Astrophys. J. Supp. 180 225
- [17] Coles P 2005 Nature **433** 248
- [18] Guth A H and Pi S Y 1982 Phys. Rev. Lett. 49 1110
- [19] Starobinskij A A 1982 Phys. Lett. B., 117 175
- [20] Bardeen J M, Steinhardt P J and Turner M S 1983 Phys. Rev. D. 28 679
- [21] Yadav A P S and Wandelt B D 2008 Phys. Rev. Lett. 100 181301
- [22] Vielva P, Martinez-Gonzalez E, Barreiro R B, Sanz J L and Cayon L 2004 Astrophys. J. 609 22
- [23] Cruz M, Martinez-Gonzalez E, Vielva P and Cayon L 2005 Mon. Not. R. astr. Soc. 356 29
- [24] Cruz M, Tucci M, Martinez-Gonzalez E and Vielva P 2006 Mon. Not. R. astr. Soc. 369 57
- [25] Cruz M, Cayon L, Martinez-Gonzalez E, Vielva P and Jin J 2007 Astrophys. J. 655, 11
- [26] Cruz M, Martinez-Gonzalez E, Vielva P, Diego J M, Hobson M and Turok N 2008 arXiv:0804.2904
- [27] Cayon L, Jin J and Treaster A 2005 Mon. Not. R. astr. Soc. 362 826
- [28] Naselsky P D, Christensen P R, Coles P, Verkhodanov O, Novikov D and Kim J 2009, arXiv/0712.1118

- [29] Schwarz D J, Starkman G D, Huterer D and Copi C J 2004 Phys. Rev. Lett. 93 221301
- [30] Copi C J, Huterer D and Starkman G D 2004 Phys. Rev. D. 70 043515
- [31] Katz G and Weeks J 2004 Phys. Rev. D. 70 063527
- [32] Land K and Magueijo J 2005 Mon. Not. R. astr. Soc. 357 994
- [33] Land K and Magueijo J 2005 Mon. Not. R. astr. Soc. 362 L16
- [34] Land K and Magueijo J 2005 Phys. Rev. D. 72 101302(R)
- [35] Land K and Magueijo J 2005 Phys. Rev. Lett. 95 071301
- [36] Land K and Magueijo J 2005 Mon. Not. R. astr. Soc. 362 838
- [37] Land K and Magueijo J 2007 Mon. Not. R. astr. Soc. 378 153
- [38] Copi C J, Huterer D, Schwarz D J and Starkman G D 2006 Mon. Not. R. astr. Soc. 367 79
- [39] Copi C J, Huterer D, Schwarz D J and Starkman G D 2007 Phys. Rev. D. 75 023507
- [40] Eriksen H K, Hansen F K, Banday A J, Górski K M and Lilje P B 2004 Astrophys. J. 605 14
- [41] Park C 2004 Mon. Not. R. astr. Soc. 349 313
- [42] Eriksen H K, Banday A J, Górski K M, Hansen F K and Lilje P B 2007, Astrophys. J. 660 L81
- [43] Hoftuft J, Eriksen H K, Banday A J, Górski K M, Hansen F K and Lilje P B 2009 Astrophys. J. Suppl. 699 985
- [44] Hansen F K, Banday A J, Górski K M, Eriksen H K and Lilje P B 2009 Astrophys. J. 704 1448
- [45] Hanson D and Lewis A 2009, arXiv: 0908.0963

- [46] Groeneboom N E, Ackerman L, Wehus I K and Eriksen H K 2009, arXiv: 0911.0150
- [47] Hanson D, Lewis A and Challinor A 2010, arXiv: 1003.0198
- [48] Zheng H and Bunn E F 2010, arXiv: 1003.5548
- [49] Chiang L-Y, Coles P, Naselsky P D and Olesen P 2007 J. Cosmol. Astropart. Phys. 01(2007)021
- [50] Chiang L-Y, Naselsky P D and Coles P 2007 Astrophys. J. 664 8
- [51] Francis C L and Peacock J A 2009, arXiv: 0909.2495
- [52] Short J and Coles P 2010 Mon. Not. R. astr. Soc. 401 2202
- [53] Grishchuk L P, Doroshkevich A G and Novikov I D 1968 Soviet Physics ZETP 55 2281
- [54] Ellis G F R and MacCallum M A H 1969 Commun. Math. Phys. 12
- [55] Collins C B and Hawking S W 1973 Mon. Not. R. astr. Soc. 162 307
- [56] Dautcourt G and Rose K 1978 Astr. Nachr. 299 13
- [57] Tolman B W and Matzner R A 1984 Mon. Not. R. astr. Soc. 392 391
- [58] Matzner R A and Tolman B W 1982 Phys. Rev. D. 26 10
- [59] Tolman B W 1985 **290** 1
- [60] Barrow J D, Juszkiewicz R and Sonoda D H 1985 Mon. Not. R. astr. Soc. 213 917
- [61] Bunn E F, Ferreira P G and Silk J 1996 Phys. Rev. Lett. 77 2883
- [62] Kogut A, Hinshaw G and Banday A J 1997 Phys. Rev. D. 55 1901
- [63] Jaffe T R, Banday A J, Eriksen H K, Górski K M and Hansen F K 2005 Astrophys. J. 629 L1

- [64] Jaffe T R, Hervik S, Banday A J and Górski K M 2006 Astrophys. J. 644 701
- [65] McEwen J D, Hobson M P, Lasenby A N and Mortlock D J 2005 Mon. Not. R. astr. Soc. 369 1583
- [66] McEwen J D, Hobson M P, Lasenby A N and Mortlock D J 2006 Mon. Not. R. astr. Soc. 371 L50
- [67] Bridges M, McEwen J D, Lasenby A N and Hobson M P 2007 Mon. Not. R. astr. Soc. 377 1473
- [68] Sung R and Coles P 2009 Class. Quantum Grav. 26 172001
- [69] Pontzen A and Challinor A 2007 Mon. Not. R. astr. Soc. 380 1387
- [70] Pontzen A 2009 Phys. Rev. D. 79 103518
- [71] Page L et al 2007 Astrophys. J. Supp. 170 335
- [72] Kamionkowski M, Kosowsky A and Stebbins A 1997 Phys. Rev. D. 55 7368
- [73] Hu W and White M D 1997 Phys. Rev. D. **56** 596
- [74] Rees M J 1968 Astrophys. J. 153 L1
- [75] Nanos G P 1979 Astrophys. J. 232 341
- [76] Negroponte J and Silk J 1980 Phys. Rev. Lett. 44 1433
- [77] Basko M M and Polnarev A G 1980 Sov. Astr. 24 268
- [78] Polnarev A G 1985 Sov. Astron. 29 607
- [79] Frewin R A, Polnarev A G and Coles P Mon. Not. R. astr. Soc. 266 L21
- [80] Ellis G F R 1967 J. Math. Phys. 8 1171

- [81] MacCallum M A H and Ellis G F R 1970 Commun. Math. Phys. 19 31
- [82] King A R and Ellis G F R 1973 Commun. Math. Phys. 31 209
- [83] Ellis G F R 2006 Gen. Rel. Grav. 38 1003
- [84] Kasner E 1921 Trans. Amer. Math. Soc. 43 217
- [85] Górski, K M, Hivon E, Banday A J, Wandelt B D, Hansen F K, Reinecke E M and Bartelmann M 2005 Astrophys. J. 622, 759
- [86] Campanelli L, Cea P and Tedesco L 2006 Phys. Rev. Lett. 97 209903
- [87] Campanelli L, Cea P and Tedesco L 2007 Phys. Rev. D. 76 063007
- [88] Bianchi L 1897 Mem. Sot. It. della SC., Dei XL 11 267.
- [89] Taub A.H., Ann. Math. 1951 **53** 472.
- [90] Barrow J D and Levin J 1997 Physics Letters A 233 169-174
- [91] MacCallum M A H and Ellis G F R 1970 Commun. math. Phys. 19 31-64
- [92] Ni W 2008 Prog. Theor. Phys. Supp. 172 49
- [93] Wu E Y S et al 2009 Phys. Rev. Lett. 102 161302 Reinecke E M and Bartelmann M 2005 Astrophys. J. 622, 759
- [94] Kim J and Naselsky P and Christensen P R 2008 Phys. Rev. D. 77 103002
- [95] Maxwell J C 1891 A Treatise on Electricity and Magnetism (Clarendon Press, London) Vol. I, 3rd edition.
- [96] Bielewicz P, Eriksen H K, Banday A J, Górski K M, and Lilje P B 2005 Astrophys. J. 635 750.
- [97] Newman E and Penrose R 1966 J. Math. Phys. **7** 863

- [98] Chandrasekhar S 1960 Radiative Transfer (New York, Dover)
- [99] Ellis G F R and Elst H V 1998, arXiv: gr-qc/9812046v4

